Solid-Fluid Interactions in Porous Media: Processes that Form Rocks

by

Einat Aharonov

Submitted in partial fulfillment of the requirements for the degree of
Doctor of Philosophy

at the

MASSACHUSETTS INSTITUTE OF TECHNOLOGY

and the

WOODS HOLE OCEANOGRAPHIC INSTITUTION

February 1996

Signature of Author .....
Joint Program in Oceanography,
Massachusetts Institute of Technology/Woods Hole Oceanographic Institution
February, 1996

Certified by .....
Daniel H. Rothman
Associate Professor, MIT
Thesis Co-Supervisor

Certified by .....
Peter B. Kelemen
Associate Scientist, WHOI
Thesis Co-Supervisor

Accepted by .....
Debborah Smith
Chairman, Joint Committee in Marine Geology and Geophysics,
Massachusetts Institute of Technology/Woods Hole Oceanographic Institution

Solid-Fluid Interactions in Porous Media: Processes that Form Rocks

by

Einat Aharonov

Submitted in partial fulfillment of the requirements for the degree of

Doctor of Philosophy at the Massachusetts Institute of Technology

and the Woods Hole Oceanographic Institution

February, 1996

Abstract

This thesis studies how rocks evolve due to the coupled effects of flow and chemical reaction. The study was motivated by various experimental observations, both in igneous and sedimentary rocks. In the first part of this thesis, growth of microscopic, pore-scale, features in sedimentary rocks is theoretically investigated. It is found, in agreement with experiments, that statistical properties of pore-grain interfaces mirror growth conditions. The shapes of pore-grain intrefaces both influence and are influenced by large-scale transport properties of the rock. The second part of this thesis employs analytical methods to study flow patterns in melt upwelling beneath mid-ocean ridges. It is shown that high permeability channels spontaneously form, allowing for efficient extraction of melt from the system. This result may aid in understanding existing geochemical and geological observations. In the third part of this thesis, I present a new $3D$ computer model that simulates flow and reaction through a porous matrix. The model is used to study and compare the different characteristics of dissolution and deposition, and to simulate different settings for melt upwelling in the mantle.

Acknowledgments

I think this part is essential for understanding the rest of the thesis, at least it was for me...

I dedicate this thesis to my parents, Tsipora and Dov Aharonov. Not only did they bring me to this world, but they also taught me love of truth, games, riddles, and curiosity for many years. Dorit and Niv, my sister and brother, were also part of these lively family gatherings, where we all competed to solve riddles and play games, and science intermingled with gossip. I think these gatherings shaped my thought process more than anything anyone has ever formally taught me.

I am grateful to Gilad, my beloved husband, partner, and friend. Without him I would never have come to MIT (for better or for worse). Gilad made having both a wonderful family and a thesis possible, understanding my "everything at the last minute" way of working, and supporting me while I struggled with both philosophical and practical aspects of a pursuing a PhD.

When I met Dan Rothman, my adviser, I was intending to leave MIT, since at that time I didnt like the PhD program I was in. I fell asleep at every single seminar I attended, and was seriously considering enrolling in med school. Dan asked me if I would like to try my hand at some fluid dynamics games before I left, and if I still wanted to leave in a few months, why, I could do it then. Working with Dan sounded like fun, and indeed, it was.

For the past five years Dan guided me through the dark forest of science, giving me freedom, yet insisting upon his usual high standards. Teaching me his own special and elegant style, yet allowing me to find my own path. I constantly admired his thorough and deep understanding of physics and bureaucracy alike, and hope I have absorbed some of that during the time I have worked with him.

It is next a true joy to thank Peter Kelemen who has been a mentor, an esteemed colleague, and a good friend. Peter's deep understanding of geology and geochemistry provided me with a rich and bottomless source of interesting scientific problems to study. His intuition and broad perspective contributed significantly to all my works.

Most of all, I thank Peter for the great time I had while doing exciting science.

Jack Whitehead has been a teacher, a collaborator, and a role model for a playful yet profound approach to geodynamics. It is through Peter and Jack that I came to do the work related to melt migration in the mantle.

It is with greatest pleasure that I thank Art Thompson. Art taught a course during his visit to MIT on the fall 1993, which motivated the first work presented here. Ever since then Art has graciously shared with me his important data, and his interesting thoughts. Our collaboration has been invaluable to me.

I would next like to thank Marc Spiegelman, who generously provided me with a his $3D$ MultiGrid code, without which the last chapter wouldnt have existed. I really enjoyed our discussions of the art and philosophy of numerics and physics, especially the science+drinking ones in WHOI.

I thank Caterina Riconde and Alison MacDonald, my dear friends, for the long-long lunches with lots of laughter, without which I wouldnt have been able to endure life in this gray place. And John Olson, a friend and a gentleman who shared my office for 4 years, and who was patient and helpful at all times, even when I nagged him when he was really busy, which I always did.

I finally thank Brian Evans, Greg Hirth, Gretchen Eckhardt, Olav Van Genabeek, Gunter Sideiqi, Steve Karner, Rafi Katzman, Bruno Ferreol, Sylvain Michalland, and Eirik Flekkoy for interesting and helpful discussions throughout the course of these last five years.

This work was supported by NSF Grants 9218819-EAR, OCE-9314013 and the sponsors of the MIT Porous Flow Project.

Contents

Chapter 1

Introduction

Motivated by various observations in sedimentary and igneous rocks, this thesis studies a few aspects of the slow process of rock formation. Such a study of formation of geological features is reminiscent of a murder investigation of an unknown person: On the one hand, the body (in this thesis, a rock) is observed out of context. It had a long life previous to this moment, but only a few snapshots in time are available to deduce the full chain of events. On the other hand, there is a multitude of data, only a small percent of which may be essential in understanding what is observed, but it is hard to determine beforehand which parts to ignore. The studies in this thesis propose that fluid flow and reaction through a porous medium strongly influence the evolution of rocks and their resulting properties, and may explain some of the experimentally observed richness.

Understanding coupled flow and reaction is important in a variety of geological and industrial settings. Dissolution and precipitation that occur during brine flow are responsible, to a large degree, for the formation of sedimentary rocks from the initial compacted grains [63]. Both the flow patterns and the chemistry within the earths mantle are effected by similar processes of reactive porous flow (e.g., [10, 19, 64, 44]), but here the fluid is lava melted from the grains at temperatures hundreds of degrees higher than in sedimentary rocks. Geologists, oil companies, hydrologists, companies concerned by contaminents and even coffee percolator manufacturers would like to understand, and in the end quantify, time dependent changes in geometrical and

transport properties of porous media due to clogging or corroding processes.

The study of the evolution of porous media during reactive flow is also intriguing on its own right, being a relatively basic, yet not well understood, physical process. Because of the strong non-linearities and the multiple length and time scales involved, coupled flow and reaction is most difficult to tackle. Length scales range between micrometers, the scale of a single pore where chemical reaction rates may be controlled by transport and kinetics at the pore wall, to tens of kilometers which can be the scale for flow through a sedimentary basin or the mantle. Time scales range just as widely: Fluid may flow on time scales of hours, but may react for years before any significant change in porosity occurs. Flow and reaction through porous media is also one of the few physical systems in which length and time scales continuously change with time, making it impossible to define a unique set of non-dimensional parameters to describe flow. For example, as a porous media is dissolved by acid, channels may form with characteristic length scaled much larger than the initial Darcy scale, and flow rates orders of magnitude faster than in the initial configuration [16].

Structures formed in rocks would be relatively uninteresting if pore fluids were static and in complete equilibrium with surrounding rock. Luckily, many natural systems such as sedimentary basins or the upper mantle are chemically open systems, with fluids continuously driven from here to there or back. In this case, long-range interactions or extensive disequilibrium are the rule rather than the exception. The dynamical system can be studied via different approaches, ranging from microscopic studies [92, 36, 9] of reactive "particles" in actual "pores", to analog network simulations [24], to solutions of macroscopic partial differential equations [14, 57]. A delicate aspect in all studies is the bridging across the scales. Due to computational limitations it is still difficult to use microscopic models to study macroscopic behavior that occurs on scales much greater than a single pore. It is similarly impossible to use macroscopic models to describe phenomena that occur on a pore scale. It is thus necessary to use a priori constitutive laws in macroscopic equations, which may be far removed from microscopic calculations. For example, solute concentration within a single pore may be uniform, but great differences in mineral compositions may be found between

neighboring pores [63]. Thus, one may conclude that although microscopic diffusion through pore fluids is most efficient, the resulting macroscopic diffusion coefficient is much smaller than naively expected, and is in some way influenced by interpore interaction.

In this thesis the different length scales are treated separately. Figure 1-1 illustrates the interactions between the scales of the different studies presented in this thesis.

In the first part (Chapter II, also in [1]) I construct a physical microscopic model of pore-grain interface growth in sedimentary rocks, based on experimental results [43, 53] that indicate that pore scale dynamics are controlled by chemical reaction rates and not by transport rates. The effect of flow at this scale is thus only in supplying unequilibrated fluid to pores and so allowing the existence of non-equilibrium features, and not in supporting gradients as at the larger scales. Chapter II proposes that sedimentary rocks, regardless of their mineralogy, follow a universal path of evolution in which their pore-scale statistical characteristics continuously change as they approach (but possibly never achieve) local chemical equilibrium. These changing statistics are in turn tied to changes in permeability, to form a closed picture about the evolving sedimentary rock. It is interesting that forming features, of the order of micrometers, both influence and are influenced by the large scale fluid transport.

In the second part of this thesis (Chapter III, also in [3]) I study macroscopic aspects of flow of melt, which is dissolving the surrounding mantle as it is upwelling beneath mid-ocean ridges. Coupled flow and reaction in this case are shown to be responsible for spontaneous formation of macroscopic channels, of fast and slow porous flow, which span the whole region of upwelling. The spontaneous formation of channels may resolve a long-standing puzzle (e.g., [22]) in the understanding of melt extraction from mid-ocean ridges. Chapter III was proceeded by [36], which presented initial investigations, both computational and experimental, and a description of the relevant geochemical processes.

In the third part of my thesis (Chapter IV) I present a macroscopic computer model of flow and reaction in $3D$, and apply it to both general aspects of flow and

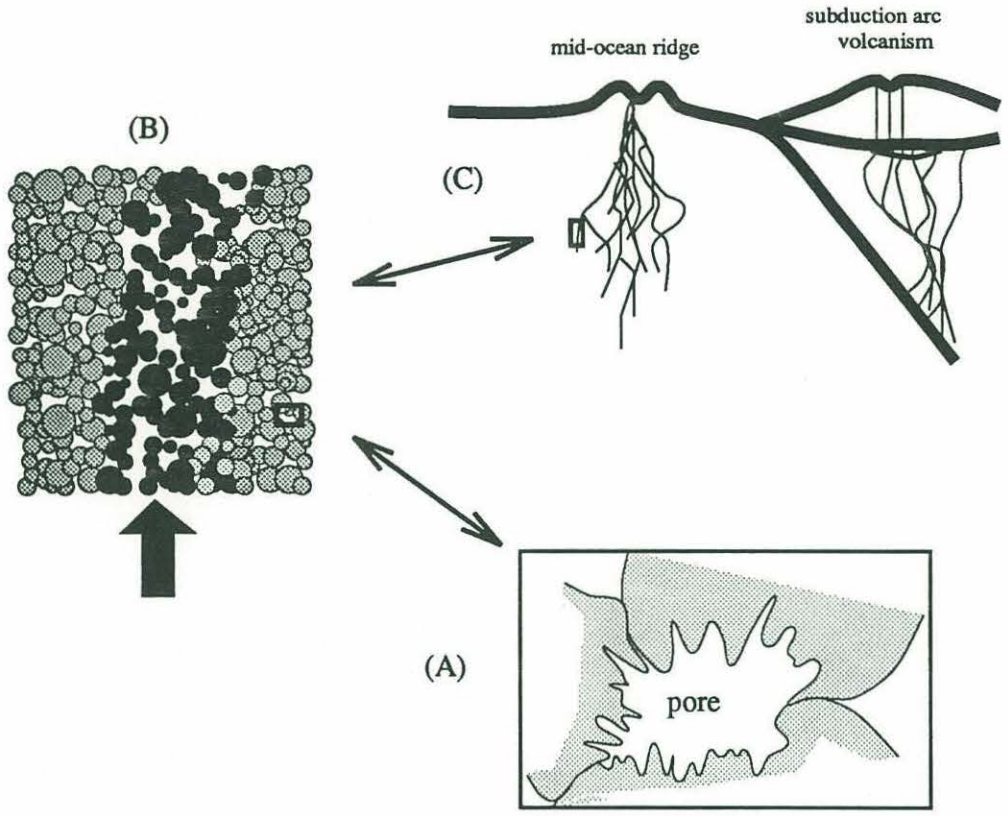

Figure 1-1: (A) On the smallest scales, the pore scale, this thesis studies statistical changes of pore-grain interfaces in sedimentary rocks. Results show that pore-grain interfaces both quantitatively reflect large scale changes in the rock (i.e., amount of diagenetic alteration), and effect the large scale transport properties. In this way scale (A) is tied to scale (B). (B) On the intermediate scale, this thesis studies the general effects of dissolution and precipitation on evolving porous media. $3D$ computer simulations show that dissolution will cause formation of preferred high permeability paths, (as illustrated in this figure by a black high permeability path formed by corrosive flow,) while precipitation will diffuse and homogenize any initially preferred paths of flow (not illustrated here). (C) On an even larger scale, coupled flow-reaction systems in different settings result in different geochemical and geological outcomes [36]. This thesis shows, by means of linear analysis and $3D$ computer simulations, that melt upwelling in conditions believed to describe midocean ridges, will focus into high permeability channels, due to its corrosive effect on the matrix. On the other hand, simulations mimicking intra-plate volcanism will result in diffuse flow, due to the cooling and crystallizing process induced by the continents, and a formation of an overpressurized region just below the crystallizing region. Using these results, large-scale geological and geochemical observations are understood via interactions on the intermediate scale (B).

reaction and to some scenarios of melt extraction from the mantle. The model is new both in its ability to simulate large systems more efficiently than previous models, and in its analytical macroscopic description of the deposition process. In Chapter IV the two processes of deposition and dissolution, and the organization of the porous media due to each one of them, are studied as opposite processes. The studies are performed in the limit where the effect of flow is maximized. In this case it is shown that dissolution produces long-range correlations in porosity and permeability while deposition produces negative correlations. The results of the experiments performed for melt migration agree both with Chapter III and with predictions in [36].

Lastly I will summarize the conclusions of this thesis: Coupled flow and reaction may be significant forces in shaping rocks as they evolve. This generic physical process may be responsible for the observed fractal structures on the pore scale of sedimentary rocks [38, 85, 1], for formation of channels in the mantle [3], or caves in calcite rocks [16]. It may influence rates of lava flow, and in turn rates of sea-floor accretion or eruption of volcanos, and determine where dikes will initiate in the mantle (Chapter IV).

I find that coupled flow and reaction are responsible for changing the statistical characteristics of a porous medium, with dissolution and deposition having qualitatively opposite effects. It may be possible in the future to use the statistics of the "geometrical fingerprints" to obtain quantitative constraints on the processes that different rocks have undergone. It is also clear that flow and reaction effect permeability, in a way which needs to be further studied. Future studies require deeper understanding and quantification of the interaction between the scales.

Chapter 2

Roughness in rocks

Abstract

Recent laboratory measurements have shown that pore surfaces of most sedimentary rocks have a fractal dimension ranging mostly between 2.6 and 2.8. The lower and upper cutoffs for fractal behavior are 10^{-2} and 10^{2} μm, respectively. The fractal dimension increases with diagenetic alteration. To explain these measurements, we construct a physical model of mineral deposition and dissolution on a substrate. We propose that when formation dynamics are reaction controlled, the forming pore-grain interface can be described by a non-linear partial differential equation for interface growth. We construct a discrete particle-deposition model corresponding to these dynamics. Three-dimensional computer simulations of the model show that resulting pore-grain interfaces are fractal, with a fractal dimension that increases from $D \approx 2.63$ to $D \approx 2.84$ as the dissolution rate is increased, in close agreement with observations. Additionally, our model predicts an increase in the amplitude of interface undulations with dissolution and fractal dimension. We conclude that geometrical measures of pore-grain interfaces are an indicator of the diagenetic history of sedimentary rocks, and are related to large scale changes in permeability.

2.1 Introduction

How can we better understand the conditions under which sedimentary rocks form? In this paper we concentrate on statistical measurements and geochemical observations to provide us with new insight into formation processes. Specifically, we study how dissolution, precipitation, weathering, erosion, and other processes that alter the pore-space of sedimentary rocks from its initial state (i.e., processes that cause "diagenetic

alteration"), affect certain statistical characteristic of these rocks.

As shown schematically in Figure 2-1, pore-grain boundaries observed in sedimentary rocks are usually quite "rough" and complex. A growing body of measurements [5, 30, 94, 84, 21, 38, 39, 83] suggest that in most sandstones and shales these pore-grain interfaces are fractal for length scales ranging over 4 orders of magnitude, from approximately 10^{-2} to 10^{2} μm. The measured surface area, S, of a fractal interface has a power-law dependence on the lateral extent L of the interface: i.e., $S(L) \propto L^{D}$, where $2 < D < 3$ is the interface fractal dimension [91]. Thus, the surface area of a fractal interface increases faster with L than if it were Euclidean (D=2), but slower than if it were a volume filling object (D=3). Fractal dimensions of pore surfaces in sedimentary rocks are observed to range mostly between 2.6 and 2.8, with D increasing with diagenetic alteration [39, 38, 85].

In general, a fractal distribution of features in space also indicates spatial power-law correlations between them [89]. Specifically, the "density-density" correlation function, designated here $c(r)$, describes the correlation between a scalar property ρ at position vectors r' and $r' + r$,

$$c(r) = 1/V \int_V \rho(r' + r)\rho(r')dr', \tag{2.1}$$

where V is the sample volume. When $\rho(r')$ is a distribution of solid ($\rho(r') = 1$) and voids ($\rho(r') = 0$) in space, then $c(r)$ is proportional to the probability of finding a solid object at position $r + r'$, given that there is a solid object at position r'. For a fractal object with a fractal dimension D, embedded in the Euclidean dimension $d = 3$, this correlation function scales like [89]

$$c(r) \sim r^{D-3}. \tag{2.2}$$

If pore interfaces are indeed fractal, equation 2.2 implies a formation process that is responsible for long-range correlations in space; e.g., crystal growth at one point in the pore influences growth at other points. Hence, in the study of the evolution of rocks one cannot isolate growth of single crystals and hope to fully characterize the dynamical formation process. One must instead consider the effect of the growth

and dissolution of a large number of crystals and their effect on one another, in order to understand the statistical surface measurements and their implications for rock formation.

In this paper we propose a physical model of evolution of pore-grain interfaces to explain such long-range correlations. Our goal is to provide a link between formation dynamics in rocks and measurable statistical properties. In constructing a model for explaining the existence of rough interfaces in rocks, we are guided by three main objectives:

1. The model should describe non-equilibrium growth.

2. The model should be independent of mineralogy, as is indicated by the range of length scales and diversity of minerals over which fractal behavior is observed. Specifically, fractal behavior is observed in rocks with many cementing components, from clays with crystals as small as $10^{-2}\mu$m to quartz with up to 100μm crystals.

3. The dynamical model should be consistent with known geochemical constraints for growth. The results of the model should also be consistent with available qualitative and quantitative statistical observations in sedimentary rocks, and supply an explanation for the range of fractal dimensions measured.

Previous attempts to construct a model [30, 15, 94] partially met the first two of these objectives but were unable to meet the third. In particular, no model has yet explained and predicted a range of observed fractal dimensions.

The construction of our model follows from recent experimental studies, (e.g., [65, 53]), that suggest that most sedimentary rocks form by reaction-controlled kinetics. Kinetics are reaction-controlled when the rate-limiting step for interface-growth is the chemical reaction at the interface rather than transport of mineral to the interface. We propose that when formation dynamics are reaction controlled, the forming pore-grain interface can be described by the interface growth equation derived by *Kardar, Parisi and Zhang* (KPZ) [1986]. This equation describes the evolution of an interface that grows everywhere in the direction normal to the interface, and includes terms to

allow for interfacial smoothing and random "noise". The KPZ equation has not been solved analytically for interfaces growing in the three-dimensional physical space, but a large body of numerical evidence shows that it describes the evolution of a self-affine (fractal) interface (see e.g.,[40]), with a fractal dimension that is possibly a function of varying growth conditions (e.g.,[95]).

Since we aim to investigate how different formation conditions effect measurable statistical parameters, we construct a computer model to simulate reaction-limited kinetics with a tunable rate of growth. Our model is a discrete three-dimensional particle-deposition model which is a variant of the so called "single-step" model (SSM) proposed by [48]. The SSM and variations of it have been used extensively as generic models for interface growth. One reason for this particular choice of model is the theoretical connection that can be made with the KPZ equation [48, 6]. Our variation allows for dissolution to occur as well as deposition, and one can choose the relative rates of dissolution versus deposition by changing the value of a control parameter. Simulation results indicate that as the ratio of dissolution versus deposition at the interface approaches unity, the fractal dimension of forming interfaces increases. The range of fractal dimensions of the simulated interfaces lies between $D = 2.63 \pm 0.005$ and $D = 2.84 \pm 0.01$, in close agreement to observations.

We then introduce a second variation of this model in which we allow the interface to undergo partial thermodynamic equilibration when dissolving. This allows for a thermodynamic distribution of dissolution features, and formation of etch-pits and holes. This second variation of the model results in non-symmetrical dissolution and deposition kinetics, which might prove to be a more realistic description of growth dynamics, since asymmetrical functions for dissolution and precipitation have been experimentally observed for many minerals [65, 53, 54]. Simulations show that statistical descriptions of interfaces formed by Model II are similar to those obtained from Model I.

After studying how growth affects formation of long-range correlations on interfaces, as measured via their fractal dimensions, we investigate a different geometrical property, the "roughness amplitude", and its relation to formation dynamics. We find

that the amplitude of interface fluctuations increases both with dissolution and the fractal dimension of interfaces. Simulation results show good qualitative agreement with our theoretical predictions.

Finally we compare results from simulations to existing observations and suggest an avenue for future work.

2.2 Experimental motivation

Experimental measurements, mostly motivated by a need to better characterize and predict properties of sedimentary rocks, have shown that sedimentary rocks are yet another one of the existing fractal objects to be found in nature [5, 30, 94, 84, 21, 38, 39, 83]. Specifically, measurements have shown that pore-grain interfaces in most sandstones and shales are statistically scale-invariant over up to four orders of magnitude; from $10^{-2}\mu$m, the scale of the smallest cementing crystals, to $10^{2}\mu$m, the scale of a characteristic pore.

These experimental measurements were performed using a variety of techniques. [21] covered the pore surfaces observed on thin sections with boxes of different sizes to find a power-law dependence between the size of boxes and the number of boxes needed to cover the pore surfaces. [84] measured the chord-length distribution formed by intersections between lines and pore surfaces observed on thin sections and fractures. Autocorrelation measurements were also done on thin-sections [30]. All the above mentioned techniques use thin-sections which are limited by the polishing process to a resolution of 1μm. In order to find the statistics at the molecular level, molecular adsorption [5] and small-angle scattering measurements [94] were performed; these indicate fractal pore surfaces. Capillary-pressure measurements [18] have been used [83] on the intermediate scale, between 10^{-2} and 1μm to provide overlapping data that supports the continuous power-law nature, over all relevant scales, of pore-grain interfaces in most sedimentary rocks.

Most ($\sim$ 75%) of the fractal dimension measurements of sedimentary rock pore-grain interfaces presented by [38] (Figure 2-3) fall within the range $2.6 \lesssim D \lesssim 2.8$. [94]

found a distribution of fractal dimensions between 2.25 and 2.95. Figure 2-2 (reproduced from [85]) shows thin-sections from 3 different sandstones, with $D = 2.55, 2.66$ and 2.75. In these thin-sections one can qualitatively observe a trend of increasing fractal dimension with increasing amount of cementation due to chemical diagenetic alteration of pores.

Figure 2-4 (from [85]) serves to quantify the observation that D increases with diagenesis. When the pore-grain interface is fractal, a *fractal porosity*, ϕ_f, can be associated with the pits and protruding features of these interfaces. The remaining open space, in which one can inflate an imaginary balloon, is defined to be the *Euclidean porosity*, ϕ_e (see Figure 2-1). ϕ_f is measured [85] using the capillary pressure method of de Gennes [18] that predicts that the capillary pressure of a non-wetting fluid, forced by pressure gradient to displace a wetting fluid, is indicative of the geometry of pore-grain interfaces in the rock. The total *measured porosity*, $\phi_m = \phi_f + \phi_e$, is obtained by gas-displacement methods. The relative measure of fractal porosity versus total porosity, $\phi_f/\phi_m = 1 - \phi_e/\phi_m$, constitutes a measure of diagenetic alteration. As diagenesis progresses, the total porosity, ϕ_m, changes from being associated mainly with large open voids, ϕ_e, to porosity associated mainly with pits and protrusions on a rough interface, ϕ_f. In Figure 2-4 one can see that D increases with amount of diagenetic alteration as measured by ϕ_f/ϕ_m.

2.3 Self-affine interfaces

In this section we formulate a mathematical description of the physical mechanisms that alter pore-grain interfaces in sedimentary rocks. We study the evolution of an interface between two distinct regions, a region of a pore filled with fluid and a region of solid, as shown in Figure 2-5. The height, $h(\mathbf{x})$, of the interface between the two phases is defined as the distance of the interface from a reference substrate.

2.3.1 Statistical description

A self-affine interface is statistically similar to itself under an affine transformation; i.e., when the directions parallel and perpendicular to the substrate are magnified by different values [87, 89] such that

$$h(x) \approx b^{-\alpha} h(bx), \tag{2.3}$$

where b is the amount of stretching parallel to the substrate and $b^{-\alpha}$ is the amount of stretching perpendicular to it. The approximation sign indicates that the two sides of the equation have identical *statistical* properties.

A useful statistical parameter is the standard deviation of the height, which will be identified here, as in much of literature on interfaces, as the *interface width*, W:

$$W(L) = \langle |h(\mathbf{x}) - \bar{h}|^2 \rangle^{1/2}, \tag{2.4}$$

where $\langle\ \rangle$ denote an ensemble average, and $\bar{h} = 1/L^2 \int_0^L h(\mathrm{x}) d\mathrm{x}$ is the mean interface height averaged over the lateral extent of the system L. The width of self-affine interfaces can be shown to relate to the linear dimension of the substrate L via a power law [89]:

$$W(L) \sim L^{\alpha}. \tag{2.5}$$

Here the exponent α has a simple relation to the fractal dimension of the interface,

$$\alpha = 3 - D, \tag{2.6}$$

for interfaces embedded in $d = 3$.

Figure 2-6 shows plots of interfaces (obtained from our simulations as outlined in following sections) taken from ensembles with 2 different fractal dimensions. The first one, Figure 2-6a, is a realization from an ensemble of interfaces with a fractal dimension of $D \approx 2.63$. It is relatively smooth, with greater dominance of long-wavelength structures over small-scale variability. Figure 2-6b is a realization taken from an ensemble with $D \approx 2.84$. This interface is jagged with relatively greater short-wavelength variability.

After introducing the basic concepts used in the study of self-affine interfaces (for a review see [6]), we next examine continuum models of interfaces undergoing generic dynamical processes of growth and smoothing.

2.3.2 Continuum models for dynamical growth of interfaces

Smoothing processes

The time evolution of a growing curved interface when subjected to smoothing processes such as surface tension effects, surface diffusion, mechanical erosion, weathering, recrystalization, etc, can be described by a simple diffusion equation:

$$\frac{\partial h(\mathbf{x},t)}{\partial t} = \nu \nabla^2 h(\mathbf{x},t) + \lambda, \tag{2.7}$$

where $h(\mathbf{x},t)$ is the surface height, λ is the average velocity of interface growth, and ν is an effective diffusion coefficient from the combined smoothing effects. A diffusion term in this context represents the decay of a curved interface due to processes that favor a lower surface energy. Such processes only rearrange the solid phase mass beneath the interface while conserving total mass. Any initial sinusoidal component of the interface which evolves by equation 2.7 decays exponentially to $h(x,t)$ =const [13, p.7-12]. Flat interfaces, such as those resulting from the steady-state solution of the diffusion equation 2.7, correspond to a fractal dimension of $D = 2$ [91].

"Noisy smoothing"

In real rocks random fluctuations can stem from impurities, anisotropies, nucleation processes, etc. We can mathematically model randomness in the formation process in a simple way by letting the rate of change in height have uncorrelated Gaussian fluctuations, $\eta(\vec{x},t)$, with a zero mean and an amplitude of Q:

$$< \eta(\mathbf{x},t)\eta(\mathbf{x}',t') >= 2Q\delta(\mathbf{x}-\mathbf{x}')\delta(t-t'). \tag{2.8}$$

Given such a white noise structure, the full stochastic description of interfaces undergoing "noisy smoothing" is:

$$\frac{\partial h}{\partial t} = \nu \nabla^2 h + \lambda + \eta(\mathbf{x},t). \tag{2.9}$$

Interfaces that grow according to 2.9 have a logarithmic relation between the width and lateral extent of the system [20]:

$$W^2(L) \sim \ln(L) \tag{2.10}$$

Hence an interface undergoing a "noisy-smoothing" process does not have a power-law dependence of W on L, as in equation 2.5, and therefore does not have a fractal dimension as defined by equation 2.6. The closest approximation is a fractal dimension of $D = d = 3$, equal to the Euclidean dimension in which it is embedded. Thus equations 2.7 and 2.9 are insufficient to describe the dynamical growth process which is responsible for formation of fractal interfaces.

Reaction-limited growth

Interface kinetics can also influence the physics of growth. Consider a mineral depositing from a saturated solution on a substrate such as described in Figure 2-5. The deposition process is composed of two main steps: transport of mineral in the fluid phase to the solid interface via advection and diffusion, and incorporation of the mineral at the interface via chemical reaction. The slower of the two steps determines the rate of interface growth. If reaction is slower than transport, the growth is called "reaction-controlled", while if transport is slower, growth is termed "transport-controlled". Reaction-controlled kinetics result in disappearance of concentration gradients in the fluid phase due to the fast transport, so that the concentration of mineral in the fluid is constant in space [50]. Thus the description of growth simplifies to only one variable, the height of the interface. Since there are no concentration variations in the fluid, every point on the interface will have equal probability to grow. Because there are no preferred directions and positions for growth, growth will occur *normal* to the local orientation of the interface and will be statistically uniform in space. This description is different from transport-limited growth, where one must consider the coupling between the interface height and the mineral concentration field in the fluid [42]. In that case growth sites that protrude into the fluid phase have a higher probability for deposition than growth sites on flat areas, because of the

steeper mineral concentration gradient near protrusions. Figure 2-7 schematically illustrates two extreme cases in the evolving different shapes of interfaces growing by reaction-controlled and diffusion-controlled mechanisms.

Recent experiments indicate that most sedimentary rocks (excluding some carbonates [52, 51]) form in the reaction-limited regime [43, 65, 53, 54, 50]. Characteristic order-of-magnitude experimental reaction rates are $K_- \sim 10^{-8}$ moles/m^2/sec for silica [65] and $K_- \sim 10^{-13}$ moles/m^2/sec for kaolinite [53, 54]. An order-of-magnitude calculation for diffusion rates of dissolving silica is [43]

$$K_{\mathcal{D}} = \frac{\mathcal{D}(C_\infty - C_{eq})}{\delta}.$$

Taking the diffusion rate constant $\mathcal{D}$ to be 10^{-5} cm^2/sec, the solubility of silica to be $C_{eq} \sim 10^{-3}$ moles/liter, the concentration at infinity to be $C_\infty = 0$, and the characteristic width of the boundary layer to be $\delta = 1\mu$m , then $K_{\mathcal{D}} \sim 10^{-4}$moles/m^2/sec. Thus diffusion rates in such a calculation are $O(10^4)$ times faster then reaction rates, resulting in a uniform concentration of mineral in the fluid, and reaction-limited growth.

Given an interface that grows by reaction-limited growth, (i.e. normal to its local orientation) with a constant normal growth velocity λ, Figure 2-8 shows, from purely geometrical arguments, that the increment of growth projected onto the h direction is

$$\delta h = \left((\lambda \delta t)^2 + (\lambda \delta t \nabla h)^2\right)^{1/2}. \tag{2.11}$$

For small slopes this can be written [29] as

$$\frac{\partial h(\mathbf{x}, t)}{\partial t} \approx \lambda + \frac{1}{2}\lambda(\nabla h)^2, \tag{2.12}$$

where the growth velocity λ depends on the saturation of depositing minerals in the fluid and reaction rates and can be time dependent. Here we shall assume for simplicity that the saturation is quasi-static, i.e. the saturation is effectively constant on the time-scales required for the interface to reach a statistical steady-state.

To combine smoothing, randomness, and growth processes we write an equation

describing the evolution of an interface as

$$\frac{\partial h}{\partial t} = \nu \nabla^2 h + \frac{1}{2}\lambda(\nabla h)^2 + \eta(\mathbf{x}, t), \tag{2.13}$$

where we have changed to a reference frame moving with the average interface velocity λ. Equation 2.13 (commonly referred to as the "KPZ" equation), was first introduced for the study of interface growth by [29]. The KPZ equation has been studied extensively as a continuum model for evolving interfaces, but due to intractable mathematical difficulties, numerical methods and theoretical investigation of its statistical characteristics constitute the main directions of research [6].

The deterministic version of 2.13, i.e., with $\eta(\mathbf{x}, t) = 0$, has known solutions. Resulting surfaces develop as a collection of paraboloids joined together by discontinuities in ∇h. Normal growth results in bumps growing laterally as well as sideways, so that an interface with some initial random configuration of features will tend toward increasing dominance of long-wavelength features over short-wavelength features, as seen in Figure 2-7a. The relaxation toward a flat interface in this case is interesting and quite different from the ordinary "diffusion" dominated case, as described by 2.7. For example, in an interface flattening in $d = 2$, the lateral extent of paraboloids grows with a power-law dependence on time, faster than the decay of a surface flattening due to diffusion-like smoothing processes [29].

Dynamic renormalization group calculations predict that interfaces that evolve according to the full stochastic equation 2.13 exhibit statistical scaling in space and time [29]. The width of these interfaces grows with time until it reaches a steady state, after which it retains a constant value W_s,

$$W_s(L) \sim L^{\alpha}. \tag{2.14}$$

The steady-state interface is thus a self-affine fractal, as defined by 2.5 and 2.6. While there are no conclusive theoretical predictions, computer simulations in $d = 3$ suggest the existence of a continuous transition from formation of non-fractal interfaces to formation of interfaces with $D \approx 2.6$ (or $\alpha \approx 0.4$) as $|\lambda|$ is increased from 0 to some finite value [95, 4, 59].

An intuitive understanding of the physics described by equation 2.13 can be gained by considering the effects of each term in 2.13 on formation of long-range correlations in the system:

a) When only diffusion-like smoothing acts upon the interface ($\nu \neq 0$ and $\lambda, \eta = 0$ in 2.13, resulting in 2.7), the steady-state interface is $h(\mathbf{x})$ =const, and since all points have identical height, a "height-height" correlation function does not decay in space and $D = 2$.

b) When white noise is added ($\nu, \eta \neq 0, \lambda = 0$, resulting in 2.9), the never-decaying correlations obtained in case (**a**) are diminished by the noisy random forcing. This results in an interface width W that grows only logarithmically with system size corresponding to the limit $\alpha \rightarrow 0$ ($D \rightarrow 3$) in equation 2.6.

c) When reaction-limited growth is also present ($\nu, \eta, \lambda \neq 0$, resulting in the full equation 2.13), "bumps" grow normal to the interface; thus when they grow upwards they also grow sideways (Figure 2-7a) at a rate faster than diffusion would predict, allowing local "height information" to be transmitted laterally. Hence normal growth enhances formation of long-range correlations and long-wavelength features, while suppressing or smoothing out short wavelength features, and thus decreases the fractal dimension of the forming interface.

Equation 2.13 therefore represents a balance between factors (diffusion and reaction limited growth) which tend to reduce small-scale features (decrease fractal dimension) and a factor (random forcing) which tends to relatively increase small-scale features. The balance that is struck by the coefficients of 2.13 should determine the fractal dimension of the pore interfaces.

A common method for quantitative study of growing interfaces is the construction of simple discrete models governed by processes similar to those described by the respective continuous equations. This approach avoids the severe sensitivity that direct numerical solutions to 2.13 exhibit. Such analog discrete models are also appealing due to their relatively simple implementation and the fact that in most interface growth problems (as in our problem of growth of crystals on interfaces) the physical system studied is actually discrete by nature. Nevertheless, continuous equations such

as 2.13 provide a predictive physical framework for the discrete studies. Here, the continuous representation is useful both for isolating the different processes involved in formation of pore-grain interfaces and for providing some physical insight into dynamics of formation of long-range correlations. For a review of recent approaches and results in the study of fractal interface growth see [45] and [6].

2.4 Computer simulations

We next present two simple discrete-particle models of interfaces roughening by deposition and dissolution, variations of the so-called 'single-step' model (SSM) [48] . The average properties of the SSM can be calculated and shown to correspond, to a first approximation, to equation 2.13 [48, 60]. It is this theoretical correspondence, as well as the existence of a physical analog between mechanisms in rocks and deposition and dissolution in the model, that led us to choose the SSM over the multitude of other discrete-particle models used to study the KPZ equation.

The original SSM (Figure 2-9) starts with a square lattice that is filled by steps in a checker-board manner; i.e., every filled site is a step of height 1 surrounded by nearest neighbor holes of height 0. At each successive time step, a site is chosen at random from all the sites that are local minima (i.e., sites that are lower than any of their nearest neighbors). The chosen site is then filled by a block of height 2, so that it now becomes a local maximum, 1 step higher than its neighbors. Qualitatively, the SSM captures the three generic physical processes described by the KPZ equation in the following way:

I) The SSM has an intrinsic smoothing process, corresponding to a diffusional term ν in 2.13, due to the requirement that the choice of deposition sites must be among the ones that are local minima, thus effectively "smoothing" away holes.

II) Randomness, corresponding to η in 2.13, is incorporated in the SSM by the random choice among all available sites.

III) Reaction-limited growth is incorporated because growth is restricted by the availability of growth sites, rather than by the supply of blocks from, say, a diffusing field.

The non-linear term in the continuum description of the SSM emerges from a geometrical argument similar to the one made in deriving 2.13. In Figure 2-8 the change in local height (δh) during normal growth is an increasing function of the local slope (∇h), so that $\lambda > 0$ in 2.13. In a $2d$ SSM, a locally flat interface has a height configuration of $h(x_i) = c$ for i even, $h(x_i) = c + 1$ for i odd, where c is a constant. In this case, half the sites are local minima and are available for growth, and the interface can grow rapidly. On the other hand, for an inclined interface ($h(x_i) = a + bi$) there are no sites available for growth, since no site is a local minimum. Hence, as with the KPZ equation, the SSM model enforces a dependence of local height change (δh) on local slope, but in the opposite sense (i.e. $\lambda < 0$). A quantitative derivation of 2.13 from the average properties of the SSM was made using mappings of the SSM to Ising spin and lattice gas models, and can be found in [48] and [6].

2.4.1 Model I: Symmetric dissolution and precipitation

Specifications We are interested in testing the hypothesis that the fractal dimension of forming interfaces depends on the relative amplitudes of noise η, smoothing rate ν, and reaction-controlled growth rate λ. We propose to control the reaction controlled growth rate by allowing dissolution of blocks in dynamics that mirror those of deposition. At each time-step a deposition event, as described above, will occur with a probability p_+ ($0 \geq p_+ \geq 1$) and a dissolution event will occur with a probability $p_- = 1 - p_+$. A dissolution event is defined to be the subtraction of a block of length 2 from a site randomly chosen among all the sites that are local maxima. By allowing particles to attach and detach to the interface, we hope to simulate molecular exchange across phase boundaries; increasing p_- increases the number of particles leaving the interface versus the number attaching to it.

Two-dimensional analogs of our model have been studied by [60] and [6]. They calculate that, on average, the evolution of the simulated interface is described by 2.13. Parameters ν and Q are constants independent of p_+, while

$$\lambda = -(p_+ - p_-). \tag{2.15}$$

Qualitatively, 2.15 describes a relation between the average growth velocity of the interface ($\propto (p_+ - p_-)$) and the non-linear coefficient λ. As expected from analog calculations for the continuum model (Figure 2-8 and equation 2.12) the magnitude of the non-linear coefficient increases with increasing interface growth velocity. Here $|\lambda|$ is maximum when $p_+ = 1$, and decreases to 0 when dissolution balances deposition and the interface has no net growth.

Results. Simulations of growing interfaces were performed for different system sizes, with p_+ varying from 0.5 to 1. (Note that $p_+ = 0.5$ is a symmetry point, and results obtained for advancing interfaces are applicable to retreating interfaces, with p_- and p_+ exchanged). Representative interfaces with $p_+ = 1$ and $p_+ = 0.6$ are shown in Figure 2-6. To quantitatively test whether resulting interfaces are self-affine, the interface width, $W(t)$ (as defined by equation 2.4) is measured for different system sizes L and averaged over an ensemble of 300 simulations performed with different random numbers. We find that the width of interfaces grows as a function of time until it reaches a statistically constant saturation value, W_s. Thereafter it exhibits a power-law dependence on system size, L, and remains self-affine, obeying equation 2.14. We ascribe this behavior to growth of 'bumps' both vertically and horizontally, as explained for Figure 2-7a, until a saturation value for the amplitude of the largest bumps is obtained when the wavelength corresponding of the lateral extent of the largest features reaches the system size. The initial transient phase of power-law growth in time is characteristic to interfaces that obey dynamics described by 2.13. The initial power-law growth of our model agrees well with theoretical predictions [40] for all $p_+ \gtrsim 0.6$. Although this transient evolution of interfaces is an interesting aspect of the problem, we limit the discussion in this paper to the non-equilibrium steady-state, since that is where we can make comparison with experiments.

To demonstrate the fractal nature of the resulting statistically steady-state interfaces, we plot $\log_{10} W_s$ versus $\log_{10} L$. For self-affine interfaces equations 2.14 and 2.6 should hold, and hence we expect that the width of self-affine interfaces will plot as straight lines on this graph with a slope which is equal to $3 - D$. Figure 8a shows

such plots for various p_+ values. Note that as p_+ decreases, the slope of the graph decreases, indicating an increase in the fractal dimension of the resulting interfaces with increasing amount of dissolution. For $p_+ \lesssim 0.6$ the results of simulations are not well-fit by a straight line; these interfaces are not self-affine. Figure 2-10b, a plot of W_s^2 versus $\ln L$, demonstrates that 2.10 provides a better fit for the data for high dissolution rates. This is consistent with the expectation that a transition from power-law to $W_s^2 \sim \ln L$ behavior will occur when $p_- \to p_+$ and $\lambda \to 0$.

After obtaining D for various p_+ values from Figure 2-10a, we investigated functional relations between deposition rate, dissolution rates, and fractal dimensions of forming interfaces. In Figure 2-11 we plot D versus a nondimensional parameter p_-/p_+ which we term the "dissolution-deposition ratio". The dissolution-deposition ratio measures the rate of particles leaving the interface ($2p_-$) versus the rate of particles attaching to it ($2p_+$).

The fractal dimension of resulting interfaces is seen to increase with the dissolution-deposition ratio, with a curve showing that for $p_-/p_+ = 0$, $D = 2.63 \pm 0.005$, in agreement with previous simulations of the pure deposition SSM [48], and as p_-/p_+ increases, D approaches a limiting value of 2.84 ± 0.01. An increase in the dissolution-deposition ratio above $p_-/p_+ \approx 0.7$ results in suspected loss of fractal behavior and a transition to logarithmic, rather than power-law, dependence of W_s on L.

2.4.2 Model II: Asymmetric model of dissolution and precipitation

Specifications. We next construct a variation of Model I that models dissolution in partial thermodynamic equilibrium [93]. This is done in order to investigate the effects of a finite probability for the development of features such as etch pits and holes that can be found in rocks. Allowing for partial thermodynamic equilibration in the dissolution step, but not in the deposition step, creates an asymmetry between the two processes. Asymmetrical functions for dissolution and precipitation have been experimentally observed for many minerals [65, 53, 54].

In Model II, deposition occurs with probability p_+ identical to the deposition step in Model I, but a temperature-dependent dissolution step occurs with probability $p_- = 1 - p_+$ in a way that allows for thermodynamic equilibration of the interface. The dissolution step is constructed as following: A site i is randomly chosen among all the sites of the interface and the local surface area

$$E_i = \frac{1}{4}\sum_{\delta} |h_i - h_{i+\delta}|$$

is measured, where summation is over the 4 nearest neighbors. If a block is to be dissolved at site i, the change in surface area, $\Delta E_i = \sum_\delta (|h_i - 2 - h_{i+\delta}| - |h_i - h_{i+\delta}|)$, is calculated. The probability q of occurrence of a dissolution event at site i is then defined to be

$$q = \begin{cases} 1 & \text{if } \Delta E < 0 \\ e^{-\Delta E/kT} & \text{if } \Delta E > 0 \end{cases} \tag{2.16}$$

Here kT is a tunable model temperature, roughly analogous to a thermodynamic temperature. Dissolution at site i will thus happen if a dissolution event results in reduced or equivalent surface area, and will have an exponentially decaying probability to occur if the surface area is increased by the dissolution step. Finite probability for increasing the surface area is allowed in order to model etch-pits and holes, features observed in rocks. If dissolution of a block did not occur at the site i first chosen, a different site is randomly chosen among all the sites of the interface and a dissolution event is attempted (according to rule 2.16) at the newly chosen site, and so on, until an attempt to dissolve is successful. The only effect of these repetitive attempts at dissolution is to force p_- to be constant and equal to $1 - p_+$. At the zero temperature limit this model reduces to Model I. At high enough temperatures the dissolution step introduces only noise to the system while reducing the growth rate.

Because dissolution introduces a thermodynamical equilibration procedure that is not duplicated in the deposition event, the dynamics of retreating interfaces with $p_+ < 0.5$ in Model II are not the mirror image of interfaces with $p_+ > 0.5$. This asymmetry is the fundamental difference between Model II and model I.

Results. We performed statistical studies for interfaces forming at different kT, p_+, and L. At all temperatures studied we find that, similar to the results of Model I, the width of interfaces formed by Model II have a transient stage of dynamical scaling, after which they reach a statistical steady-state. Graphs of $\log W_s(L)$ as function of $\log L$ are plotted in Figure 2-12a and b for $kT = 1$ and $kT = 100$, respectively. It is demonstrated that power-law models provide a good fit to the data, although logarithmic dependence between the width and size of the system for high dissolution rates at low temperatures cannot be ruled out. The fractal dimension for $kT = 1$ (Figure 2-12a) is seen to increase with increasing p_-/p_+ similarly to results of Model I. For $kT = 100$ (Figure 2-12b) we note a different behavior than for the low temperatures. The fractal dimension (deduced from the measured slope) of interfaces is nearly constant with increased dissolution, but the amplitude of the width increases with decreasing p_+.

Figure 2-13 shows the fractal dimension of interfaces as function of p_-/p_+. The four curves correspond to four different temperatures: $kT = 10^{-2}, 1, 10^2$ from this model, and $kT = 0$ replotted from Model I. At high temperatures ($kT = 10^2$) the fractal dimension is nearly constant as a function of relative dissolution rate. For low temperatures all curves follow the same trend of increased D with increased dissolution. We believe that interfaces formed at low temperature are not fractal for $p_-/p_+ \gtrsim 0.7$.

2.4.3 Roughness of interfaces

The notion of roughness of an interface, i.e. the amplitude of its fluctuations, can be quantified by measuring the prefactor in equation 2.14, now rewritten as

$$W_s = A(D)L^{3-D} \tag{2.17}$$

The prefactor, $A(D)$, is termed the "roughness amplitude", and measures the amplitude of the undulations of interfaces.

In Figure 2-14 we plot A, calculated for all temperatures, from intercepts of lines in Figures 2-10a and 2-12a,b with the width axis, versus p_-/p_+. We find that the

roughness amplitude increases approximately linearly with the dissolution-deposition ratio. It is interesting to note that data from all temperatures follow the same linear trend, except where interfaces are not likely to be fractal. At low temperatures, where dissolution-deposition ratio is high enough ($p_-/p_+ \gtrsim 0.7$), the roughness reaches a plateau and diverges from the linear trend. We attribute this to the logarithmic dependence of W^2 on L for dissolution-deposition ratios close to unity. Thus we can use the divergence from the linear trend in Figure 2-14 as another indication for circumstances for which interfaces cannot be well modeled as fractals. The dissolution-deposition ratio obtained for this divergence ($p_-/p_+ \gtrsim 0.7$) is consistent with that determined from Figures 2-10 and 2-12.

The dependence of A on D can be predicted for the zero temperature model by using two constraints. The first constraint emerges from the "single-steppedness" of Model I: the square of the slope of the height at any given site must always be equal to unity ($|h_i - h_{i+\delta}|^2 = 1$). The second constraint is that the power spectra of self-affine interfaces have a power-law form [87]. The details of predicting $A(D)$ are given in Appendix A.

Figure 2-15 shows that for $kT = 0$, A is an increasing function of D, which means that on short length-scales interfaces with high fractal dimensions appear rougher and have larger undulations than interfaces with lower fractal dimensions. The discrepancy between simulation results and theoretical predictions is probably due to the fact that the power spectrum in the theoretical calculation of $A(D)$ is assumed to follow a power-law at all wavelengths (as given in equation A.9), but in reality only follows this behavior between high and low wavenumber cutoffs.

We note that although A is an increasing function of p_-/p_+ and D (Figures 2-14 and 2-15), the measured width W of interfaces of large enough lateral extant L is a decreasing function of p_+/p_- and D. This is because as the system size increases, W increases as well, but more slowly for interfaces with high fractal dimensions than for interfaces with low fractal dimensions, which can be seen from both equation 2.17 and Figure 2-10. Thus, for a "system-sized elephant" an interface with a high fractal dimension appears smoother than one with a lower fractal dimension, while for a

"particle-sized ant" an interface with a high fractal dimension is rougher than one with a low fractal dimension.

2.5 Summary and discussion

2.5.1 Summary of model and results.

Motivated by experimental data indicating fractal pore surfaces in sedimentary rocks, we have developed an analytical description and a simple computer model for reaction-controlled growth of interfaces. Analytical arguments lead to the KPZ equation 2.13 [29], a non-linear partial differential equation extensively studied as a model for growth of self-affine interfaces (e.g., [6]). This equation describes dynamical interface evolution governed by diffusion-like smoothing, reaction-limited growth, and random events. Our goal in studying such dynamical descriptions of interface growth was to find a link between physical processes that govern growth and geometrical properties of resulting interfaces. Such a link can help constrain formation history of rocks by measuring their geometrical properties.

In order to study how different dynamical processes affect the steady-state statistics of interfaces we have constructed a discrete particle deposition and dissolution model which incorporates reaction-limited growth, interfacial smoothing, and random "noise" processes at a growing interface and provides a control over the relative rates of these processes. The average properties of interfaces formed by this model were shown (in $d = 2$) to correspond to the KPZ equation. We qualitatively explain this correspondence.

Interfaces formed by our model go through a transient stage of roughening after which they reach a statistical steady state, where the interfaces still grow, but their statistical characteristics remain constant. The steady-state interfaces are fractal for most parameter ranges, with the fractal dimension increasing from 2.63 ± 0.005 to 2.84 ± 0.01 as the dissolution-deposition ratio is increased. For dissolution-deposition ratios approaching unity, interfaces formed are no longer fractal. These results are

consistent with an expected transition from fractal to non-fractal interfaces when the magnitude of the non-linear term in the KPZ equation is decreased from a finite value to 0. The nature of the transition is not theoretically predicted.

We also find that the "roughness amplitude" of interfaces, A (as defined in equation 2.17), increases with increasing dissolution-deposition ratio and increasing fractal dimension of simulated surfaces. This behavior is in relatively good agreement with our theoretical predictions.

2.5.2 Comparison with experiments

The emerging physical picture. Laboratory measurements show that the majority of sedimentary rocks are fractal with $2.55 \lesssim D \lesssim 2.8$, as seen in Figures 2-3 and 2-4. This range coincides approximately with our simulation results. The experimental observations also show that rocks with highly diagenetically altered porosity (generally the samples with higher content of cementing materials, and more evidence of dissolution and precipitation) correspond to the higher fractal dimensions. We propose the following scenario to explain the observed trend in the geometry of pore-grain interfaces: Near-surface sedimentary rocks are usually part of a large scale system through which fluid is flowing at non-negligible flow rates. These rocks are thus prevented from reaching global chemical equilibrium as one would expect for samples in a closed system. Diagenetic processes occur in the forming rock as a consequence of this non-equilibrium situation. Since diagenesis generally acts to reduce permeability [69, 63], the rock becomes more resistant to fluid flow with time. Although global equilibrium is not reached, the reduction in flow rates results in pore fluids spending more time in a pore and thus becoming more locally chemically equilibrated with surrounding solid. Thus, growth and dissolution ionic fluxes at the pore surface begin to equilibrate and p_-/p_+ increases. Figure 2-11 shows that the fractal dimension increases when p_-/p_+ increases, while Figures 2-2 and 2-4 show that the fractal dimension increases with diagenetic alteration. The model and experiments together suggest that growth and dissolution in a finite volume lead to a unique "diagenetic pathway" that is descriptive of pore evolution in many similar rocks. At

the beginning of the pathway the pore is relatively open, crystal growth is reaction limited with a small p_-/p_+ (or small p_+/p_-, in the symmetrical case of dissolving interfaces) and the resulting fractal dimension is near 2.6. As the pore space is filled, the balance of growth and dissolution rates shifts toward unity, p_-/p_+ increases, and so the fractal dimension increases. Following this model, [85] find a limiting fractal dimension, $D = 2.75$, reached by the competition between rates of ionic diffusion on an increasingly rough surface, and reaction.

Finally, it is possible to tie the physical picture with a recent result that demonstrates (Figure 2-16) that the permeability, $\mathcal{K}$, is related to ϕ_e and l_e, the Euclidean porosity and length scale, and not to the total porosity and length scales [85, 2], via:

$$\mathcal{K} = \frac{1}{226} l_e^2 \phi_e^2, \tag{2.18}$$

Since $\phi_f/\phi_m = 1 - \phi_e/\phi_m$ increases with diagenesis (see Figure 2-4), equation 2.18 predicts that permeability will decrease with time, even if ϕ_m stayed constant (a prediction in agreement with experimental results in [69]). The reduced fluid flow rates result in more equilibration and so the fractal dimension will increase, and ϕ_f and ϕ_e will consequently change. Thus, the evolving microscopic features on pore-grain interfaces both influence and are influenced by the large scale transport properties.

Comparison of model results for the "roughness amplitude" with data from real rocks should be approached with caution because of the large number of variable parameters. These can be dealt with by constructing suitable transformations (e.g. doubling molecular size would result in double roughness amplitude). Although at this point we have no reliable data to which we can compare our roughness results, estimates of A from [38] show a trend of increasing A with D, as predicted quantitatively from our models. Our simulations also predict that diagenetically altered pores that appear rough on the crystal scale will appear smooth on the pore scale, while rocks which have low D and little diagenetic alteration will appear smooth on the crystal scale but rough and strongly undulating on the pore scale. At this point we do not have enough data to check this prediction.

Deviations of some observations from the predicted. Simulation results do not predict the observations of sedimentary rocks with $D \lesssim 2.6$. Since it is our intention to capture the dominant physical processes in pore-grain interfaces, why can we not simulate these existing, though less common, observations? Most likely our model does not adequately describe all natural growth environments, in particular the different growth mechanisms. We propose that the small percentage of rocks that have a fractal dimension which cannot be explained by our model should serve as a test for a point of departure of the formation conditions from the ones assumed by our models. For example, transport-controlled growth, which was not investigated here, may produce completely different results from our model. Transport-limited growth might be the mode of growth for some carbonates (e.g., calcite and arogonite at certain pH levels [52, 51]) that are highly soluble. Bedford limestone, a carbonate for which $D = 2.35$ [39], serves as an example for transport limited growth leading to fractal interfaces, with a fractal dimension quite different than that predicted by our model. Another possibility is that all the processes that we have termed "noise" are not uncorrelated as we postulate. While uncorrelated noise might be a good assumption in most cases for forming sedimentary rocks (due to the generally short range nature of the forces exerted by ions on the interface, the random position of impurities and orientation of grains on which growth occurs, the random process of nucleation, and a variety of other conditions), one can imagine cases where random events tend to be correlated in space and time, such as when one mineral acts to lower the surface energy for a second mineral to crystallize, or when events are correlated in space by certain directions of growth being energetically preferred. By introducing power-law correlated noise, interfaces may be formed with a continuously varying fractal dimension between 2 and 3, as demonstrated by computer and theoretical models [49, 46, 47]. As one might naively expect, forcing external correlations (anti-correlations) on the growth process indeed increases (decreases) correlations between points on the interface and results in a lower (higher) surface fractal dimension.

2.6 Conclusion

Our proposed physical and numerical model addresses the three requirements posed in the introduction: it is a model of non-equilibrium growth, it is independent of mineralogy, and it agrees with the observations that higher fractal dimensions are found in rocks that are more diagenetically altered. Thus, we believe that the general physical mechanism of growth in most shales and sandstones can be captured by the simple processes of reaction-limited growth and smoothing in a noisy system. This microscopic growth is in turn linked to the large scale permeability changes occurring during diagenesis.

This work constitutes a first step in using geometrical constraints to study the dynamical history of the formation of rocks. More quantitative observations of geometrical properties as well as more experiments for controlled growth in the laboratory are necessary before a comprehensive theory can be developed.

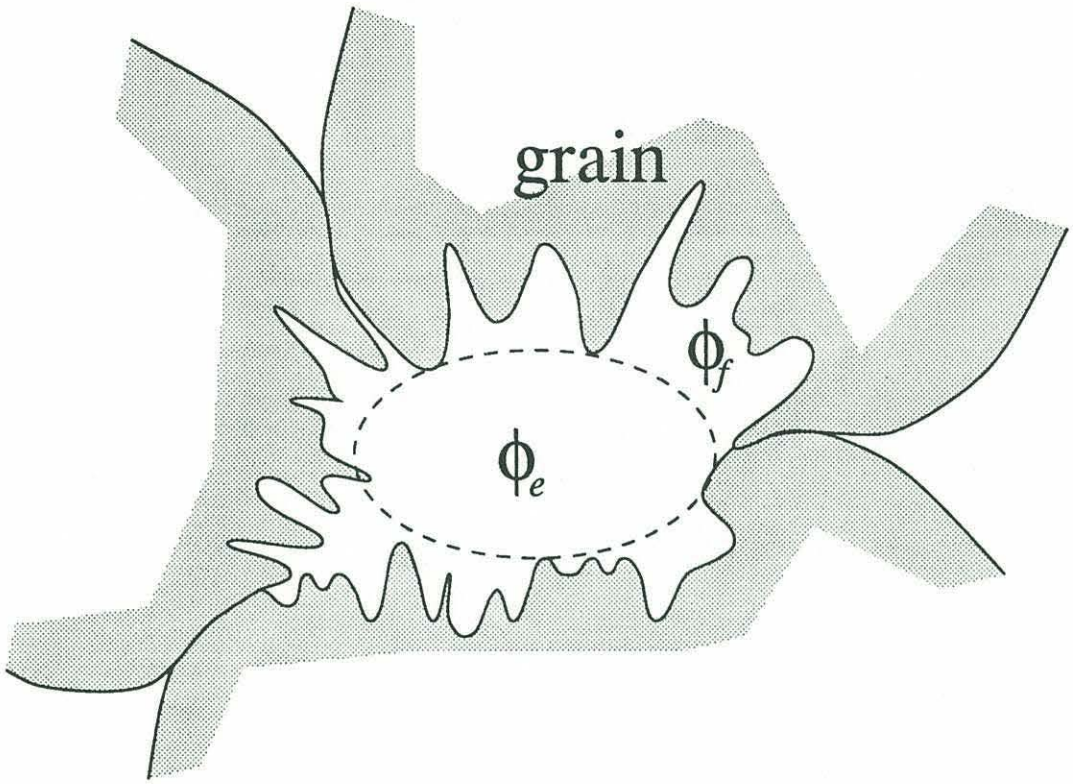

Figure 2-1: Schematic diagram of a single pore in a sedimentary rock. Pore-grain interfaces in sedimentary rocks are generally quite convoluted with geometrical structures formed by cementing crystals and corroded etch pits and holes. The total porosity, ϕ_m, is a sum of ϕ_e, the porosity associated with Euclidean open pore space, and ϕ_f, the porosity associated with fractal undulations of the pore-grain interface.

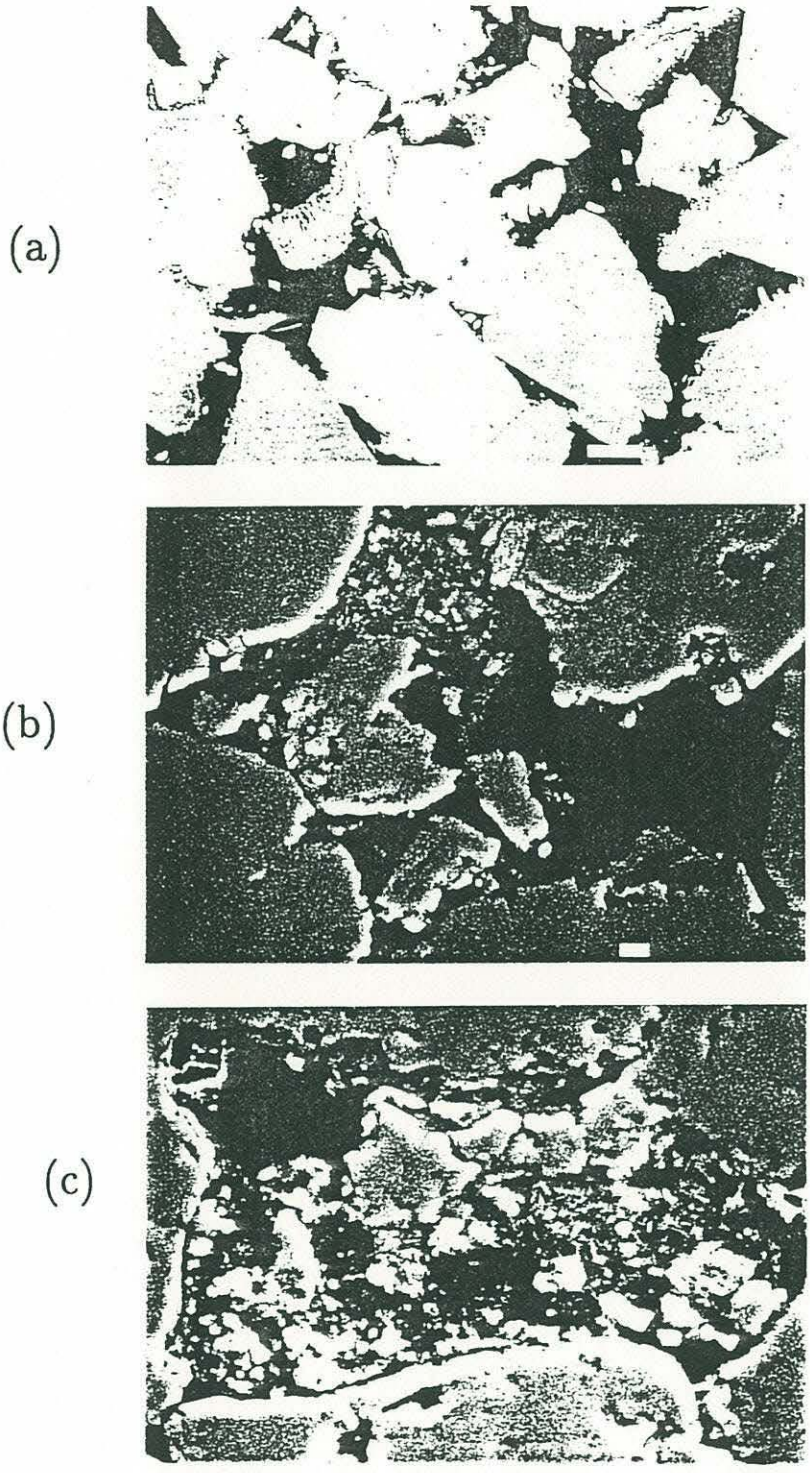

Figure 2-2: From [85]. Thin sections of three sandstones. (A) Table sandstone with a fractal dimension of $D = 2.55$. (B) Price River sandstone with $D = 2.66$. (C) Coconino sandstone with $D = 2.75$. The fractal dimension increases with increasing volume of cementing material and dissolution of the initial sand grains.

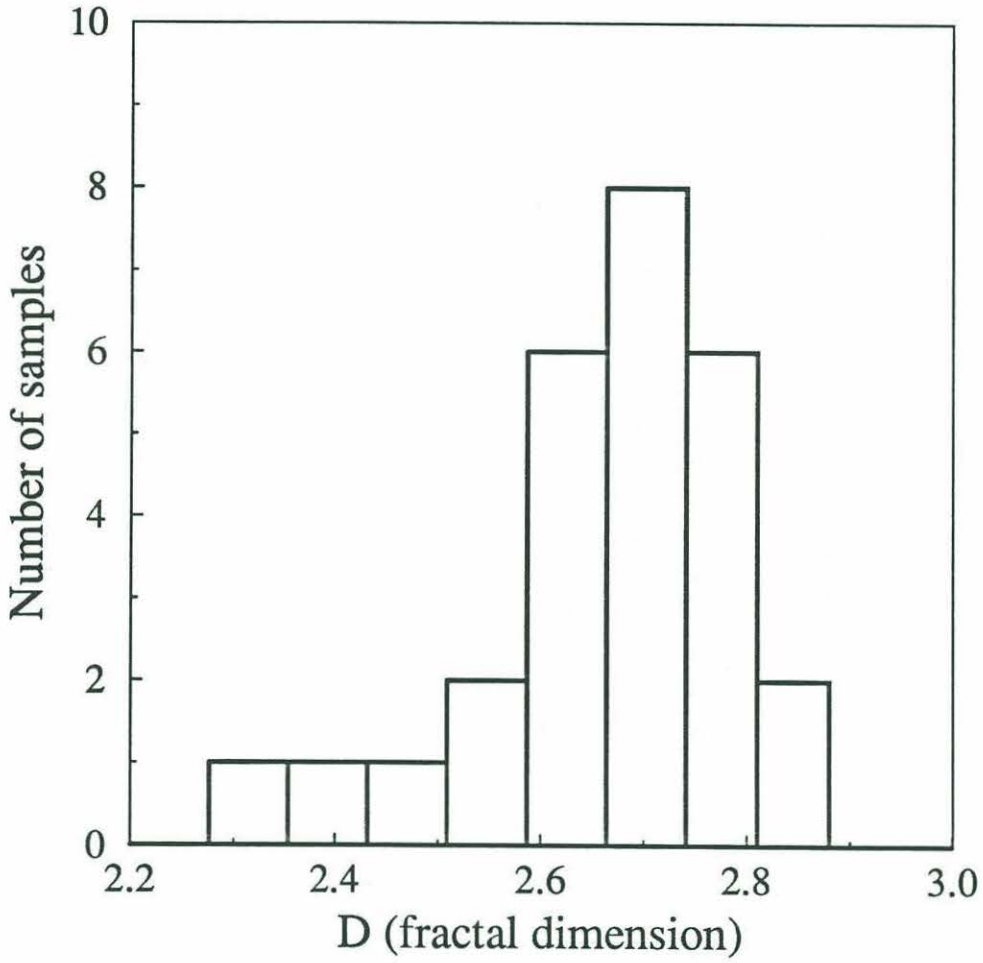

Figure 2-3: A histogram of fractal dimensions for 27 different rocks. Bins are of equal size. The data are from [38]. 75% of the observed rocks have a fractal dimension between 2.6 and 2.8.

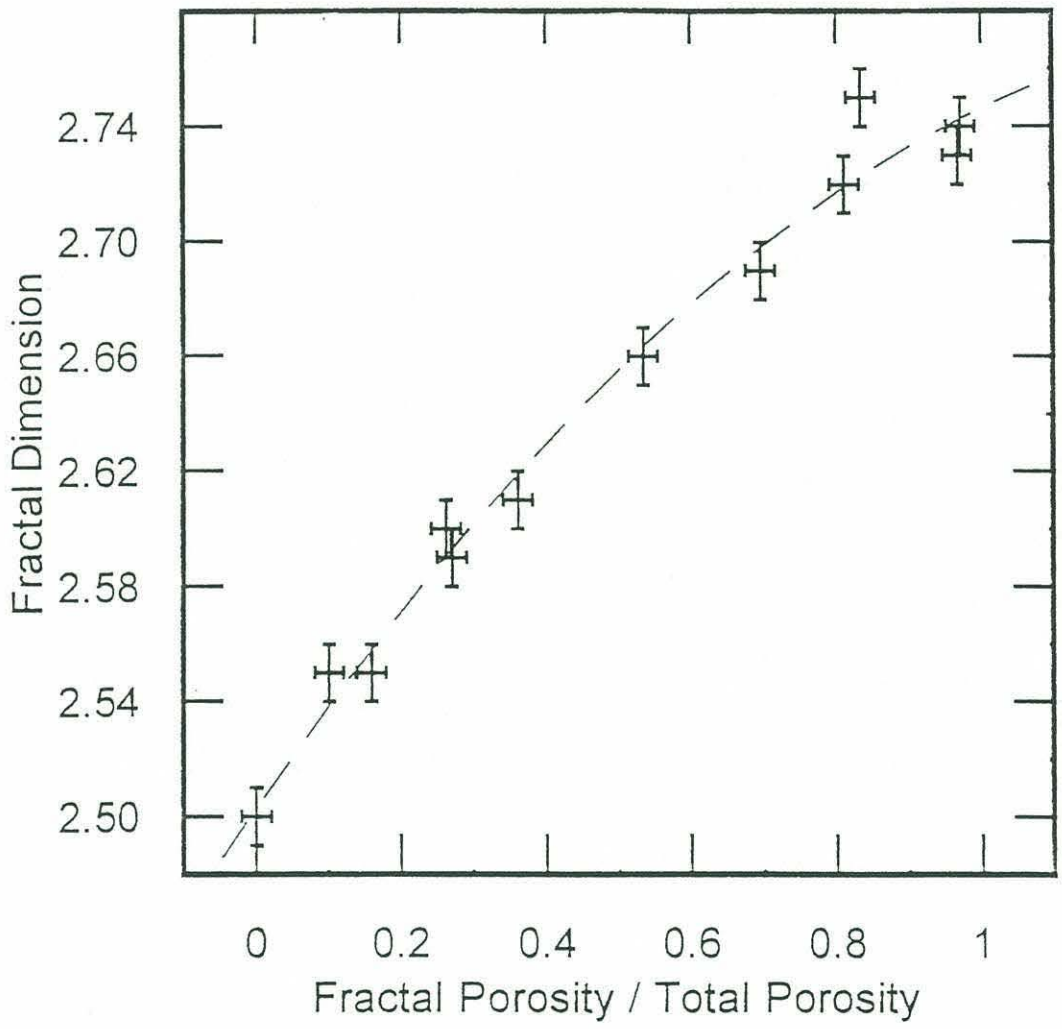

Figure 2-4: From [85]. The measured fractal dimension D of pore-grain interfaces versus the porosity associated with fractal surfaces over the measured total porosity, ϕ_f/ϕ_m, of 11 different sandstones and 1 shale. The plot shows a monotonic increase of D with ϕ_f/ϕ_m.

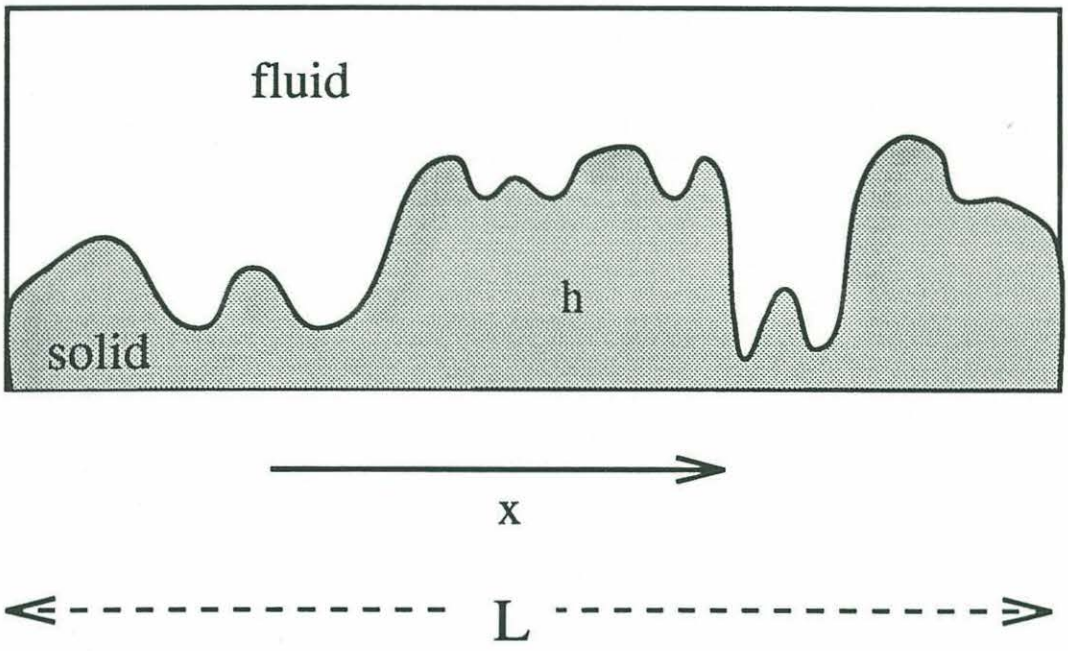

Figure 2-5: A schematic view of the interface between a fluid-filled rock pore and a solid rock material. This is the setting of the theoretical problem: an interface, with no overhangs, constitutes the boundary between fluid and solid phases. The interface position is described as a height deviation, $h(x,t)$, from a substrate. L is the lateral extent of the substrate on which the interface grows.

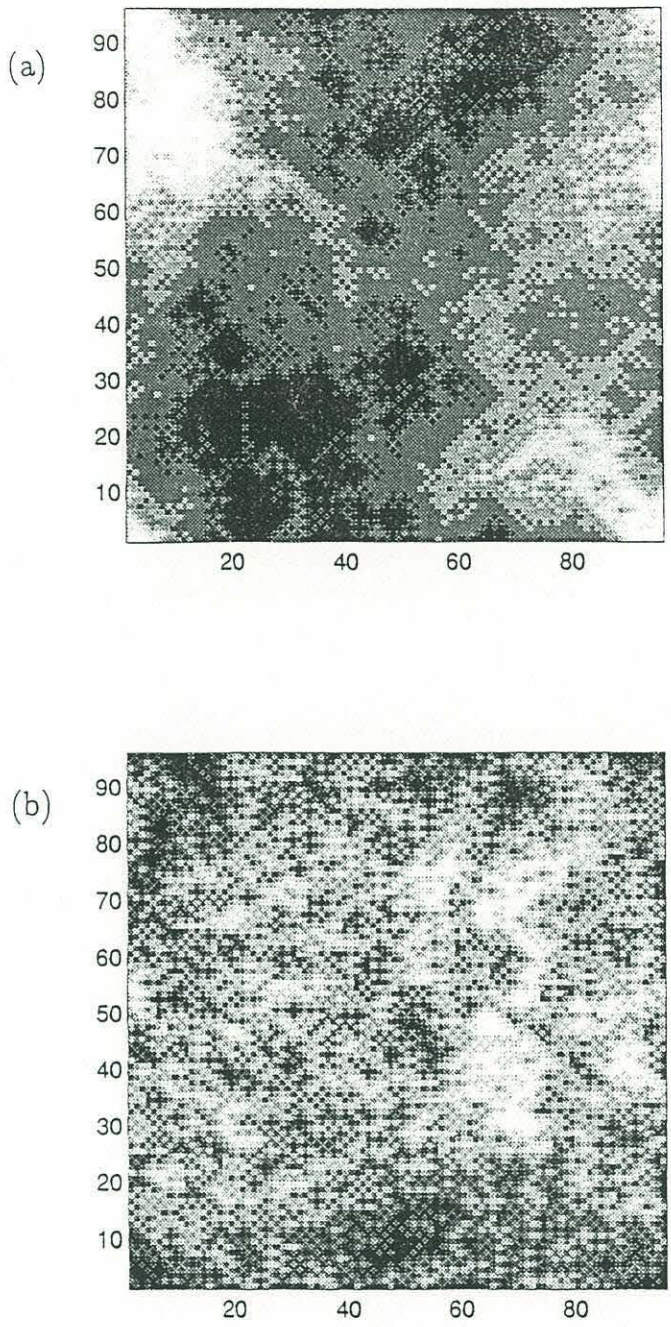

Figure 2-6: Plots of two interfaces taken out of ensembles with 2 different fractal dimensions. The interfaces were obtained from simulations of Model I, performed on lattices of size 96×96. Dark shadings indicate lower then average height and light colors indicate heights greater then average. (a) A sample realization from an ensemble with a fractal dimension of $D = 2.63$. It shows relatively subdued short-wavelength features (formed with $p_+ = 1$). (b) A sample realization from an ensemble with $D = 2.84$. This interface is jagged with relatively more power to short wavelength features (formed with $p_+ = 0.6$).

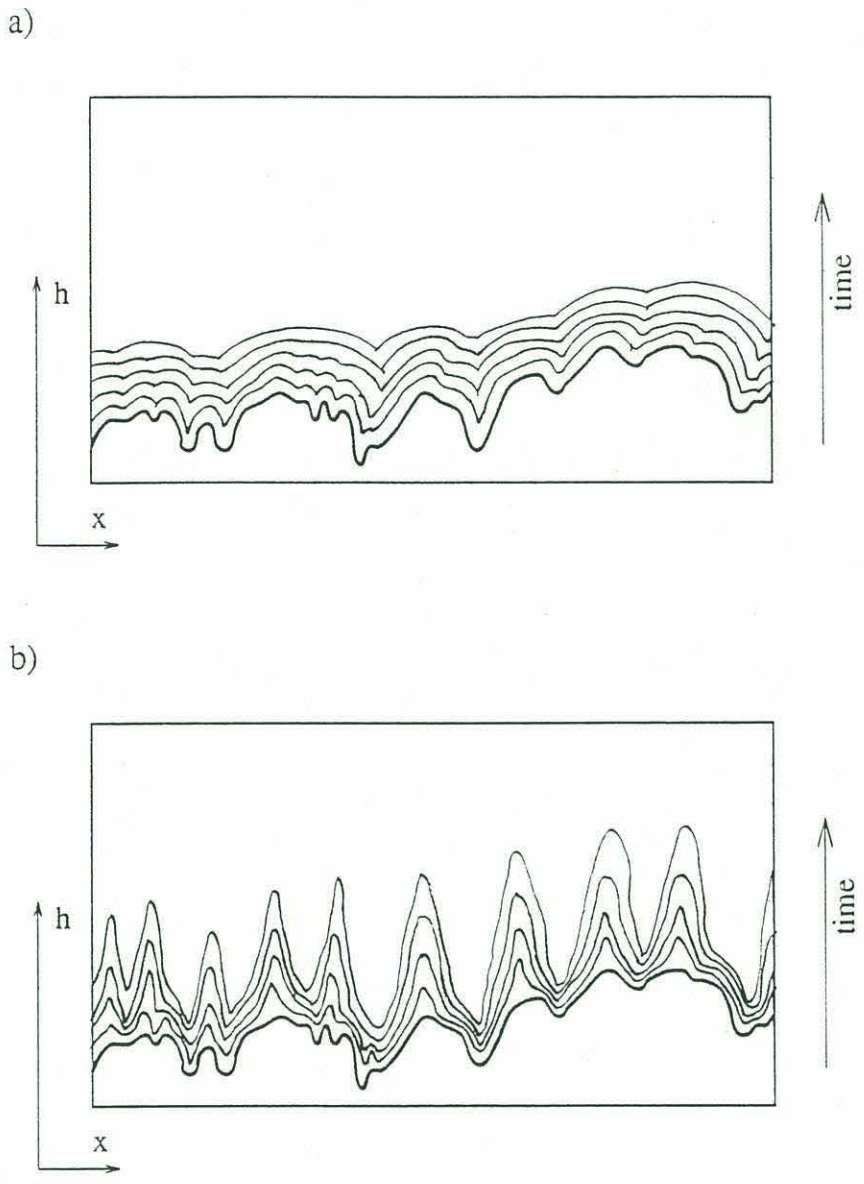

Figure 2-7: A schematic drawing of growth by (a) only reaction controlled kinetics and (b) only transport controlled kinetics (shown in the limit of infinitely fast reaction rates). Both interfaces start from the same initial condition, and successive profiles correspond to propagation in time. (a) is growing normal to its local orientation, with a constant normal growth rate. Large bumps grow at the expanse of small ones, creating parabolas which are joined by discontinuities in ∇h [29]. (b) illustrates the Mullins-Sekerka instability. Protruding features create steep concentration gradients in the fluid phase, thus increasing transport of mineral from the fluid to the interface and causing a further growth of the height of the protrusion, in a positive feedback mechanism. Selected wavelengths grow exponentially in time [42].

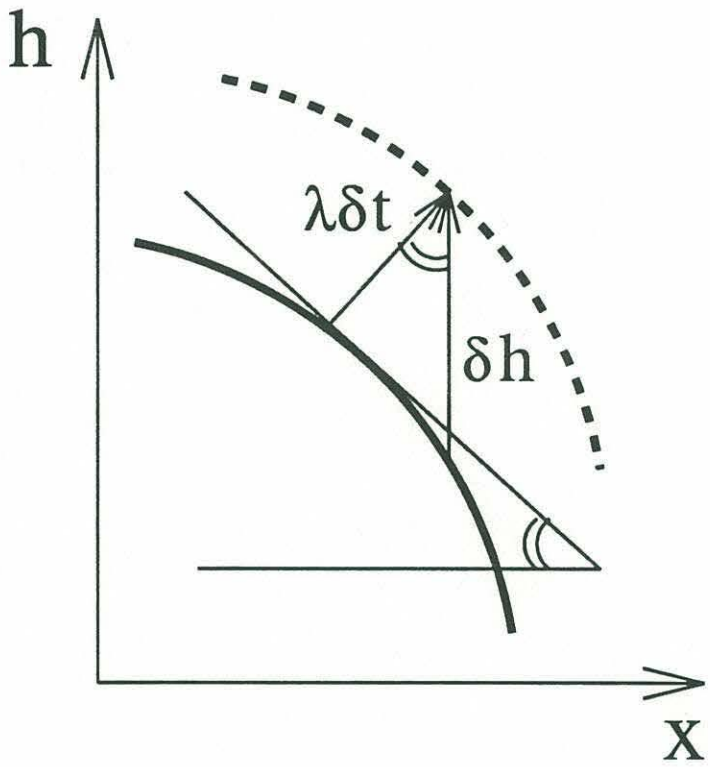

Figure 2-8: In reaction limited kinetics, growth occurs normal to the interface. The position of the interface at time t is indicated by a thick solid line and the position at time $t + \delta t$ by a dashed line. The change in local height, $\delta h(x,t)$, relates to the normal growth velocity, λ, via $\delta h^2 = (\lambda \delta t)^2 + (\lambda \delta t \nabla h)^2$. This relationship can be derived from trigonometrical considerations, where identical angles are indicated by a double solid line [29].

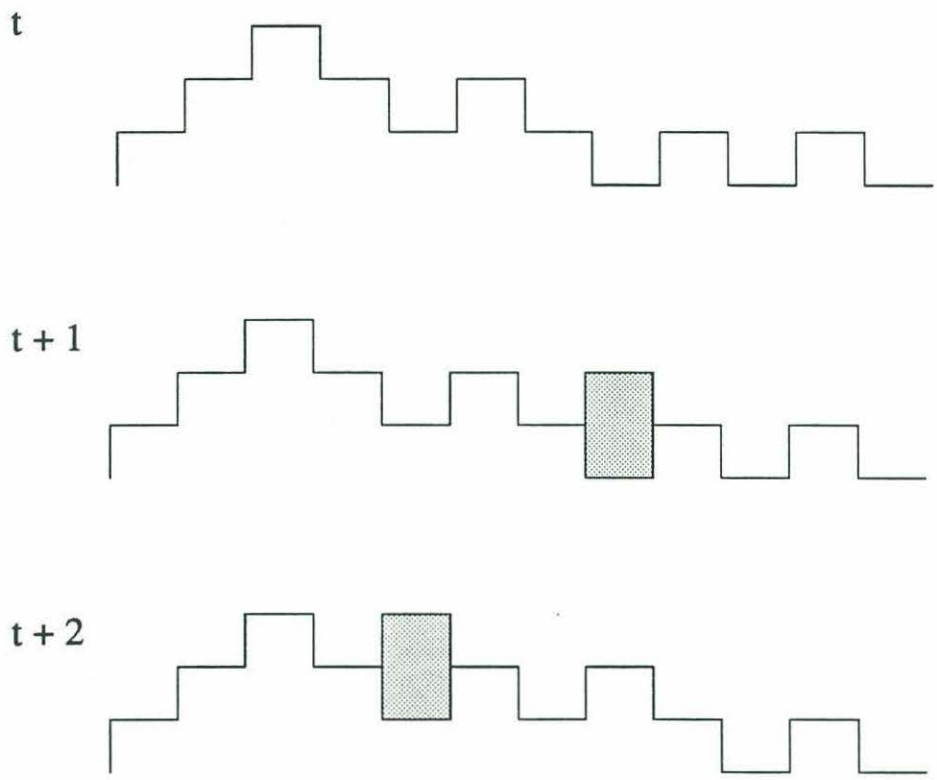

Figure 2-9: A schematic drawing of the discrete-particle deposition "single-step" model of a growing interface embedded in two-dimensional physical space, using periodic boundary conditions. A block of length 2 is added at each successive time step to a site randomly chosen among all sites that are a local minima.

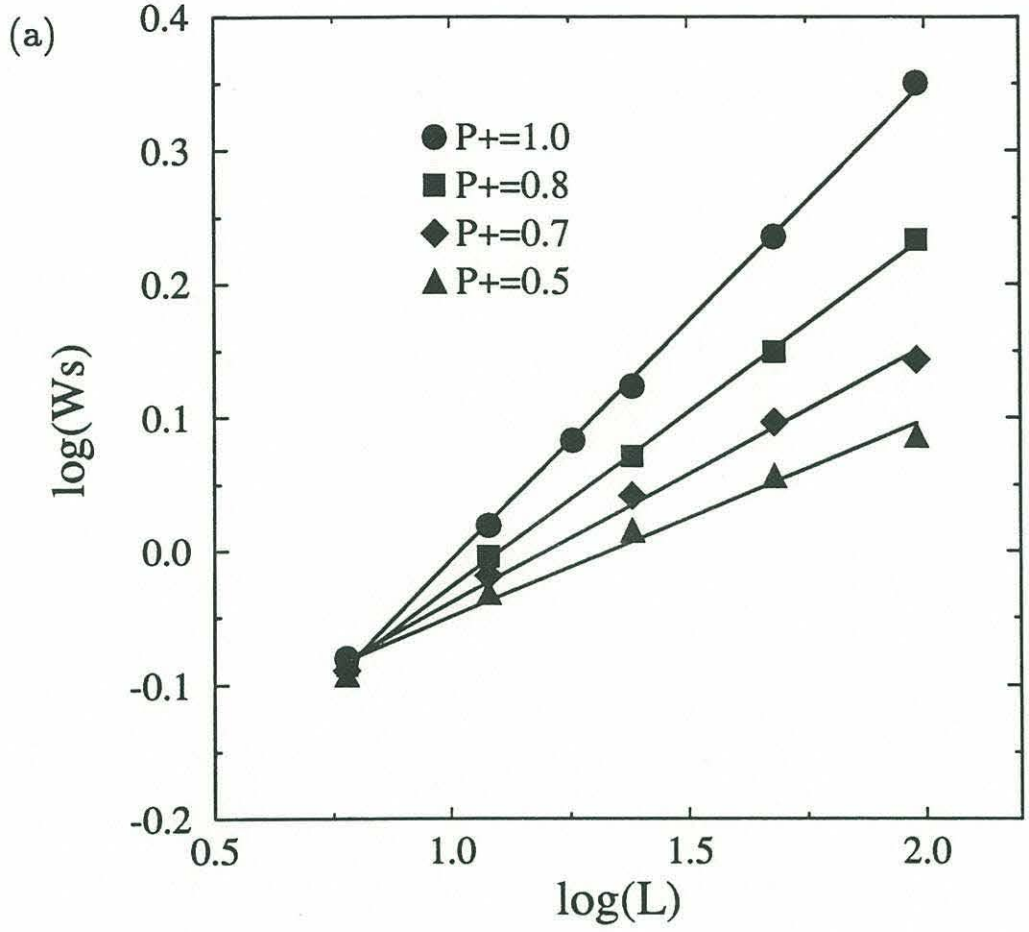

Figure 2-10: (a) Logarithm (base 10) of saturated value of interface width, W_s versus the logarithm of system size L. For self-affine interfaces W_s will have a linear dependence on L with a slope equal to $3 - D$. Different symbols correspond to different $0.5 < p_+ < 1$. Solid lines indicate best fits from linear regression. As p_+ is decreased, the slope of the graph decreases, indicating an increase in the fractal dimension of resulting interfaces with increasing dissolution-deposition ratio. When dissolution begins to balance deposition ($p_+ < 0.6$), the deviations from a linear dependence indicate that the interfaces are not self-affine. Error bars, taken as the standard deviation of the measured width from its steady saturation value, are of the order of the symbol size. (b) A plot of W_s^2 versus $\ln(L)$. Solid lines are best fits from linear regression. This plot demonstrates that a better model to fit the data for high dissolution-deposition ratios ($p_+ \lesssim 0.6$), is $W_s^2 \sim (\ln L)$. This transition is expected to occur when $|\lambda| \to 0$ in 2.13.

(b)

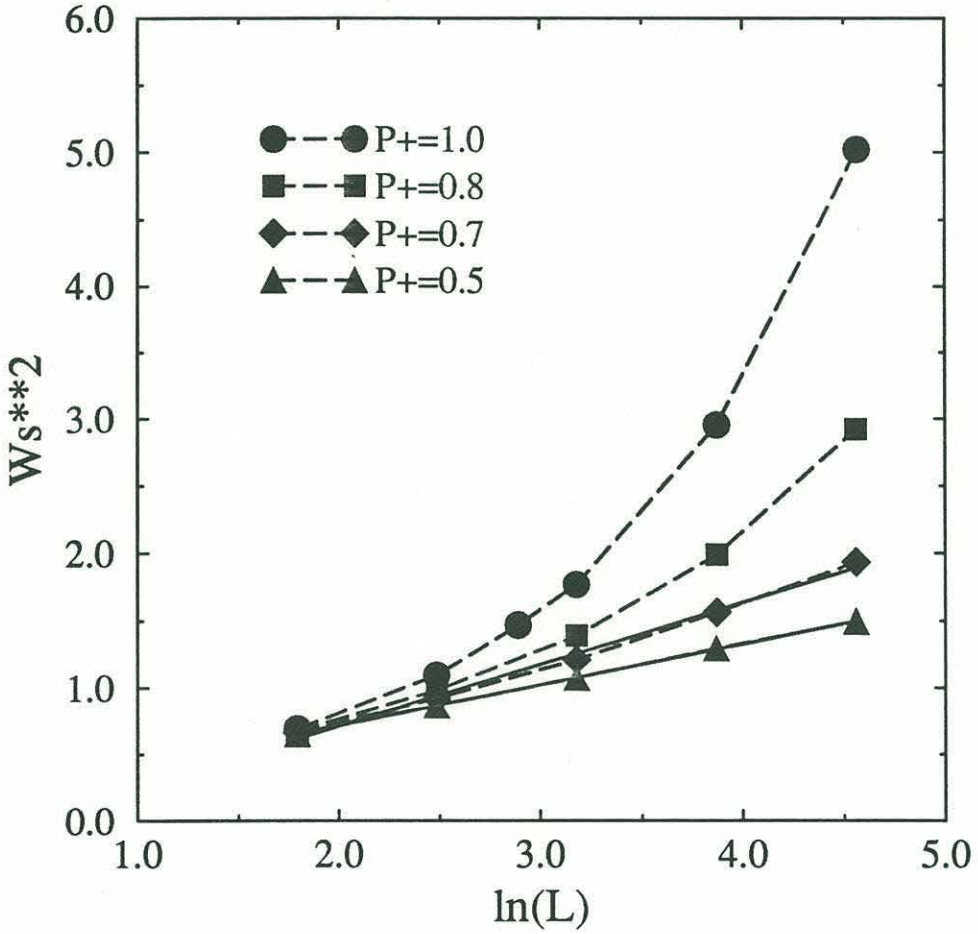

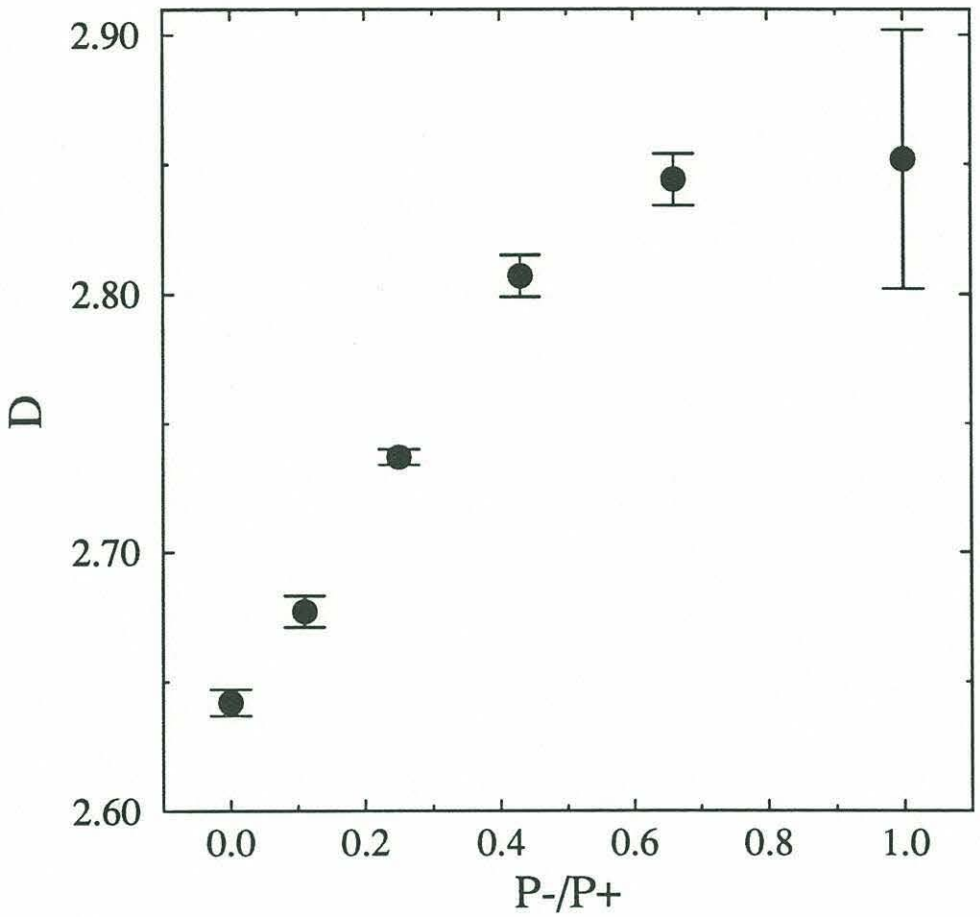

Figure 2-11: Using the slopes of the linear regression best-fits in Figure2-10a, we plot D versus p_-/p_+, the dissolution-deposition ratio rate. Error bars are calculated using the standard deviation from the linear regression best-fits. The fractal dimension of resulting interfaces is seen to increase with p_-/p_+. For $p_-/p_+ = 0$ $D = 2.63 \pm 0.005$. As p_-/p_+ increases D approaches a limiting value of 2.84 ± 0.01. A further increase in p_-/p_+, above $p_-/p_+ \approx 0.7$, results in suspected loss of fractal behavior and a transition to logarithmic dependence, instead of power-law dependence, of W_s on L.

(a)

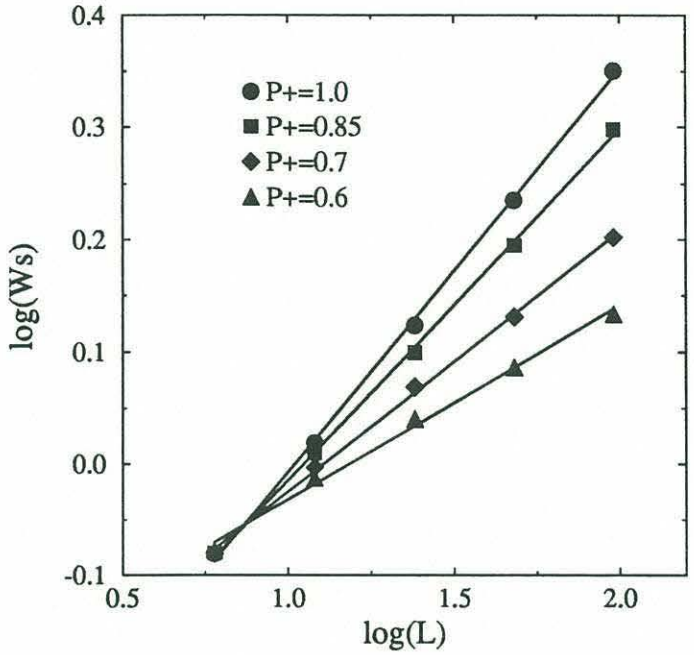

(b)

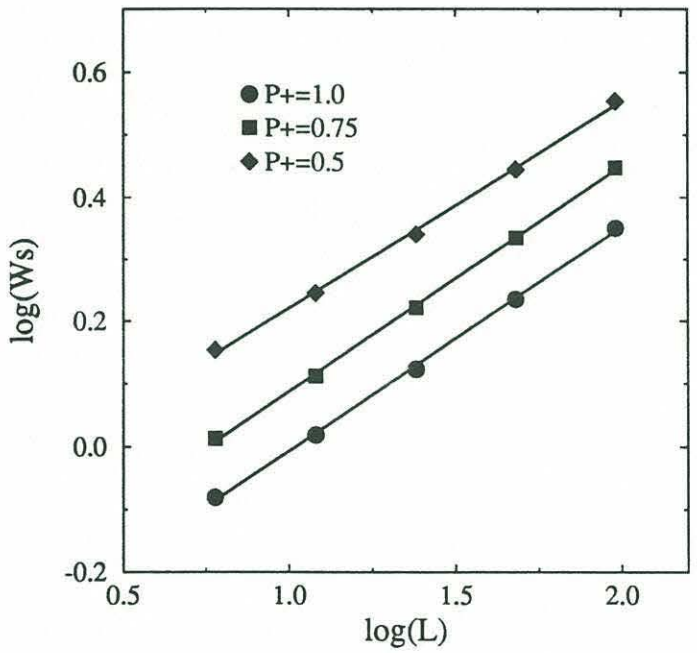

Figure 2-12: Graphs of $\log_{10}(W_s(L))$ as function of $\log_{10}(L)$ for (a) $kT = 1$ and (b) $kT = 100$. Solid lines are best fits from linear regression. For $kT = 1$ the fractal dimension increases (the slope decreases) with decreasing p_+ similarly to results of Model I. For $kT = 100$ the behavior is different: the slope, and hence the fractal dimension, is nearly constant with p_-/p_+.

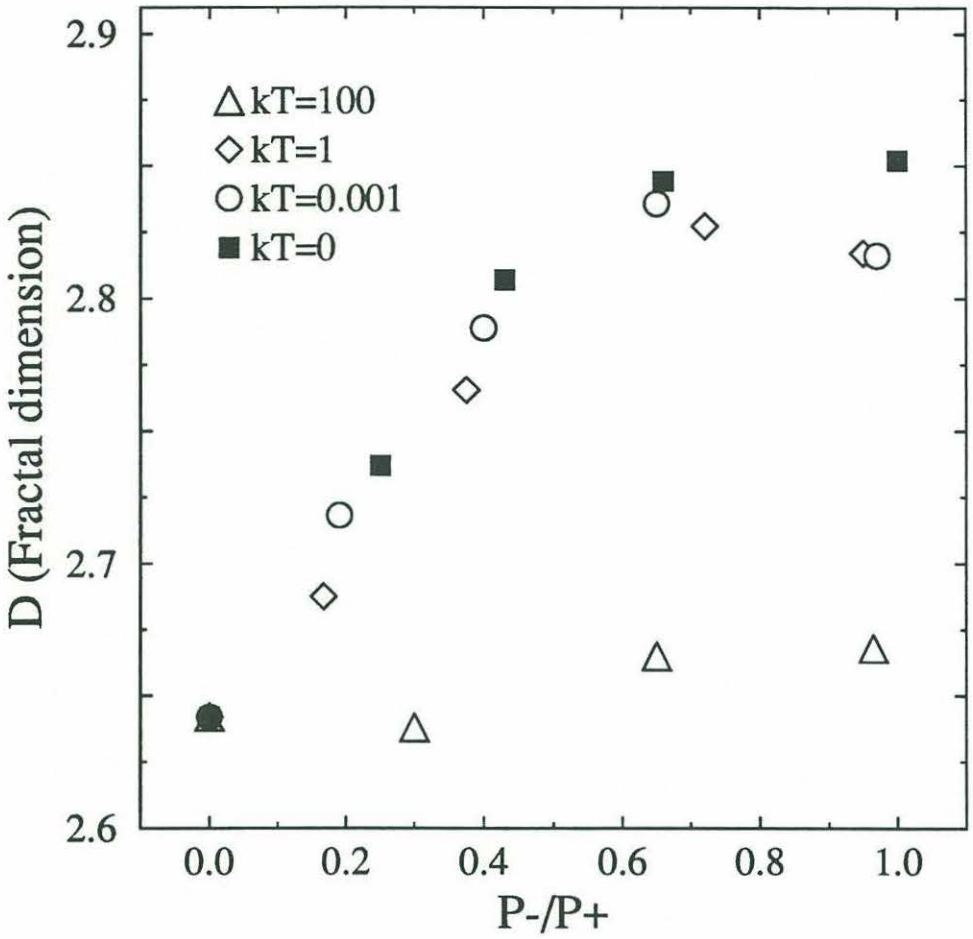

Figure 2-13: Fractal dimension of interfaces as a function of p_-/p_+, the dissolution-deposition ratio. The four curves correspond to four different temperatures: $kT = 10^{-2}, 10^0$, and 10^2 from Model II and $kT = 0$ replotted from Model I. D is deduced from the slopes of plots similar to Figures 2-10 and 2-12. At high temperatures ($kT = 10^2$) the fractal dimension does not change perceptibly as a function of p_-/p_+. For low temperatures, curves follow a trend of increasing D with increased p_-/p_+. Although we plot results from all simulations, interfaces where dissolution and precipitation rates are nearly balanced, when $p_-/p_+ > 0.7$, are probably not fractal, as can be observed in Figures 2-10 and 2-12.

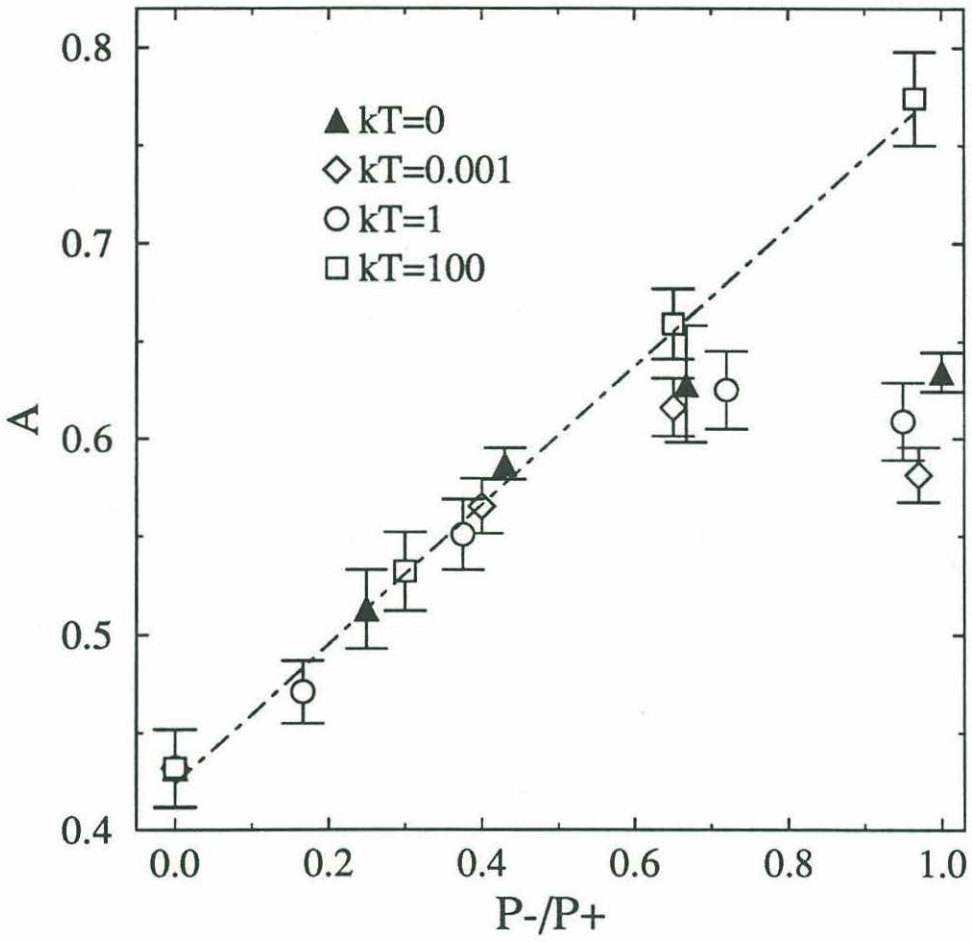

Figure 2-14: A, the "roughness amplitude", calculated from intercepts of lines in Figures 2-10a and 2-12a,b with the width axis, versus the non-dimensional parameter p_-/p_+. The data follows a linear increase of roughness with increased dissolution independent of kT, except for where interfaces are suspected not to be fractal. For low temperatures when $p_-/p_+ \gtrsim 0.7$, the roughness amplitude A reaches a plateau and diverges from the linear trend. Best fit to the linear trend gives $A = (0.355 \pm 0.005)p_-/p_+$.

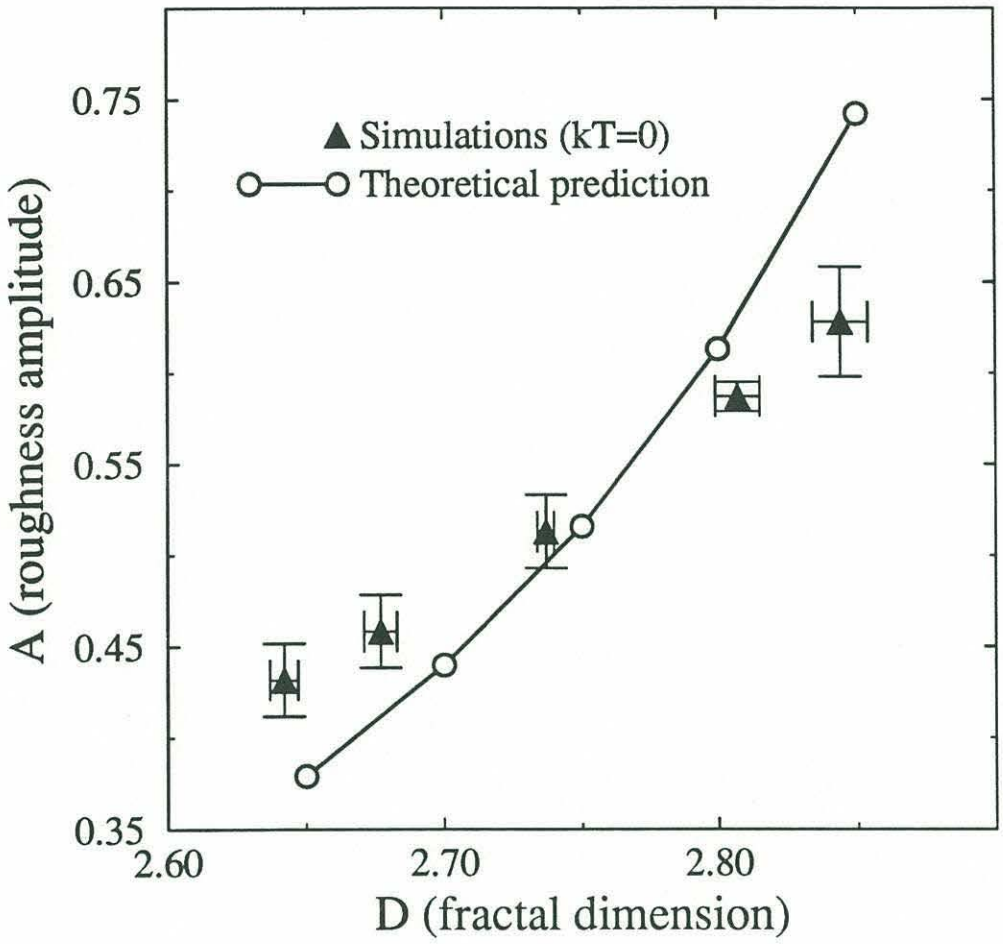

Figure 2-15: For interfaces formed at low temperatures A, the roughness amplitude, is an increasing function of D, the fractal dimension, as can be seen for simulation results for Model I (plotted here as triangles). Thus, when viewed on short length scales, interfaces with high fractal dimensions appear rougher and more strongly fluctuating then interfaces with lower fractal dimensions. Best fit to the linear trend gives $A = (1.01 \pm 0.02)D$. The solid line is theoretical prediction given by equation A.11 using values of $L = 10^4$. Deviation of simulation results from theoretical predictions are probably due to existence of natural cutoffs for fractal behavior, which are not represented in theory.

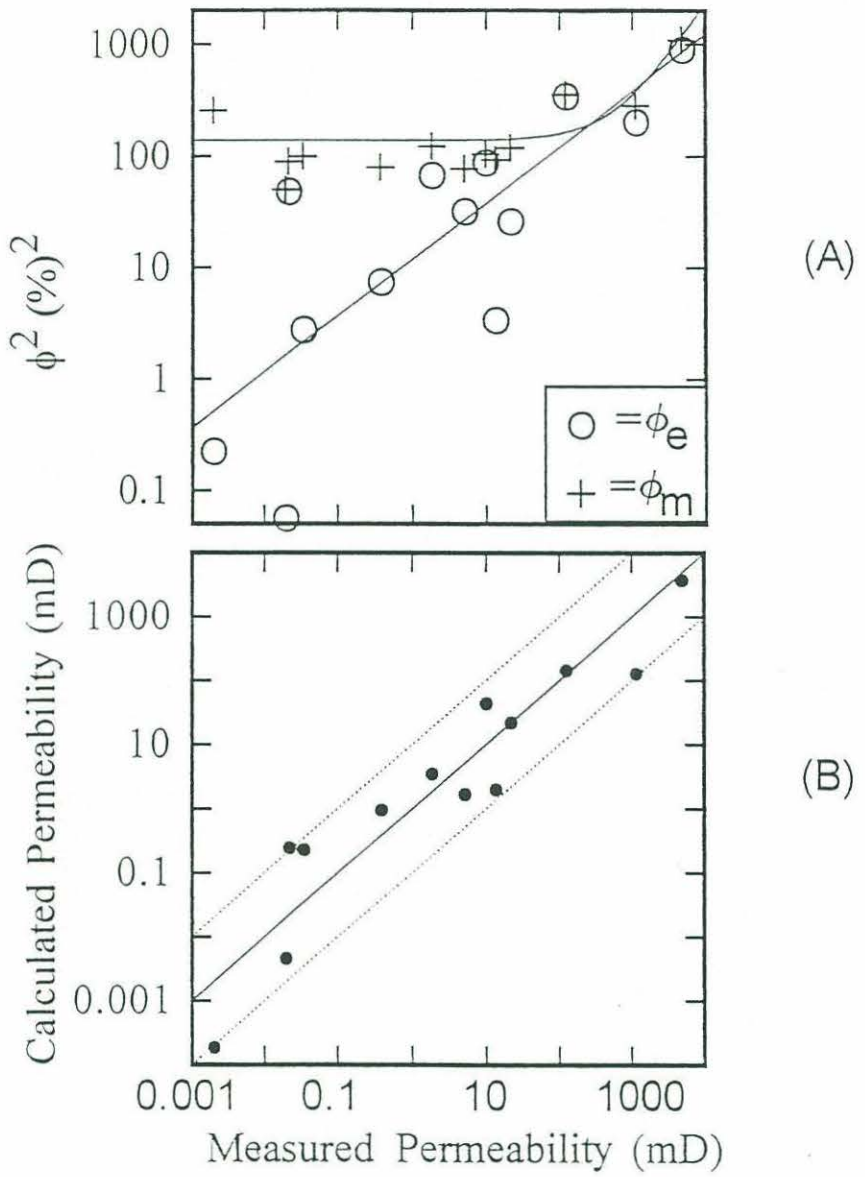

Figure 2-16: After [85]. (A) Demonstrates the lack of correlation between permeability of the samples and their measured total porosity squared, ϕ_m^2, which is conventionally used for permeability predictions [8]. At low porosities permeability changes more then 5 orders of magnitude while ϕ_m^2 is virtually constant. In contrast, correlation with ϕ_e, the Euclidean porosity, is substantially better, since ϕ_e coincides with the void space relevant for transport calculations. (B) Measured permeability versus permeability predicted from equation 2.18. The data cover 7 orders of magnitude in permeability.

Chapter 3

Channeling instability of upwelling melt in the mantle

Abstract

We present results of a theoretical study aimed at understanding melt extraction from the upper mantle. Specifically, we address mechanisms for focusing of porous flow of melt into conduits beneath mid-ocean ridges in order to explain the observation that most oceanic residual peridotites are not in equilibrium with mid-ocean ridge basalt. The existence of such conduits might also explain geological features, termed replacive dunites, that are observed in exposed mantle sections. We show here, by linear analysis, that flow in a chemically reactive porous media is unstable in the presence of a solubility gradient, such as induced by adiabatic ascent of melt underneath mid-ocean ridges. The initially homogeneous flow becomes focused in time to produce elongated high-porosity fingers that act as conduits for transport of fast flowing melt. This instability arises due to a positive feedback mechanism in which a region of slightly higher than average porosity causes increased influx of unsaturated flow, leading to increased dissolution which further reduces the porosity. Even in the presence of matrix compaction and chemical diffusion the instability is demonstrated to be robust. Our analysis also indicates the existence of growing, traveling waves which transport and amplify porosity and concentration perturbations.

3.1 Introduction

Recent work [37, 68, 28, 27] indicates that upwelling mid-ocean ridges basalt (MORB) is in chemical disequilibrium with the upper mantle peridotites that constitute the matrix through which it flows. These observations place constraints on melting and

melt extraction processes at ridges. In order to produce disequilibrium transport, small melt fractions must be efficiently segregated from their source and transported to the crust [28, 27, 75, 26]. Since diffuse porous flow of melt along grain boundaries would lead to extensive chemical reaction and erasure of observed trace element fractionation, some form of focused flow of melt into channels has been proposed to explain extraction of MORB from the mantle [79, 22].

The results of our study imply that one of the mechanisms responsible for focusing may be a coupled chemical-hydrodynamical instability; uniform upwelling of melt flowing through a porous media is unstable when the melt is dissolving some of the matrix through which it is flowing and begins to form elongated, high-porosity channels. In ophiolites, geological observation of dissolution channels (dunites) in chemical equilibrium with MORB, surrounded by mantle peridotites which are not in chemical equilibrium with MORB, confirms that this instability may operate during melt extraction from the mantle at oceanic spreading ridges [33, 31, 36].

Additional mechanisms for melt extraction from the mantle beneath mid-ocean ridges could include (1) hydrofracture (e.g., [56]); (2) focused flow of melt in zones of localized, active deformation (e.g., [81, 35]); and (3) decompaction into melt-filled lenses or veins [73]. Mechanisms 1 and 2 are most probable near and above the brittle/ductile transition in the mantle, where strain becomes localized into shear zones. This is supported by geological evidence that dikes and localized shear zones in the mantle section of ophiolites form mostly "off-axis," away from a spreading ridge, near the brittle-ductile transition, and not in the adiabatically ascending, partially melting mantle beneath a spreading ridge [35, 32]. The third possible mechanism is poorly understood at present, and we are not aware of geological evidence supporting such a hypothesis. In contrast, the reactive infiltration instability is likely to operate in adiabatically upwelling, partially molten, ductile asthenosphere, and there is geologic evidence for focused flow of melt in porous dissolution channels in the mantle section of ophiolites.

It has been known for some time [14, 58, 23] that reactive flow through a soluble porous matrix may result in formation of finger-like embayments along an advancing

reaction front. The mechanism for this instability, termed the "reactive infiltration instability" (RII), is simple: when unsaturated fluid flows through a soluble matrix, a region with slightly higher than average porosity will tend to have an increased influx of fluid, which will increase the rate of dissolution and so increase the porosity even further, in a positive feedback mechanism. Increased velocity in localized regions will cause lateral convergence of fluid upstream of the front into the high-porosity fingers [36].

The characteristic wavelengths and growth rates of the front instability are determined by three parameters: chemical reaction rate, transport rate, and diffusion rate [80]. Reaction and diffusion act to restore the system to equilibrium, while advection acts to make it unstable. When diffusion is strong (compared with reaction), it will act as the main stabilizing mechanism for this instability. The most unstable wavelength in this case is determined by competition between advection (which drives the instability) and diffusion (which tends to smooth perturbations). The ratio between these parameters is termed Pe, the Peclet number.

Work on the RII with reaction-controlled smoothing is sparse but generally indicates that growing fingers are present [24, 80]. Da, the Damköhler number, is the ratio between reaction timescale and advection timescale and is the control parameter in this case. Hoefner and Fogler performed experiments and network simulations which indicate a dependence of coalescing or branching of dissolution channels on Da.

Past work on this subject is not directly applicable to Earth's mantle. The front problem as reviewed above is transient; there is no supply of new grains to the system, and once the reaction front has propagated through the matrix there are no porosity perturbations left. Moreover, the instability (area of disequilibrium) is localized to a single interface between two areas of equilibrium rather than affecting the entire interior solution (although [23] consider the case of a front of finite width). We see no evidence for the existence of such a propagating reaction front in the mantle, no evidence of a sharp reaction zone underneath which the mantle is composed purely of olivine and above which it is composed of pyroxene. In this paper, we investigate instabilities arising in a steady state mantle, where some background porosity, solid

and liquid velocities, and mineral composition can be assumed. In this case there are no transient solution fronts, and if an instability arises, it will be present in the whole region of upwelling and dissolution.

In the mantle, decompression of ascending melt underneath mid-ocean ridges causes an increase in solubility of solid phases with height [72, 36]. Choosing a point along the ascent path of the melt, one can see that dissolution at this point increases the local concentration of soluble components in the melt but never to the point of equilibrium, since upward flow keeps bringing in undersaturated melt. This small departure from equilibrium allows an instability to occur, in the same manner as the feedback mechanism for the dissolution front described above. However, instead of having a fingered front, we expect the instability to occur within the region of melt transport wherever there exists a gradient in solubility.

In this paper we study a porous matrix confined in a box where grains are soluble, and there is a constant flux of melt from the lower end of the box. As solid material dissolves, the matrix is allowed to contract by compaction so as to keep the porosity constant in the steady state, with additional grains supplied at the top of the box. The solubility of the grains increases linearly with increasing height in order to approximate the increase in solubility induced by adiabatic ascent of melt decompressing in the mantle. Thermal melting of the solid phases, as distinguished from reactive dissolution, is neglected, as is viscous shearing of the solid phases and advective heat transport by melt. In what follows, we present the governing equations, nondimensionalize them, find a possible steady state, and do a linear stability analysis.

Two interesting unstable features are then shown to coexist:

1. The system is shown to be linearly unstable to small perturbations, causing focusing of flow in elongated high-porosity channels, where the vertical dimension is generally much longer than the horizontal dimension, establishing conduits for ascent of melt. These channels form provided that the characteristic length for chemical equilibration is smaller than a characteristic length for compaction. A calculation using characteristic values for Earth's mantle predicts that the condition for formation

of the instability is probably met and that the reaction-infiltration instability may play an important role in forming conduits for melt extraction from the mantle.

2. The system gives rise to unstable propagating waves, which in the limit of no dissolution are linear compaction waves [76]. The addition of dissolution during porous flow gives rise to waves whose amplitude increases with time, providing dissolution features which propagate in space with a finite phase and group velocity. These results suggest a mechanism for spontaneous nucleation of "magmons" [71, 78].

Finally, we discuss the application of our study to focusing of melt flow in the mantle beneath mid-ocean ridges.

3.2 Formulation of the Problem

3.2.1 General Equations

In this section we present a set of equations describing the essence of reactive flow through a soluble porous medium with a gradient in solubility. The setup of the problem is given in Figure 3-1. Fluid is driven upward by a pressure gradient, entering the soluble matrix at $z = 0$ and leaving it at $z = L$. With decreasing pressure the fluid has increasing ability to dissolve the porous matrix. Since we would like to investigate a steady state and deviations from it, we have allowed for compaction, though it is by no means crucial for the growth of the instability. Compaction provides a relatively simple steady state where dissolution increases the porosity and compaction works to decrease it.

The set of governing equations presented below closely follows the notation and form of some previous work on deformable porous media [44, 71, 76, 77]. This approach views the coupled solid-fluid system as two interpenetrating fluids with vastly different viscosities and is valid for length scales much larger than a pore size. Inertial effects have been assumed to be negligible.

Conservation of mass. Conservation of the solid phase is given by

$$\frac{\partial \rho_s(1-\phi)}{\partial t} + \nabla \cdot [\rho_s \mathbf{V}(1-\phi)] = -\sum_i \Gamma_i, \tag{3.1}$$

where ϕ is the porosity, ρ_s is the solid density in kg m^{-3}, $\mathbf{V}$ is the solid grain velocity vector and Γ_i is the mass transfer rate of mineral i from solid to fluid in kg m^{-3} s^{-}1.

Conservation of fluid mass is given by

$$\frac{\partial \rho_f \phi}{\partial t} + \nabla \cdot (\rho_f \mathbf{v} \phi) = \sum_i \Gamma_i, \tag{3.2}$$

where ρ_f is the density of the fluid and $\mathbf{v}$ is the fluid velocity vector.

Component conservation equations in the fluid phase consist of three contributions: diffusion, advection, and a chemical source/sink term:

$$\frac{\partial \rho_f \phi c_i}{\partial t} + \nabla \cdot (\rho_f \phi \mathbf{v} c_i) = \nabla \cdot (D_i \rho_f \phi \nabla c_i) + \Gamma_i, \tag{3.3}$$

where D_i is the diffusion coefficient of component i in the fluid and c_i is the mass fraction of dissolved component i in the fluid, with $\sum_i c_i = 1$.

Each individual component is also conserved in the solid phase such that

$$\frac{\partial \rho_s (1-\phi) c_i^s}{\partial t} + \nabla \cdot [\rho_s (1-\phi) \mathbf{V} c_i^s] = \nabla \cdot [D_i^s \rho_s (1-\phi) \nabla c_i^s] - \Gamma_i, \tag{3.4}$$

where c_i^s and D_i^s are the mass fraction and the diffusion coefficient of component i in the solid phase and $\sum_i c_i^s = 1$.

If one defines a partition coefficient $K_i = c_i^s / c_i$ and assumes chemical equilibrium between the solid and the fluid phases, then previous formulations can be rederived (e.g., [44]). However, since we are interested in nonequilibrium chemical reactions, we shall not follow that practice.

Mass transfer by chemical reaction. Assuming first-order chemical reaction, one can write the rate of mass transfer as

$$\Gamma_i = -R_i A(\mathbf{x}, t) \left[c_i - c_{eq_i}(z) \right], \tag{3.5}$$

where R_i is the reaction rate constant of component i in kg m^{-2} s^{-1}, A is the specific area (m^2/m^3) available for reaction, and $c_{eq_i}(z)$ is the equilibrium concentration of mineral i in the fluid given in mass fraction.

Solubility is taken to be a linear function of height, as approximately the case for melt that is adiabatically rising [72, 36]:

$$\frac{\partial c_{eq_i}(z)}{\partial z} = \beta_i, \tag{3.6}$$

where β_i is a proportionality coefficient describing the steepness of the solubility gradient with units of m^{-1}.

Darcy's law. Darcy's law relates the pressure p and the relative velocity between the fluid and the solid matrix:

$$\phi(\mathbf{v} - \mathbf{V}) = -\frac{k_\phi}{\mu}\nabla p, \tag{3.7}$$

where the permeability k_ϕ of the porous medium is usually taken to be a power law function of the porosity $k_\phi = d^2\phi^n/b$, with d a typical grain size, n between 2 and 3, and b a constant (e.g., [8, 88]). μ is the viscosity of the fluid and p is the pressure in excess of hydrodynamic pressure.

Matrix deformation. The closing equation is the momentum conservation equation which relates pressure changes to the rate of compaction, viscous deformation of the solid phase and body forces acting on the system [44, 76]:

$$\frac{\partial p}{\partial x_i} = \frac{\partial}{\partial x_j}\eta\left(\frac{\partial V_i}{\partial x_j} + \frac{\partial V_j}{\partial x_i}\right) + \frac{\partial}{\partial x_j}(\xi - \frac{2}{3}\eta)\nabla \cdot \mathbf{V} - (1-\phi)\Delta\rho g\delta_{i3}, \tag{3.8}$$

where η, ξ are the solid phase shear and bulk viscosities and $\Delta\rho = \rho_s - \rho_f$ is the buoyancy difference. Equation 3.8 states that any change in the pressure field can be expressed as the force the solid exerts on the fluid. In a rigid material where the grain velocity goes to zero ($\mathbf{V} \to 0$), the viscosity of the matrix will go to infinity ($\xi, \eta \to \infty$) and the product will always remain bounded.

The resulting set of dynamical equations are similar to those introduced by workers on compaction of molten rocks [44, 76], but here a specification of a dissolution mechanism (equation 3.5) with increasing dissolution as a function of height (equation 3.6) brings in interesting behavior. Our goal is to study the combined effect of dissolution and porous flow, rather than to concentrate on the compaction effects.

3.2.2 Simplified Equations

For simplicity, we assume the existence of a fully soluble solid phase composed solely of one mineral ($c^s = 1$) which can chemically react with the fluid by dissolution or precipitation, with first-order kinetics. Since only one reacting component is present,

the subscript i will be dropped from here on. The fluid phase is composed of a carrier fluid with mass fraction $1 - c$. The carrier fluid component does not enter the solid phase. The dissolved mineral has mass fraction c and effective reaction rate $R_{\text{eff}} = RA$, where we assume that reactive surface area can be taken as constant to leading orders.

The density of the fluid phase is presumed constant as the composition of the melt changes due to chemical reaction. This assumption is approximately correct during dissolution reactions involving basaltic melt and mantle minerals. The solid phase density in a one component system is also a constant.

Neglecting matrix shear, the momentum conservation equation 3.8 is

$$\nabla p = (\xi + \frac{4}{3}\eta)\nabla \mathcal{C} - (1 - \phi)\Delta\rho g\hat{k}, \tag{3.9}$$

where we have defined a compaction rate as $\mathcal{C} = \nabla \cdot V$ and $\hat{k}$ is a unit vector in the vertical direction.

Equations 3.1-3.5 and 3.7 can now be written as

$$\begin{aligned}
\frac{\partial \phi}{\partial t} + \mathbf{V} \cdot \nabla \phi &= (1 - \phi)\mathcal{C} - R_{\text{eff}}(c - c_{\text{eq}}(z))/\rho_s, & (3.10)\\
\frac{\partial \phi}{\partial t} + \nabla \cdot (\mathbf{v}\phi) &= -R_{\text{eff}}(c - c_{\text{eq}}(z))/\rho_f, & (3.11)\\
\phi\frac{\partial c}{\partial t} + \phi\mathbf{v} \cdot \nabla c &= D\nabla \cdot (\phi\nabla c) - (1 - c)R_{\text{eff}}(c - c_{\text{eq}}(z))/\rho_f, & (3.12)\\
-\phi(\mathbf{v} - \mathbf{V}) &= \frac{k_\phi}{\mu}\left[(\xi + \frac{4}{3}\eta)\nabla \mathcal{C} - (1 - \phi)\Delta\rho g\hat{k}\right], & (3.13)
\end{aligned}$$

where 3.12 is a result of subtracting 3.2 from 3.3, equation 3.4 is identical to 3.1 in the case of $c^s = 1$ and equation 3.13 is a result of substituting 3.9 in 3.7.

Boundary conditions. In general, equations 3.10-3.13 will require five boundary conditions to solve for $\mathbf{v}$, $\mathcal{C}$, ϕ, and c. Mass conservation requires that the flux across a boundary be continuous or balanced by a source or a sink. Flux boundary conditions include impermeable, rigid, or "free flux" boundary conditions. When the boundary is impermeable, the normal flux is zero either because $k_\phi = 0$ or because $\nabla p \cdot \hat{n} = 0$, where $\hat{n}$ is the direction normal to the boundary. The latter condition poses constraints on $\nabla \mathcal{C} \cdot \hat{n}$. At a rigid boundary $\mathcal{C} = 0$, and so in the absence of

dissolution and matrix flow, a rigid boundary has also a constant porosity (equation 3.10). Finally, a free-flux boundary has $\nabla C \cdot \hat{n} = 0$ and yields no resistance to volume changes for the normal flux. In addition to the total flux boundary conditions, mass conservation poses constraints on flux of individual components in the fluid. These constraints translate to specification of concentration of solute in incoming or outgoing fluid.

Nondimensionalization. In nondimensionalizing equations 3.10-3.13 we shall use the following definitions: Assuming zero solubility at $z = 0$, from 3.6,

$$c_{\mathrm{eq}}(z) = \beta z.$$

The change in solubility of the matrix between the bottom and top of a box of size L is defined as $c_\delta = c_{\mathrm{eq}}(L) - c_{\mathrm{eq}}(0)$, and so

$$c_\delta = L\beta. \tag{3.14}$$

The only imposed parameter value in 3.14 is β, the solubility gradient, known from thermodynamic calculations to be of the order of 2×10^{-6} m^{-1} (an account of calculations made by [36] is given in Appendix B). If we choose to investigate a small-scale box, then c_δ, the change in solubility across the box, will be small as well; $c_\delta \approx 0.2$ over the vertical extant of decompression melting, roughly the upper 75 km of Earth's mantle beneath oceanic spreading ridges. Correspondingly over 100 m, c_δ is of order 10^{-3}.

Porosity is nondimensionalized to a characteristic value, ϕ_0, of the order of 10^{-2} in the partially molten upper mantle beneath spreading ridges (e.g., [27, 75]),

$$\phi = \phi_0 \phi'.$$

Permeability is non-dimensionalized to this porosity

$$k_0 = d^2 \phi_0^n / b.$$

Fluid velocity is characterized to be of the order of velocity driven by gravity forces such that

$$\phi_0 w_0 = \frac{k_0}{\mu} \Delta \rho g.$$

Characteristic solid velocity is taken as

$$V_0 = \phi_0 w_0 c_\delta.$$

Finally, we define a compaction length h to be

$$h^2 = \frac{k_0}{\mu}(\xi + 4\eta/3),$$

where $h \to 0$ is an infinitely weak matrix, which compacts instantly, and $h \to \infty$ is a rigid medium; h has a typical value of 100-1000 m in the mantle [44].

The nondimensional variables will be denoted by primed letters:

$$\begin{aligned}
(x, z) &= L(x', z') \\
t &= \frac{L}{w_0 c_\delta} t' \\
C &= \frac{V_0}{L} C' \\
v &= w_0 v' \\
V &= V_0 V' \\
c &= c_\delta c' \\
c_{\mathrm{eq}} &= c_\delta z'
\end{aligned}$$

Where the fact that time is scaled to $1/c_\delta$ is a result of our choice to scale time to the characteristic time for change in porosity due to dissolution. In the limit of no gradient of solubility (and thus no dissolution), $c_\delta \to 0$, and the characteristic timescale for change in porosity due to dissolution goes to infinity.

We now write the nondimensional equations:

$$\frac{\partial \phi'}{\partial t} + \phi_0 \mathbf{V}' \cdot \nabla \phi' = (1 - \phi_0 \phi') C' - Da \frac{\rho_f}{\rho_s}(c' - z'), \tag{3.15}$$

$$c_\delta \frac{\partial \phi'}{\partial t} + \nabla \cdot (\phi' \mathbf{v}') = -c_\delta Da(c' - z'), \tag{3.16}$$

$$c_\delta \phi' \frac{\partial c'}{\partial t} + \phi' \mathbf{v}' \cdot \nabla c' = -(1 - c_\delta c') Da(c' - z') + \frac{1}{Pe} \nabla \cdot (\phi' \nabla c'), \tag{3.17}$$

$$\phi'(\mathbf{v}' - \phi_0 \mathbf{V}') = -\phi'^n [\alpha \nabla C' - (1 - \phi_0 \phi') \hat{k}], \tag{3.18}$$

where Da is defined as advection time across a box versus reaction time:

$$Da = \frac{R_{\text{eff}} L}{\phi_0 w_0 \rho_f}. \tag{3.19}$$

Alternatively, if we define the "reaction length,"

$$L_{\text{eq}} = \frac{\phi_0 w_0 \rho_f}{R_{\text{eff}}}, \tag{3.20}$$

to be the length scale over which a perturbation in concentration will equilibrate with the solid matrix if it is traveling at speed w_0, then the Damköhler number is simply the system size in reaction lengths. The reaction length and compaction length are the two inherent length scales in this problem.

The Peclet number is defined as the advection rate versus diffusion rate

$$Pe = \frac{w_0 L}{D}. \tag{3.21}$$

Finally, we define a rigidity parameter α, which is a combined measure of the change in solubility over one compaction length and the size of a system L relative to a compaction length,

$$\alpha = \frac{h^2}{L^2} \times c_\delta = \frac{h}{L} \times c_h, \tag{3.22}$$

where $c_h = \beta h$ is the change in solubility over one compaction length. Since L can be as small as we choose, α is not necessarily small even if c_h is small. When $\alpha \to 0$, the matrix is easily compacted, and when $\alpha \to \infty$, the matrix is effectively rigid.

We then neglect all terms of order ϕ_0 (since ϕ_0 is of order of 10^{-2}). The effects of retaining terms of order ϕ_0 when $\phi_0 \ll 1$ have been shown to be small for many problems [7, 70, 76]. In addition, we temporarily neglect diffusion, $Pe \to \infty$, so that 3.15–3.18 become, dropping the primes,

$$\frac{\partial \phi}{\partial t} = \mathcal{C} - Da \frac{\rho_f}{\rho_s}(c - z), \tag{3.23}$$

$$c_\delta \frac{\partial \phi}{\partial t} = -\nabla \cdot (\phi \mathbf{v}) - c_\delta Da(c - z), \tag{3.24}$$

$$c_\delta \phi \frac{\partial c}{\partial t} = -\phi \mathbf{v} \cdot \nabla c - (1 - c_\delta c) Da(c - z), \tag{3.25}$$

$$\phi \mathbf{v} = -\phi^n [\alpha \nabla \mathcal{C} - \hat{k}]. \tag{3.26}$$

The value of c_δ increases with system size, but since we are interested in physical systems that have an upper limit in size (the whole region of decompression melting $\approx$ 75 km), c_δ will be less than or equal to the concentration change over that whole region, $c_\delta \leq O(10^{-1})$, and so will be taken here as a small enough parameter to allow for expansion techniques.

Equation 3.23 tells us that the important timescale in the problem is the timescale over which porosity changes. This happens due to compaction on the one hand and reaction on the other. Equation 3.24 predicts that the timescale for divergence of flux is fast compared to that of changing the porosity, since c_δ is a small parameter. Equation 3.25 predicts that the concentration in the fluid is nearly constant with time. Finally, 3.26 tells us that pressure gradients will manifest themselves as gradients in compaction rates.

3.3 Steady State

We seek unidirectional steady solutions to 3.23-3.26, of the form

$$[\bar{\phi}(z), \bar{w}(z), \bar{c}(z), \bar{C}(z)] = [\phi^0(z), w^0(z), c^0(z), C^0(z)] + c_\delta[\phi^1(z), w^1(z), c^1(z), C^1(z)], \tag{3.27}$$

where $\bar{w}(z)$ is the fluid velocity in the z direction, $w^0(z)$ is the zeroth-order solution of the steady state, and $c_\delta w^1(z)$ is a small parameter correction to it; c_δ will be shown to be unimportant in the initial steady state solution but is included here in order to simplify the subsequent linear stability analysis.

Equations 3.23-3.26 will be solved with a physical picture in mind: at the bottom of the melt column, where melt is entering in equilibrium with its surroundings, there is no dissolution and porosity is constant. Thus we require a "rigid boundary" condition $\mathcal{C} = 0$, and a chemical constraint on the concentration field at $z = 0$. These lead to the desired constant porosity at $z = 0$. We also require that fluid flux is continuous across this boundary. Taking into account that only three boundary conditions are needed, now that diffusion of solute and divergence of porosity have

been neglected, the boundary conditions take the form of:

$$\bar{\phi}(0) = 1, \quad \bar{w}(0) = 1, \quad \bar{c}(0) = 0. \tag{3.28}$$

Solutions for the zeroth-order flux are obtained from the fluid conservation equation 3.24 and the boundary conditions 3.28

$$w^0 \phi^0 = 1, \tag{3.29}$$

From the solute concentration equation 3.25 one then finds that

$$c^0(z) = \frac{1}{Da}(e^{-DaZ} - 1) + z, \tag{3.30}$$

where $1/Da$ is a measure of the thickness of a boundary layer, i.e., the dimensionless reaction length ($1/Da = L_{\rm eq}/L$).

One can see from 3.30 that nowhere (except for $z = 0$) does $c^0(z) = z$, the equilibrium value. Rather there is always a deviation of the concentration from the equilibrium concentration, and when the nondimensional height $z \gg L_{\rm eq}/L$, the deviation from equilibrium approaches a constant undersaturation (Figure 3-2). At any point along the ascent path of the melt, reaction tends to restore the system to equilibrium, but more undersaturated fluid is brought from below to drive the system away from equilibrium. This solution suggests that some degree of disequilibrium will exist as long as the reaction length is significantly larger than the continuum length scale (i.e., the grain scale). When $L_{\rm eq} \leq O(d)$, then the system is effectively in local equilibrium. Note that we will show that the channeling instability arises even under conditions of effectively local equilibrium.

For simplicity, we shall assume that the nondimensional height is $z \gg L_{\rm eq}/L$ such that any boundary layer effects are negligible. Estimates of the reaction length that are reasonable for Earth are sensitive to assumptions about the microscopic distribution of melt and solid (see Appendix B). For a range of parameters, Table 3.1 suggests that the equilibration length may range from much less than a millimeter to meters. So even if our system size is of the order of a compaction length, most parameter ranges indicate that significant boundary layers are not expected. Thus

we can approximate

$$c^0(z) \approx z - \frac{1}{Da}. \tag{3.31}$$

The zeroth-order steady state compaction rate is calculated from 3.23 to be nearly constant for $z \gg L_{\rm eq}/L$

$$\mathcal{C}^0(z) = \frac{\rho_f}{\rho_s}(e^{-DaZ} - 1) \approx -\frac{\rho_f}{\rho_s}. \tag{3.32}$$

From 3.26 the zero-order steady state porosity is approximately constant:

$$\phi^0(z) = \left(\frac{\rho_f}{\rho_s}\alpha Da\ e^{-DaZ} + 1\right)^{-1/n} \approx 1. \tag{3.33}$$

Finally, from 3.29 the velocity is also approximately constant:

$$w^0(z) \approx 1. \tag{3.34}$$

The zeroth-order steady state of constant porosity and upwelling velocity is sustained by the competition between porosity formed by dissolution and destroyed by compaction. Since compaction rate is the gradient of grain velocity, constant compaction means that grains descend with increasing speed as a function of height, which exactly balances the net increase in dissolution with height.

The c_δ-order terms of the steady state can be easily obtained from 3.23-3.26 using the zeroth-order solutions and boundary conditions of $\phi^1(0) = w^1(0) = c^1(0) = 0$, but their detail is of no particular interest here, since in the stability analysis perturbations to terms of order c_δ are negligibly small compared to perturbations to terms of order 0.

3.4 Linear Analysis without diffusion

We shall perform a linear stability analysis of 3.23-3.26 assuming that all variables can be expressed as their steady state value plus small deviations:

$$[\phi'(\mathbf{x},t), w'(\mathbf{x},t), u'(\mathbf{x},t), c'(\mathbf{x},t), \mathcal{C}'(\mathbf{x},t)] =$$
$$[\bar{\phi}(z), \bar{w}(z), 0, \bar{c}(z), \bar{\mathcal{C}}(z)] + \epsilon[\hat{\phi}(\mathbf{x},t), \hat{w}(\mathbf{x},t), \hat{u}(\mathbf{x},t), \hat{c}(\mathbf{x},t), \hat{\mathcal{C}}(\mathbf{x},t)], \tag{3.35}$$

where $\epsilon \ll 1$ and the steady state values are defined by 3.27-3.34.

Keeping $O(\epsilon)$ terms and discarding terms of $O(c_\delta\epsilon, \epsilon^2)$, the perturbation equations take the following form:

$$\frac{\partial\hat{\phi}}{\partial t} = \hat{C} - Da\frac{\rho_f}{\rho_s}\hat{c}, \tag{3.36}$$

$$0 = \frac{\partial\hat{w}}{\partial z} + \frac{\partial\hat{\phi}}{\partial z} + \frac{\partial\hat{u}}{\partial x}, \tag{3.37}$$

$$0 = -\hat{\phi} - \hat{w} - \frac{\partial\hat{c}}{\partial z} - Da\hat{c}, \tag{3.38}$$

$$\hat{w} = (n-1)\hat{\phi} - \alpha\frac{\partial\hat{C}}{\partial z}, \tag{3.39}$$

$$\hat{u} = -\alpha\frac{\partial\hat{C}}{\partial x}. \tag{3.40}$$

In solving the perturbation equations 3.36-3.40 we shall assume that all variables have the form of

$$[\hat{w}(\mathbf{x},t), \hat{u}(\mathbf{x},t), \hat{\phi}(\mathbf{x},t), \hat{c}(\mathbf{x},t), \hat{C}(\mathbf{x},t)] = [\tilde{w}(z), \tilde{u}(z), \tilde{\phi}(z), \tilde{c}(z), \tilde{C}(z)]e^{\sigma t}e^{ilx}, \tag{3.41}$$

where σ is the nondimensional growth rate of the perturbation and l is the nondimensional wavenumber in the horizontal direction. Equation 3.38 can be rewritten using 3.36, 3.39, and 3.40 to be a function of $\tilde{\phi}, \tilde{C}$ only

$$\left[nDa\frac{\rho_f}{\rho_s} - \sigma(\mathcal{D} + Da)\right]\tilde{\phi} = \left[(\alpha Da\frac{\rho_f}{\rho_s} - 1)\mathcal{D} - Da\right]\tilde{C}, \tag{3.42}$$

where $\partial/\partial z$ is designated by the operator symbol $\mathcal{D}$.

Equation 3.37 can also be rewritten using $\tilde{C}, \tilde{\phi}$:

$$n\mathcal{D}\tilde{\phi} = \alpha(\mathcal{D}^2 - l^2)\tilde{C}, \tag{3.43}$$

eliminating $\tilde{\phi}$ from both of these equations, one arrives at a final equation for a single variable

$$\left[\alpha\sigma\mathcal{D}^3 + (\alpha\sigma Da - n)\mathcal{D}^2 - (l^2\alpha\sigma + nDa)\mathcal{D} + \alpha l^2 Da(n\rho_f/\rho_s - \sigma)\right]\tilde{C} = 0. \tag{3.44}$$

3.4.1 Preview of Solutions and a Simple Scaling Argument

There are two kinds of instabilities that we find in this system: One is the growth of an absolute instability, which is stationary in space and obeys a set of boundary

conditions. In this case the growth rate σ is purely real and so dissolution features will grow pinned in space and will not travel. The other kind of instability is growth in time of the amplitude of traveling waves (in this case, σ is complex), in which we assume a semi-infinite medium and investigate the behavior of traveling waves without imposing boundary or initial conditions (these can be imposed in a future investigation in order to study the effects of the finite size of the medium on the unstable wave solutions).

How do we expect the most unstable wavelength of the absolute instability to behave as we change Da, the control parameter, and should we expect a dominant wavelength to emerge at all? As a perturbation of horizontal wavelength λ_x grows, unsaturated fluid converges laterally toward growing features: when there is no diffusion only reaction is present to counteract and the deviations from equilibrium, we expect that if the time to advect laterally across a perturbation (λ_x/u) is longer than time for reaction to wipe out the concentration difference ($1/R_{\text{eff}}$), then the perturbation will not focus enough unsaturated fluid to keep itself alive and it will be damped. This means that perturbations with long horizontal wavelengths compared to L_{eq} will not grow effectively. On the other hand, focusing by the longest of the fast growing wavelengths will starve the shorter ones, and a dominant horizontal wavelength is expected to emerge. By this argument, the horizontal wavelength of the most unstable mode should increase with increasing L_{eq} (decreasing Da number).

Compaction is expected to damp horizontal wavelengths comparable to a compaction length. We propose that if L_{eq} is so large that that the most unstable wavelength is of the order of a compaction length, then stationary channels could not be maintained in the system. However, the results of our study indicate that even when stationary channels are inhibited from growth, the system still exhibits a "traveling instability": unstable growth of traveling waves.

3.4.2 Unstable Stationary Channels

In this section we investigate the growth of unstable dissolution features by investigating the growth rate of vertical modes that obey boundary conditions, termed

"absolute instability."

A solution to 3.44 of the form

$$\tilde{C}(z) = A_1 e^{m_1 z} + A_2 e^{m_2 z} + A_3 e^{m_3 z} \tag{3.45}$$

will exist, provided that

$$m^3 + (Da - \frac{n}{\alpha\sigma})m^2 - (l^2 + \frac{nDa}{\alpha\sigma})m + l^2 Da(\frac{n\rho_f}{\rho_s\sigma} - 1) = 0, \tag{3.46}$$

where $m_{1,2,3}$, the three roots of the cubic polynomial 3.46, are either all real or one real and two complex conjugates. Equation 3.46 establishes the relationship between wavenumbers in the vertical (m_1, m_2, m_3) and horizontal (l) directions and their growth rate. In order to find the solution of the linear stability problem (that is, to find the growth rate σ as a function of the Damkholer number and the rigidity α for any given horizontal wavenumber l) we need to specify a set of three boundary conditions, which actually correspond to the third-order differential equation 3.44. These boundary conditions will constrain the vertical modes m_1, m_2 and m_3, and as a consequence determine $\sigma(l, Da, \alpha)$ via 3.46.

Boundary conditions for equation 3.44 emerge from the following assumptions: (1) There is no dissolution and porosity is constant at $z = 0$, where the incoming fluid is in equilibrium with the matrix. This assumption leads, via 3.36, to a rigid boundary condition ($\mathcal{C} = 0$) at $z = 0$. (2) The $z = 0$ boundary is impermeable to the perturbation, meaning that the flux of fluid normal to the boundary remains unperturbed from its steady state value. (3) Using an observation from physical and computer experiments [36] that lateral fluxes ahead of the perturbation are negligible, we require (from 3.40) a rigid boundary at $z = L$ as well. (Alternatively, one could choose a "free-flux" boundary at $z = L$, which actually acts to amplify the perturbation by relaxing the restrictive top rigid-boundary condition, and also complicates the mathematical presentation somewhat.) The above conditions are equivalent to

$$\tilde{C}(z = 0) = 0, \quad \tilde{C}(z = 1) = 0, \quad \frac{\partial \tilde{C}}{\partial z}(z = 0) = 0, \tag{3.47}$$

and we seek the conditions under which a nontrivial solution of the form 3.45 exists.

The boundary conditions 3.47 tell us that

$$\begin{pmatrix} 1 & 1 & 1 \\ e^{m_1} & e^{m_2} & e^{m_3} \\ m_1 & m_2 & m_3 \end{pmatrix} \begin{pmatrix} A_1 \\ A_2 \\ A_3 \end{pmatrix} = \begin{pmatrix} 0 \\ 0 \\ 0 \end{pmatrix}. \tag{3.48}$$

This has a nontrivial solution if the determinant is equal to zero:

$$e^{m_1}(m_2 - m_3) + e^{m_2}(m_3 - m_1) + e^{m_3}(m_1 - m_2) = 0. \tag{3.49}$$

To find the growth rate as a function of horizontal wavenumber from 3.46 and 3.49, we first analytically calculate the three roots $m_{1,2,3}(\sigma, l, Da, \alpha)$ of the cubic polynomial 3.46. Substituting these roots into 3.49, we then obtain an implicit equation for $\sigma(l, Da, \alpha)$. Choosing a value for the parameters Da and α, we finally obtain $\sigma(l)$ by seeking the roots of the implicit equation 3.49, using a bisection numerical method. Numerical solutions indicate that m_1, m_2, m_3 have the form of 1 real root and 2 complex conjugates so that $\tilde{C}(z)$ of 3.45 can be written as

$$\tilde{C}(z) = B_1 e^{m_1 z} + B_2 e^{pz} \cos qz + B_3 e^{pz} \sin qz. \tag{3.50}$$

Before presenting the results of the linear stability analysis, we would like to briefly discuss the physics of the problem revealed by writing 3.46 as a dispersion relation in which $\sigma = \sigma(m, l)$:

$$\sigma = \frac{1}{\alpha} \frac{nm}{m^2 - l^2} - \frac{nl^2 Da \frac{\rho_f}{\rho_s}}{(m^2 - l^2)(m + Da)}. \tag{3.51}$$

The growth rate σ is composed of two completely separate parts, one that includes a dependence on the rigidity of the matrix, α, but does not depend on the chemical reaction, and the second that depends only on the rate of chemical reactions, the Da number, but does not depend on the rigidity; σ can be expressed as a sum of these parts

$$\sigma = \sigma_C + \sigma_{Da}, \tag{3.52}$$

where the compaction contribution to the growth rate is

$$\sigma_C = \frac{1}{\alpha} \frac{nm}{(m^2 - l^2)} \tag{3.53}$$

and the chemical reaction contribution to the growth rate is

$$\sigma_{Da} = -\frac{nl^2 Da \frac{\rho_f}{\rho_s}}{(m^2 - l^2)(m + Da)}. \tag{3.54}$$

As the matrix rigidity is increased ($\alpha \to \infty$), then $\sigma \to \sigma_{Da}$. This limit strips away compaction effects on the instability. In the limit of $Da \to 0$, $\sigma \to \sigma_c$ and only compaction effects are left.

Rigid medium limit. As mentioned previously, in the limit of a rigid medium ($1/\alpha \to 0$), compaction effects are not present, illuminating the physics of the dissolution instability. In Figure 3-3 we present the growth rate σ as a function of the horizontal wavenumber l for $Da = 10$ in a rigid medium ($1/\alpha = 0$). For comparison, the growth rate in a compacting medium with $\alpha = 1$ is also shown. The choice of $Da = 10$ is given as an example, to demonstrate the qualitative behavior of the solution. For a rigid medium any value of Da produces the same kind of behavior with positive growth rate peaking at a certain wavelength. Results for a compacting medium will be discussed in the next section.

It should be noted that actually σ attains several values for each value of l: these correspond to different growth rates of different vertical modes with a wavelength $\lambda_z = 2\pi/q$ where q is defined in 3.50. The first mode has approximately half a wavelength (q close to π) in the vertical dimension of the box and is the fastest growing mode. The second mode has close to one wavelength fitted in the vertical dimension and grows more slowly. The third mode grows even more slowly, etc. Hence only the first mode, the fastest growing one, is plotted on Figure 3-3. The growth rate in Figure 3-3 is seen to peak for horizontal wavenumber $l_{\max}$, and so $\lambda_x = 2\pi/l_{\max}$ is the most unstable wavelength in the system.

Calculations similar to Figure 3-3 have been made for different Da numbers. Figure 3-4a shows the most unstable wavelengths, λ_x, as a function of Da, for the rigid medium case. As Da increases, λ_x is shown to decrease and to approach a power law dependence on Da. For $Da \gg 1$, and spanning 4 orders of magnitude, the nondimensional dominant horizontal wavelength scales as $\lambda'_x \sim \sqrt{1/Da}$. In dimensional units

this means that

$$\lambda_x \sim \sqrt{L * L_{\mathrm{eq}}}. \tag{3.55}$$

The increase in dominant horizontal wavelengths of channels with increasing equilibration length (decreasing Da) is as predicted by the "preview of solutions." The fact that the lateral extent of channels depends also on the vertical dimension of the box is more surprising. We postulate that the vertical length scale L is imposed on the perturbations by the fact that channels always span the box vertically. Since the vertical mode is coupled to the horizontal modes in 3.46, the horizontal modes are forced to feel the system size too. The aspect ratio (λ_x/λ_z) of the channels decreases as Da is increased. Since in dimensional parameters (when $Da \gg 1$) $\lambda_z \sim L$ and $\lambda_x \sim \sqrt{L * L_{\mathrm{eq}}}$, then the aspect ratio is

$$\lambda_x/\lambda_z \sim \sqrt{L_{\mathrm{eq}}/L} = \sqrt{1/Da}, \tag{3.56}$$

as seen in Figure 3-4b, and the channels become more finger-like as the equilibration length decreases or as the system size increases.

The growth rate σ of the fastest growing horizontal wavenumber l_{max} as a function of Da is plotted in Figure 3-4c, where one can see that as $Da \to \infty$, the growth rate approaches a constant value, $\sigma \to n\rho_f/\rho_s$, which can be predicted from 3.54. This limit is determined by $\partial k/\partial\phi \propto n$, the derivative of the permeability with respect to porosity. If the permeability decreased with increasing porosity, then the instability would not occur and the growth rate would approach a negative constant value. In other words, the maximum change in porosity is only related to the rate at which flux changes with porosity.

The increase of σ with Da seems counterintuitive at first, since as Da is increased the system is closer to equilibrium (equation 3.31 and Figure 3-2). The explanation stems from the fact that as $Da \to \infty$, any perturbation in flux is immediately compensated by chemical reaction bringing the liquid close to local chemical equilibrium. In the meantime, the porosity has been lowered further by the strong dissolution, so additional fluid flows into the perturbed region. This in turn will result in immediate strong dissolution lowering the porosity even further. On the other hand, a low Da

number will tend to weaken the growth of channels because the fluid has time to redistribute the concentration by lateral advection and thus smooth away gradients before substantial dissolution occurs.

Compacting medium. Numerical solutions for a compacting medium with α of order 1 indicate that there exists a critical value for Da. For

$$Da > Da_{\text{crit}} = 1/\alpha, \tag{3.57}$$

dissolution channels will grow. Once condition 3.57 is violated, there are no solutions which obey the boundary conditions 3.47 and dissolution channels do not form.

Condition 3.57 can be rewritten using the definitions of Da, α and L (equations 3.19, 3.22, and 3.14):

$$Da\ \alpha = c_h \frac{h}{L_{\text{eq}}} > 1. \tag{3.58}$$

In other words, this term is proportional to the ratio of the compaction length to the reaction length. If the compaction length is much larger than the reaction length, permanent channels can grow. Otherwise, compaction will become important and will act as a stabilizing mechanism, trying to squeeze the channels shut and forcing propagation of the instability as waves, as can be seen in the "unstable dissolution waves" section.

Figure 3-3 shows the growth rate for $Da = 10, \alpha = 1$, so that $Da\ \alpha = 10$, not so high above the critical value and in the lower range of values of $Da \times \alpha$ predicted for the mantle, as can be seen in Table 3.1. Growth rates in a compacting medium are shown in comparison with results for $Da = 10$ and a rigid medium, $1/\alpha = 0$. Figure 3-3 shows that the maximum wavelength in the compacting medium is not changed from a completely rigid medium and the growth rate is only slightly lower than in the rigid case. Compaction is shown to damp the long wavelengths, as expected.

Eigenfunctions. Here we calculate the eigenfunctions (full z dependent solutions) of all perturbed fields in the problem $(\hat{C}, \hat{\phi}, \hat{u}, \hat{v}, \hat{c})$ and plot them as contour plots, taking a snapshot in time. This demonstrates our claim that the instability is characterized by channel-like features and helps one to visualize the spatial distribution of melt and porosity.

We use 3.50, the three independent boundary conditions 3.47, and 3.36-3.41 to analytically find the eigenfunctions and thus the full solutions for the perturbation variables:

$$\hat{C}(x,z,t) = B_1\left[\frac{m_1-p}{q}e^{pz}\sin qz + e^{pz}\cos qz - e^{m_1 z}\right]e^{ilx+\sigma t} \tag{3.59}$$

$$\begin{aligned}\hat{\phi}(x,z,t) = B_1\frac{\alpha}{n}\Bigg[&\left(\frac{q(q^2+2p^2+l^2-m_1p)}{p^2+q^2} - \frac{p(m_1-p)(p^2-l^2)}{q(p^2+q^2)}\right)e^{pz}\sin qz \\ &+\frac{2pl^2-m_1(p^2+q^2+l^2)}{p^2+q^2}e^{pz}\cos qz \\ &+\frac{m_1^2-l^2}{m_1}e^{m_1 z} + l^2\left(\frac{m_1-2p}{p^2+q^2}+\frac{1}{m_1}\right)\Bigg]e^{ilx+\sigma t}\end{aligned} \tag{3.60}$$

$$\hat{u}(x,z,t) = -iB_1\alpha l\hat{C} \tag{3.61}$$

$$\begin{aligned}\hat{w}(x,z,t) = &(n-1)\hat{\phi} + B_1\frac{\alpha}{q}\left[((m_1-p)p-q^2)e^{pz}\sin qz\right. \\ &\left.+ m_1 q(e^{pz}\cos qz - e^{m_1 z})\right]e^{ilx+\sigma t}\end{aligned} \tag{3.62}$$

$$\hat{c}(x,z,t) = \frac{\rho_s}{\rho_f Da}\left[\hat{C} - \hat{\phi}\left(\frac{1}{\alpha}\frac{nm_1}{m_1^2-l^2} - \frac{n\rho_f l^2 Da}{\rho_s(m_1^2-l^2)(m_1+Da)}\right)\right] \tag{3.63}$$

In order to plot the behavior of the perturbation variables as a function of x and z, we use the values of m_1, p, q, and σ calculated numerically for the most unstable wavelength, as described in the previous section. In the surface plots illustrated in Figure 3-5 we used parameter values of $Da = 100, \alpha = 1$.

Figure 3-5a is a plot of the perturbation in compaction $\hat{C}(x,z,t_0)$, which is equivalent to the perturbation pressure. Narrow channels spanning the vertical dimension of the box can be seen. The constant pressure boundary conditions force the pressure field to achieve a maximum at about three quarters of the way to the top of the box and not at the top boundary. Porosity $\hat{\phi}(x,z,t_0)$ is plotted in Figure 3-5b and can be seen to have increasing amplitude with increasing height and to achieve a maximum amplitude at the top of the box. Disequilibrium undersaturation, $-\hat{c}(x,z,t_0)$, and vertical velocity have surface plots very similar in shape to the plot of porosity.

Within linear approximations, when the system is unstable, the longer the melt ascends, the more robust the instability becomes, spanning any given box size. This is understandable, since the more disequilibrated the ascending fluid, the stronger the driving force for instability.

3.4.3 Unstable Dissolution Waves

In this section we present a different solution to the set of perturbation equations 3.36-3.40, which is independent of the channel solution and may coexist with it. We study simple linear propagating waves in an infinite medium. These are related to compaction waves but present a previously unstudied facet of the RII instability, unstable traveling dissolution waves.

When mass transfer between the solid and the liquid is zero ($Da = 0$), equations 3.36-3.40 are close to the ones arrived by [76] in his linear analysis of compaction driven waves, apart from another time derivative which survived in his divergence equation because of the different time scales and therefore different linearization involved. In the limit of $Da \to 0$ we arrive at an equation for traveling waves:

$$n\frac{\partial \phi}{\partial z} - \nabla^2 \frac{\partial \phi}{\partial t} = 0. \tag{3.64}$$

Assuming wave solutions of the form

$$\phi = Ae^{i(lx+mz-\sigma t)}, \tag{3.65}$$

the dispersion relation is

$$\sigma = \frac{nm}{m^2 + l^2}, \tag{3.66}$$

indicating the existence of traveling waves, with a phase velocity c_p

$$c_p = \frac{\sigma}{K} = \frac{n\cos\theta}{K^2}, \tag{3.67}$$

where the wave vector is defined by $K^2 = l^2 + m^2$ and θ is the angle between the wave vector and the vertical, as seen in Figure 3-6a. The phase velocity in the z direction, $c_{pz} = c_p/\cos\theta$, is greater than zero, thus linear compaction waves always travel with an upward component. (It is interesting to note that 3.64 is identical to the equation for planetary Rossby waves that dominate the ocean and atmosphere. Rossby waves have westward traveling phases.)

These results from the zero Da limit are close to the results from [76], in which traveling dispersive waves arise from compaction. The waves form due to the increase

of melt flux as a function of porosity, and its ability to deform the matrix. Viscous resistance to volume change causes waves to disperse.

We now turn to study the full problem of nonzero Da and seek wave-like solutions to the set of perturbation equations 3.36-3.40,

$$\hat{C}(z,x,t) \sim e^{i(mz+lx)+\sigma t},$$

where m and l are real and σ is to be determined from the dispersion relation. A single equation similar to 3.46 is found, which in turn can be written as a dispersion relation that restricts the growth rate to be

$$\sigma = \frac{nl^2 Da^2 \frac{\rho_f}{\rho_s}}{(m^2+l^2)(m^2+Da^2)} - in\frac{m}{m^2+l^2}\left[\frac{1}{\alpha} + \frac{\rho_f l^2 Da}{\rho_s(m^2+Da^2)}\right]. \tag{3.68}$$

This growth rate has an imaginary part, $\sigma_{\mathcal{I}}$, and a real positive part, $\sigma_{\mathcal{R}}$, indicating that if porosity waves were formed in the presence of dissolution, their amplitude would increase with time to form "unstable traveling dissolution waves", or "channelleons".

The phase velocity of the waves, c_p, is

$$c_p = -\frac{\sigma_{\mathcal{I}}}{K} = n\cos\theta\left(\frac{1}{\alpha K^2} + \frac{\sin^2\theta Da\frac{\rho_f}{\rho_s}}{K^2\cos^2\theta + Da^2}\right). \tag{3.69}$$

where the wave vector is defined by $K^2 = l^2 + m^2$ and θ is the angle between the wave vector and the vertical. In the presence of dissolution, the amplitude of the waves grows in time due to the positive real part of the growth rate,

$$\sigma_{\mathcal{R}} = \frac{n\sin^2\theta Da^2\frac{\rho_f}{\rho_s}}{K^2\cos^2\theta + Da^2}. \tag{3.70}$$

Here $\sigma_{\mathcal{R}}$ is seen to be always positive, providing a mechanism for nucleation and growth of "magmons", which previously required an initial step perturbation in porosity in order to nucleate. For $Da = 0$, $\sigma_{\mathcal{R}} = 0$, indicating that compaction waves in the absence of dissolution are marginally stable and travel with a constant amplitude.

The presence of dissolution ($Da > 0$) brings about interesting behavior of both the phase velocity of the waves and the rate at which their amplitude grows. Figure 3-6b illustrates c_p and $\sigma_{\mathcal{R}}$ as calculated from 3.69 and 3.70. The top panel shows c_p

and $\sigma_{\mathcal{R}}$ as a function of orientation of the wave front θ for constant K, Da, and α. The phase velocity of planar waves is maximal when they have a diagonal orientation but drops to zero for waves that are oriented vertically ($\theta \rightarrow \pi/2$). On the other hand, these vertical "stationary channels" are the ones that grow the fastest, as is seen from $\sigma(\theta)$, and are actually the collapse of the traveling wave solution to the stationary channel solution obtained in the previous section. The bottom panel of Figure 3-6B shows c_p and $\sigma_{\mathcal{R}}$ as a function of Da for constant K, θ, and α. The maximum in phase velocity corresponds to $K \cos\theta = Da$, while maximal growth rate occurs for $Da \rightarrow \infty$, similar to the maximal growth rate for the stationary channels. Compaction-dissolution waves are dispersive, as expected for waves which arise partly from compaction [76], and the long wavelengths both travel and grow the fastest. Like the linear compaction waves of 3.64, these waves always have an upward phase velocity. Waves propagate with a finite phase velocity even in the absence of compaction. They appear to travel diagonally because vertical wavelengths that are shorter than the system size ($m > 0$ or $\theta < \pi/2$) imply that at some point in space, upwelling fluids in high-porosity regions encounter an obstacle of low porosity, forcing the fluid to chew its way up with a diagonal component of velocity.

3.5 Finite Diffusion

Diffusion in a porous medium is a result of hydrodynamic dispersion and molecular diffusion. Dispersion, in most cases, is associated with larger diffusion coefficients than molecular diffusion. Both have the effect of of causing an initial sharp concentration gradient to spread out with time. This section addresses the question of whether a finite diffusion rate will smooth out gradients in the concentration field to a point where the channeling instability will not be able to grow.

3.5.1 Predictions

It is probable that perturbations smaller than a diffusion length will be smoothed out. When diffusion is weak, and a diffusion length is smaller than the most unstable

wavelength determined by reaction (as calculated for the no diffusion case above), diffusion will only act as a short-wave cutoff. When diffusion is strong, and a diffusion length is longer than the most unstable wavelength determined by reaction alone, it will allow for unstable growth but modify the dominant horizontal wavelength, forcing it to become longer than a diffusion length. This is because, as seen in Figure 3-3, all wavelengths are unstable in the presence of reaction alone (in the rigid case) and when short waves are damped, long wavelengths can become the fastest growing in the system. It follows that for strong diffusion, the growth rate will be lowered compared to the case with no diffusion.

3.5.2 Simplified Calculations

We present here a somewhat simplified linear analysis for the finite diffusion case. We allow for diffusion only in the horizontal direction, since allowing for vertical diffusion adds higher order derivatives in the vertical direction, complicating the vertical structure of the equations beyond the point necessary to obtain well-behaved solutions to the stability problem. This approximation is probably justified, since the vertical melt velocity is believed to be much larger than diffusion rates. However, one should note that available experimental diffusivities in silicate melts, quoted in Table 3.1, do not include effects of dispersion.

Solving the perturbation equations 3.36-3.40 with a finite value for $1/Pe$, 3.46 will have the form

$$m^3 + (Da + l^2/Pe - \frac{n}{\alpha\sigma})m^2 - (l^2 + \frac{nDa}{\alpha\sigma})m + l^2 Da\frac{n\rho_f}{\rho_s\sigma} - l^2(Da + l^2/Pe) = 0. \quad (3.71)$$

The growth rate is again decomposed into compaction and reaction parts

$$\sigma = \sigma_C + \sigma_{Da} \quad (3.72)$$

where the compaction contribution to the growth rate is

$$\sigma_C = \frac{1}{\alpha}\frac{nm}{(m^2 - l^2)} \quad (3.73)$$

and now

$$\sigma_{Da} = -\frac{nl^2 Da\frac{\rho_f}{\rho_s}}{(m^2 - l^2)(m + Da + l^2/Pe)} \quad (3.74)$$

is the diffusion-reaction contribution to the growth rate. In the limit of $l \to \infty$, $\sigma_{Da} \to 0$, as expected since diffusion will tend to damp the growth of short wavelength perturbations.

We use boundary conditions 3.47 to solve 3.71 following the same numerical procedure outlined in the "unstable stationary channels" section. Figure 3-7 demonstrates the effect of adding diffusion to the no-diffusion solution obtained for the rigid medium. Generally, diffusion acts to reduce the growth rate of the instability and to shift the most unstable wavelength to become longer than in the no diffusion case, as predicted.

Figure 3-8 shows the most unstable wavelength and its growth rate for a constant $Da = 10$ and a varying Pe number. The qualitative behavior is as predicted: for weak diffusion ($Pe \gg Da$, which corresponds to the condition when equation 3.17 can be considered diffusionless) the most unstable wavelength and its growth rate remain nearly the same as the case with no diffusion. For $Pe \ll Da$ the dominant wavelength λ_x increases with increasing diffusion length (decreasing Pe) $\lambda_x \propto (1/Pe)^{1/4}$, and the growth rate is reduced but remains positive.

Thus we conclude that when diffusion is strong or when the Pe number is of the same order of magnitude as the Da number, the addition of diffusion can alter channel spacing and lower the growth rate but cannot inhibit the instability from growing. When diffusion is weak ($Pe \gg Da$), it can be neglected altogether.

3.6 Discussion

The results of this work show the potential for an existence of a channeling instability in Earth's upper mantle. The instability stems from combined chemical and hydrodynamical effects. Melt decompresses as it ascends through the mantle, increasing its ability to dissolve the surrounding matrix. A small perturbation in porosity allows a larger volume of unsaturated fluid to flow, thus increasing dissolution and further increasing porosity in a positive feedback mechanism.

We consider a model system incorporating porous flow, dissolution, and matrix

compaction effects and find a steady state formed by the competition between dissolution and compaction. Linear stability analysis is then performed, predicting that long, narrow channels may spontaneously form. The emerging horizontal wavelength λ_x is shown to depend on the chemical equilibration length $L_{\rm eq}$ and the vertical extent of the system L. For chemical equilibration lengths that are smaller than the size of the system ($Da > 1$), $\lambda_x = 2.534\sqrt{L_{\rm eq}L}$. For a system of the size of the melting region, $L \approx 75$ km, channels will range from 10 cm wide, when $L_{\rm eq} \sim 10^{-7}$ m, to nearly a kilometer wide if $L_{\rm eq} \sim 10$ m. Our linear prediction of channel width is in agreement with (1) postulated vein sizes needed to successfully segregate the melt in order to see observed chemical signatures [79], and (2) the size of dunite dissolution features found in field observations [10, 19, 62, 55, 34]. This further strengthens our belief that the channeling instability plays a crucial role in focusing of melt and determining the geochemical composition of upwelling liquids and residual mantle peridotites. Channels formed by the reactive infiltration instability may provide the means for extracting melt out of the viscously deformable upper mantle.

If the chemical equilibration length is too long, comparable to the compaction length, formation of the instability is inhibited by compaction. A coexisting solution predicts unstable growth of elongated traveling porosity and concentration waves that exist under all conditions. The exact criterion for stationary channels to grow is $c_h h/L_{\rm eq} > 1$. We test whether this condition is met in Earth's mantle, using a range of numbers explained in Appendix B and tabulated in Table 3.1. Equilibration lengths range from <1 mm to 10 m, and we use $\beta = 2 \times 10^{-6}$ m^{-1}; $c_h h/L_{\rm eq}$ ranges from $O(1)$ to $O(10^6)$ when the compaction length is taken as 1000 m and from $O(10^{-2})$ to $O(10^4)$ when a compaction length is taken as 100 m. Parameter values that are believed to be characteristic of Earth's mantle are thus mostly in the regime that allows for rapid growth of stationary channels.

The effect of diffusion is also investigated. When diffusion is strong enough, it will cause an increase in channel spacing and a decrease in channel growth rate. However, this will not inhibit the channels from growing.

The forming channels are elongated and span the vertical box size. Their ampli-

tude increases with height, thus showing increasing chemical disequilibration as liquid ascends in the melting column. When Da is high, chemical disequilibration is small, but dissolution of channel is most efficient. Hence soluble phases may become reduced in volume or completely exhausted. When channels thus become stripped of soluble phases (i.e., stripped of pyroxene but not of olivine), melt flowing through them will be effectively isolated from equilibration with these phases. Since the channels span the system vertically, they can bring to the surface melt that has not equilibrated with its surroundings since it began its ascent at the bottom of the melting column. This may explain why MORB is out of chemical equilibrium with upper mantle peridotites [28] and includes chemical signatures from the bottom of the melting column [37, 68].

Channels formed as a result of this instability should be identifiable in the geologic record. Their contact relationships should be indicative of replacement of host peridotite as a result of selective dissolution of more soluble phases (i.e., pyroxene). Additionally, minerals in dissolution channels should be close to equilibrium with MORB and therefore will have very different minor and trace element compositions from the same minerals in surrounding peridotite. In fact, these characteristics are observed in dunite bodies within the residual mantle peridotite section of the Oman ophiolite [32].

However, we emphasize that the results of the present study may not be directly applicable to the mantle. In particular, the morphology of dissolution channels arising from this instability, developing over finite length scales and timescales, cannot be predicted from linear stability analysis. It is possible that a much richer behavior emerges due to non-linear effects. For example, space or time dependent behavior, as tentatively sketched in Figure 3-9. Additionally, the multicomponent melt migration process in the earth with the inclusion of advective heat transport and background melting effects is more complicated than the problem studied here and is a topic for ongoing studies.

In addition to the formation of stationary dissolution channels, another coexisting linear solution indicates the existence of traveling compaction-dissolution waves,

whose amplitude increases with time. These unstable waves, pockets of undersaturated melt in a high porosity region, will transport increasingly undersaturated melts to the surface even when the matrix is too weak to support stationary channels. They may also aid in explaining the production and growth of "magmons," compaction waves previously thought to be generated by an initial step in porosity.

Variable	Symbol	Value	Notes
Solubility gradient	β	$2 \times 10^{-6}\mathrm{m}^{-1}$	1
Linear dissolution rate		$10^{-12} - 10^{-8}$ m s^{-1}	2
Solid density	ρ_s	3×10^3 kg m^{-3}	
Reaction rate constant	R	$10^{-9} - 10^{-5}$ kg m^{-2} s^{-1}	
Grain edge length	d	$10^{-4} - 10^{-3}$ m	
Total surface area		$10^3 - 10^5\ m^2/m^3$	3
Porosity	ϕ	$10^{-3} - 10^{-2}$	4
Solid/liquid surface area	S	$(1-3) \times 10^{-1}$	5
Volume fraction of soluble phase		$10^{-2} - 10^{-1}$	6
Permeability exponent	n	$2-3$	7
Melt fraction	F	$0.05 - 0.2$	8
Solid upwelling rate	V_0	$10^{-10} - 10^{-9}$ m s^{-1}	9
Background fluid velocity	w_0	$10^{-9} - 10^{-6}$ m s^{-1}	9
Equilibration length	L_{eq}	$10^{-7} - 10$ m	9
Damköhler number (L=100m)	Da	$10^9 - 1$	10
Diffusion coefficient	D	$10^{-12} - 10^{-10}$ m^2 s^{-1}	11
Peclet number (L=100m)	Pe	$10^8 - 10^3$	12
compaction length	h	$100 - 1000\ m$	13

Table 3.1: Characteristic Values Believed to Be Applicable to Earth's Mantle. For a detailed discussion, see Appendix B. Notes: 1.[36, 35]. 2. higher dissolution rates are from [12] and [41], and low dissolution rate is from [96]. 3. using d, cubic grains, and [90]. 4.[27, 75]. 5. in fraction of total surface area. 6. i.e., fraction of pyroxene [34]. 7. [90]. 8. fraction of solid mass that has melted. 9. see Appendix B. 10. using range of L_{eq} given above. 11.[25]. 12. using w_0, D given above. 13. [44].

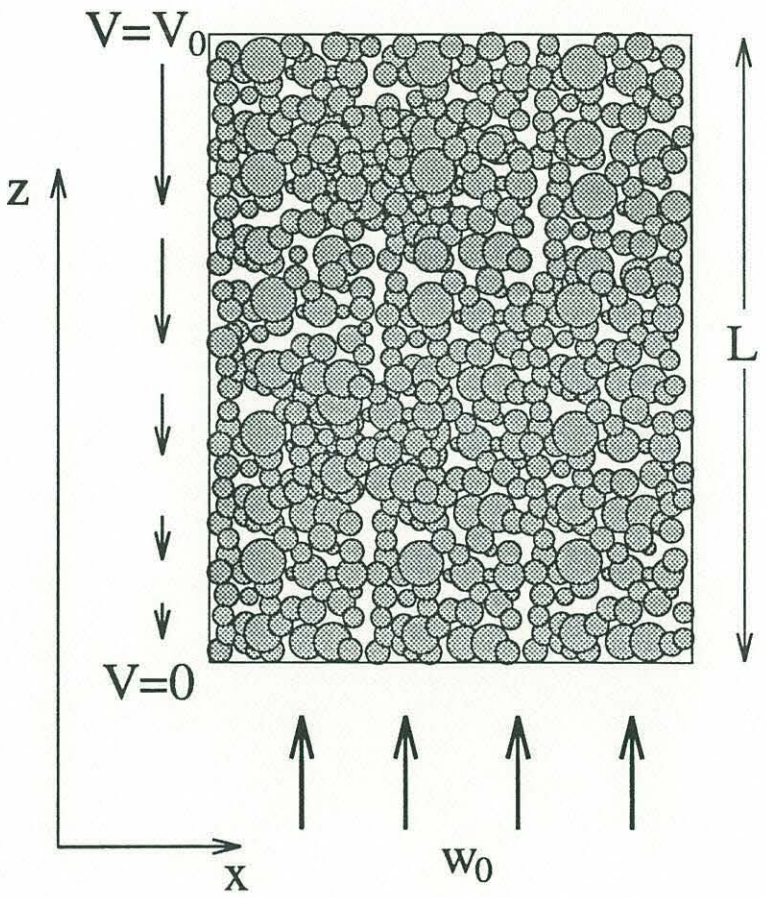

Figure 3-1: Setup of the problem: Fluid is driven upward by a pressure gradient, entering the soluble porous media at $z = 0$ and leaving at $z = L$. Owing to decompression, the fluid has increasing ability to dissolve the solid matrix. The matrix is allowed to contract by compaction and thus counteract to some degree the effects of increasing dissolution.

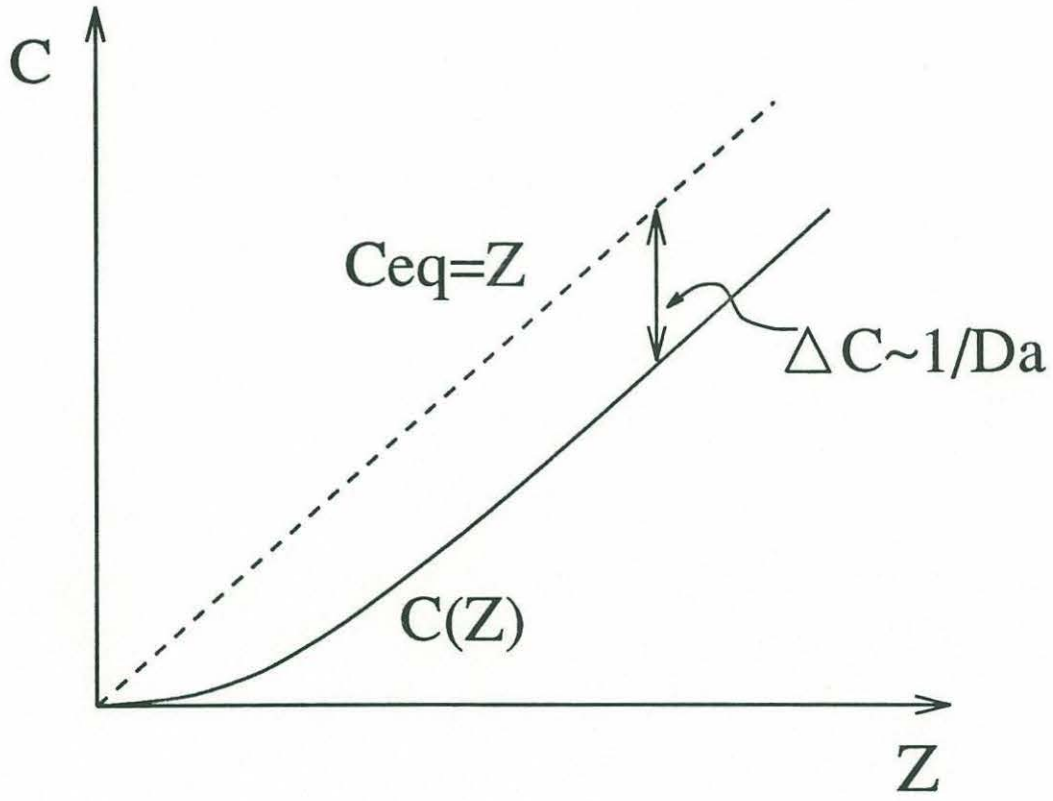

Figure 3-2: Nondimensional steady state concentration as a function of height, drawn as a solid line. After a narrow boundary layer (≈ 1 reaction length), the deviation of the steady state concentration from the equilibrium value (represented by a dashed line), approaches a constant value $\Delta c \sim 1/Da$.

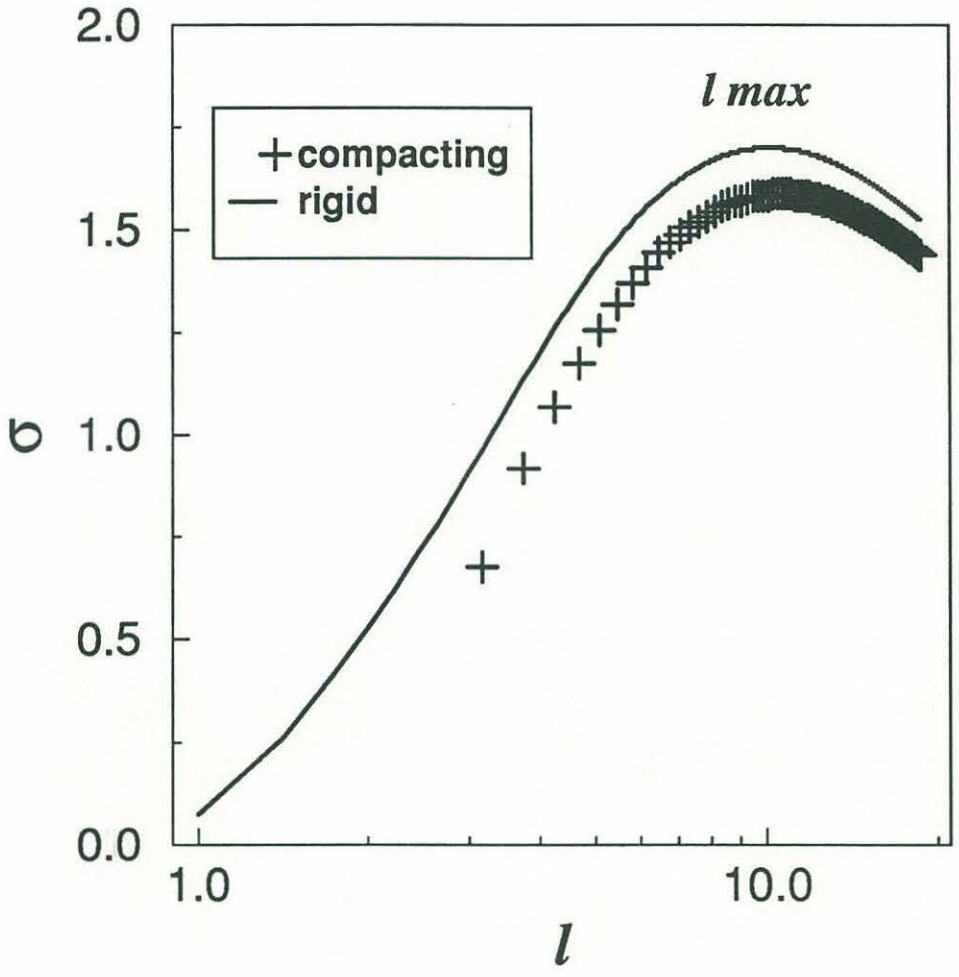

Figure 3-3: Nondimensional growth rate σ versus nondimensional horizontal wavenumber l, for $Da = 10$ in a rigid medium ($1/\alpha = 0$), and in a compacting medium with $\alpha = 1$; $l_{\max}$ indicates the fastest growing wavenumber. Comparing the growth of unstable channels in a compacting and a rigid medium, one notes that the most unstable wavelength is hardly altered and its growth rate is only slightly lowered due to the stabilizing effect of compaction. Compaction does, however, damp the long-wavelength perturbations. This effect leads to a critical Da for existence of the instability in a compacting medium.

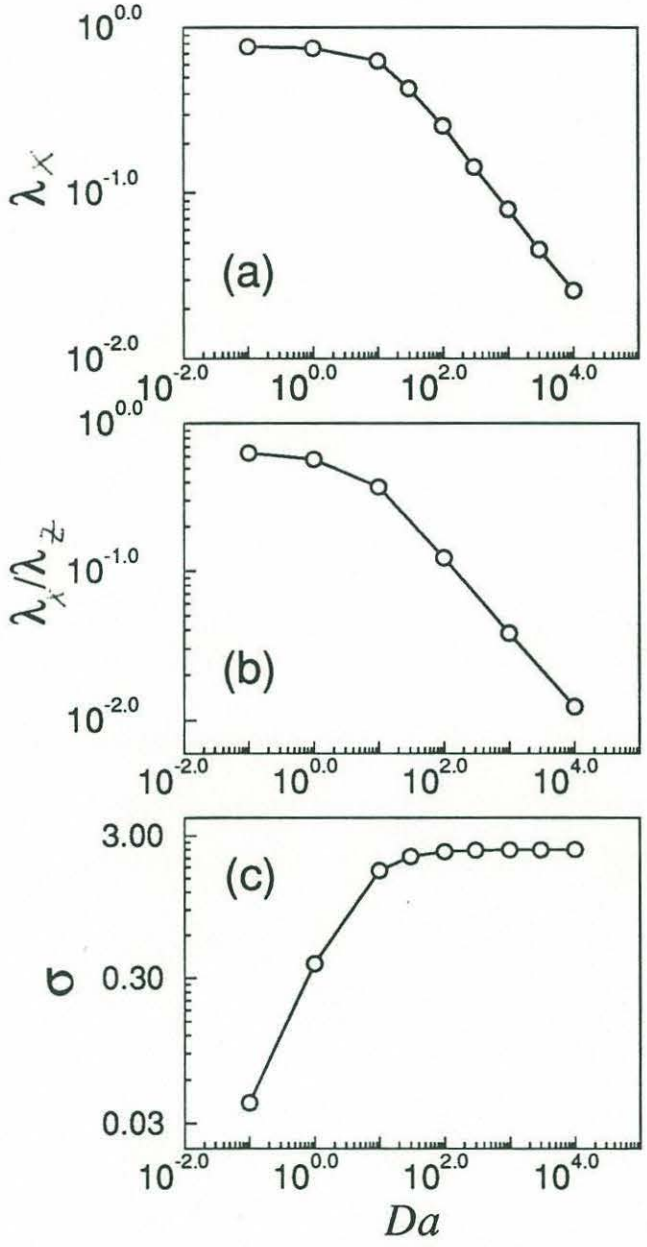

Figure 3-4: (a) The fastest growing horizontal wavelength, $\lambda_x = 2\pi/l_{\max}$, derived from plots similar to Figure 3-3 with different Da numbers in a rigid medium. For $Da > 1$, and spanning 4 orders of magnitude, $\lambda_x^2 \propto 1/Da$. (b) Aspect ratio of channels, $q/l = \lambda_x/\lambda_z$, as a function of Da in a rigid medium. Perturbations become more finger like as Da number is increased. (c) Growth rate of $l_{\max}$ as a function of Da in a rigid medium. The system becomes increasingly unstable with increase in Da and reaches a constant limit for $Da \to \infty$. This limit is set by the derivative of permeability with respect to porosity.

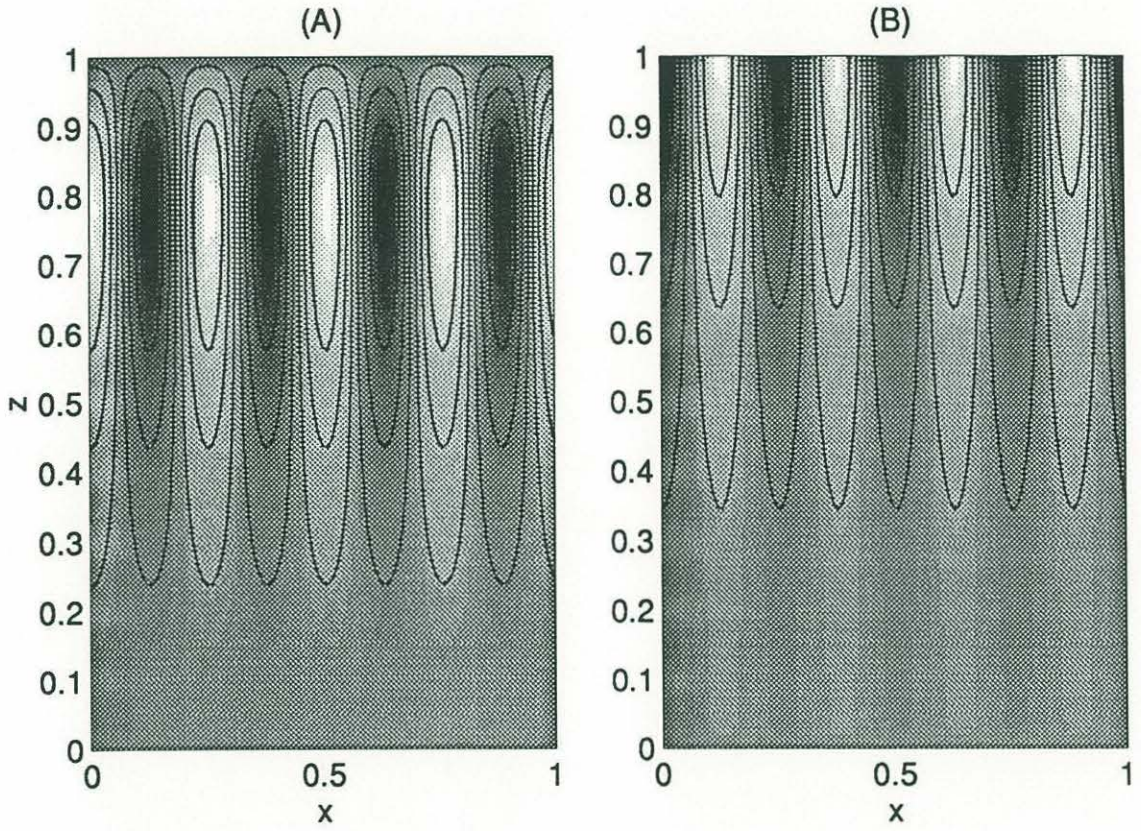

Figure 3-5: Eigenfunctions for a compacting medium, $Da = 10, \alpha = 1$ (a) Perturbation pressure as a function of x and z. Dark shading indicates negative values; light shadings indicate positive values. Owing to the boundary conditions, pressure perturbations are forced to zero at the top of the box, thus attaining a maximum amplitude at $z \approx 3/4$. (b) Porosity, vertical velocity, and concentration, which look very similar, are plotted as a function of x and z. These variables have increasing amplitude as a function of z and attain a maximum at $z = 1$.

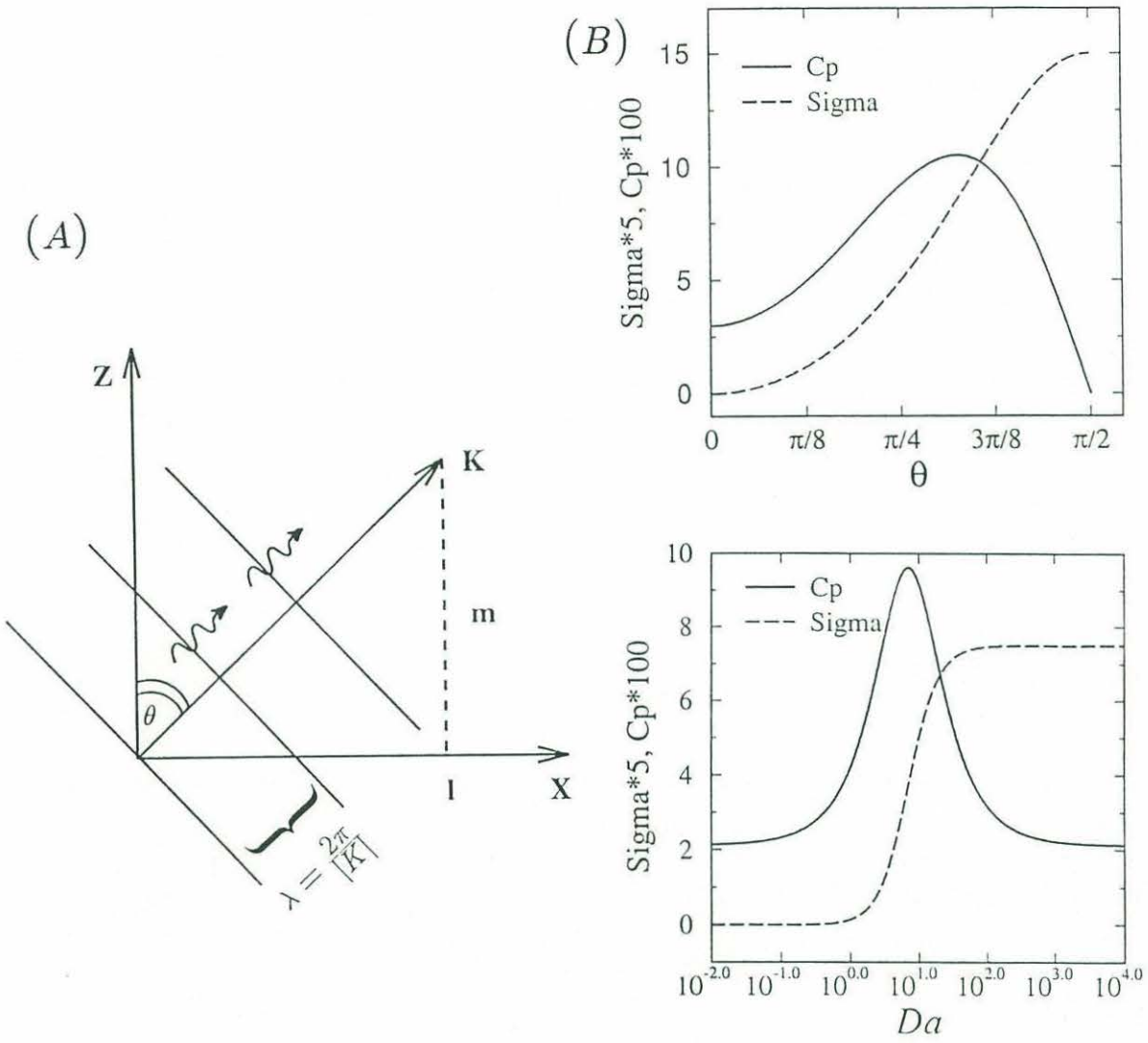

Figure 3-6: (a) Schematic drawing of a planar wave, with wave vector $K^2 = l^2 + m^2$, oriented at angle θ to the vertical. The phase velocity is the velocity at which the phases propagate. (b) (top) Growth rate $\sigma_{\mathcal{R}}$ and phase velocity c_p of compaction-dissolution waves as a function of the planar wave orientation θ. Calculations were made using $K = 10$, $Da = 10$, and $\alpha = 1$. Phase velocity is maximum when the wave is at some angle to the vertical and is zero for vertical stripes. Although these stripes do not propagate, they grow the most rapidly, as seen from $\sigma(\theta)$. The stationary vertical stripes are the collapse of the plane wave solution to the unstable channels solution. (bottom) The $\sigma_{\mathcal{R}}$ and c_p as a function of Da. Calculations were made using $K = 10$, $\theta = \pi/4$ and $\alpha = 1$. The maximum in phase velocity is for waves with $K \cos\theta = Da$. At this point a rapid transition from nearly zero growth rate to maximum growth rate can be observed.

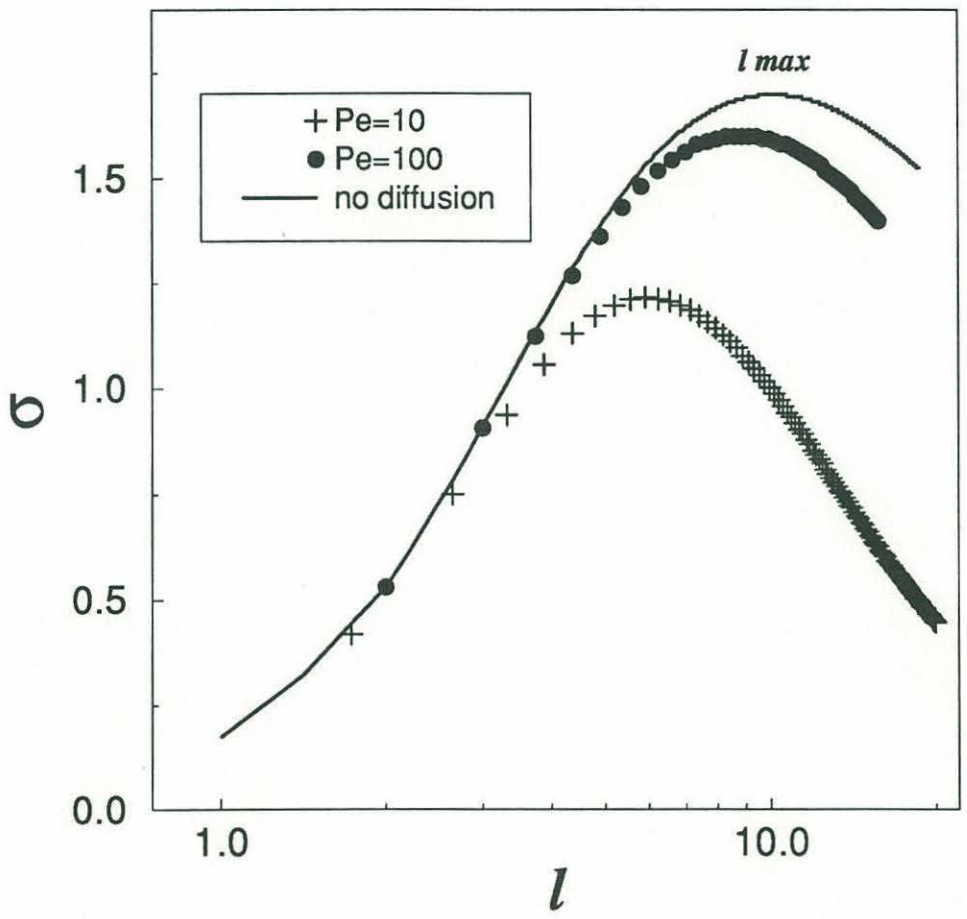

Figure 3-7: Growth rate σ as function of horizontal wavenumber l for a rigid matrix with $Da = 10$ for various diffusion coefficients. Solid line is the growth rate in the case of no diffusion, replotted from Figure 3-3. Solid circles are the linear stability analysis results for a rigid system with weak diffusion, $Pe = 100$. Strong diffusion with $Pe = 10$ is shown in crosses. The horizontal wavelength ($= 2\pi/l_{\max}$) of forming channels becomes larger in the presence of diffusion and the growth rate is somewhat lowered, but the nature and the robustness of the instability are not changed. These results are in agreement with scaling arguments.

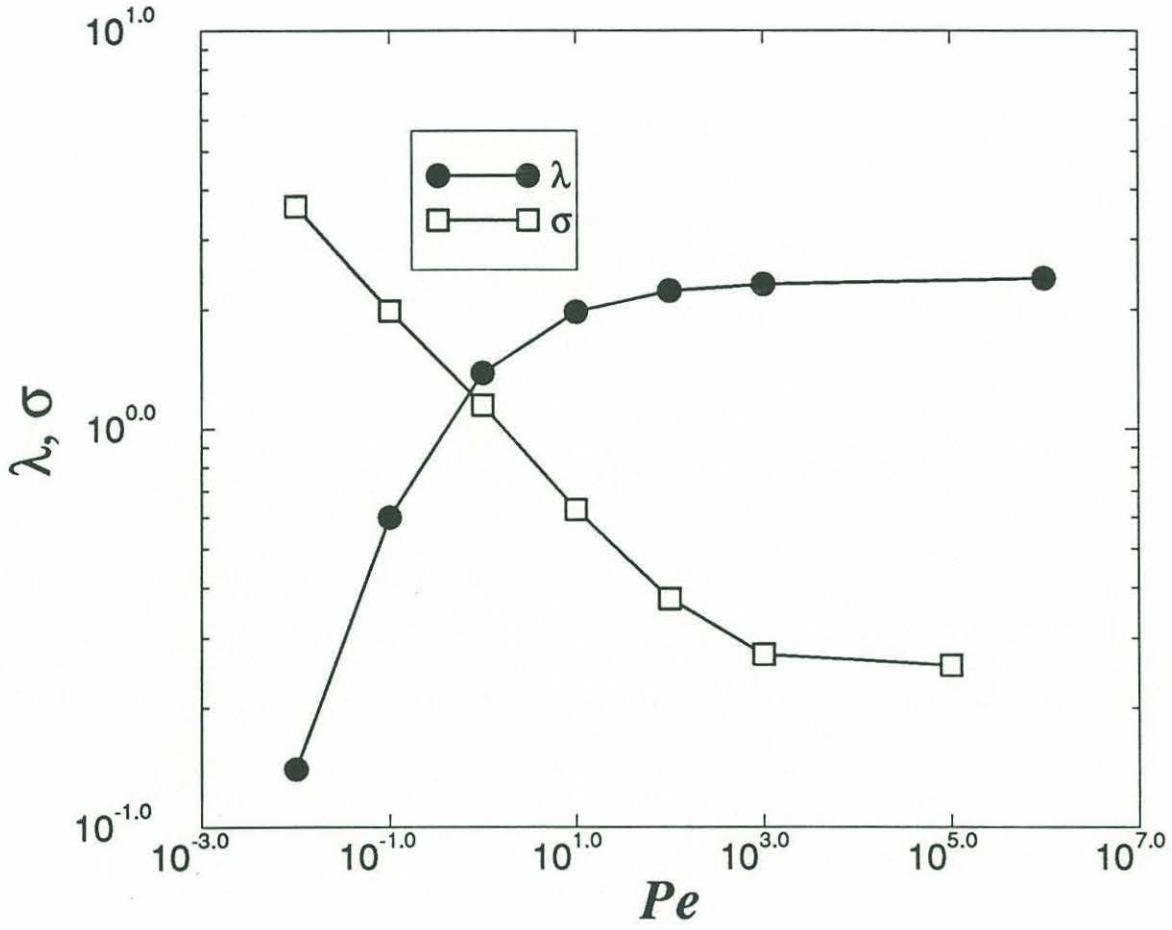

Figure 3-8: The fastest growing horizontal wavelength, $\lambda_x = 2\pi/l_{\max}$, derived from plots similar to Figure 3-7 with different Pe numbers, for a rigid medium with a constant $Da = 10$, plotted by solid circles. In the case of strong diffusion, when $Pe < Da$, $\lambda_x^4 \propto 1/Pe$. On the same plot we show the growth rate σ by open squares, to be unaffected by diffusion when Pe is large but to be reduced when diffusion becomes important. Channels will grow ($\sigma > 0$) for all diffusion rates.

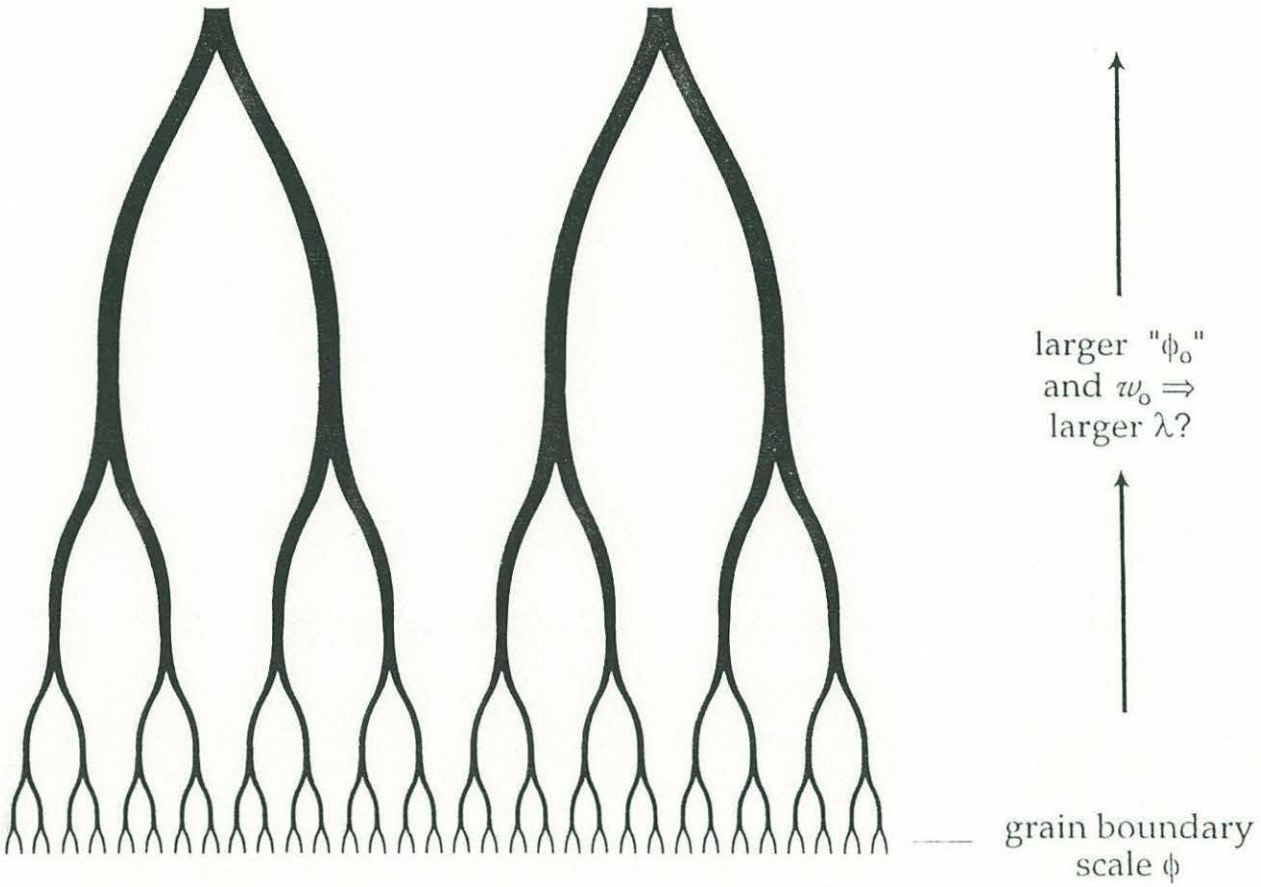

Figure 3-9: When high-porosity channels form, the solid-liquid surface area per unit volume is reduced and the characteristic equilibration length of the system will increase. This means that the wavelength of the channels will increase as well (from equation (55)). If we also consider the increase in melt velocity with height, we get an additional increase in L_{eq}. Thus we can tentatively propose the following picture: narrow channels that form deep in the melting column will act as the background porous structure for a higher level and, due to the increase in horizontal wavelength with equilibration length, will coalesce to form an interconnected network of high porosity tubes similar to the upside down "fractal tree" proposed by [22].

Chapter 4

Simulations of flow and reaction in porous media

Abstract

I present a $3D$ computer model that simulates flow and reaction through a porous medium, by solving the relevant mass conservation partial differential equations and Darcy's law. Reaction generally results in re-organization of the porous media. Dissolution causes focused and highly correlated flow patterns, while deposition reduces correlations in the spatial arrangement of porosity, so as to cause dispersion of flow. Three specific experiments relevant to melt migration in the mantle are also performed. The first simulates conditions in upwelling melt beneath mid-ocean ridges, where I find formation of high permeability channels as predicted in Chapter III. The second experiment simulates conditions for upwelling melt beneath intra-plate volcanos or magmatic arcs, where melt crystalization is expected. Simulations of such conditions indicate increasingly diffuse and homogeneous porous flow, even when flow was initially channelized. The third experiment is of melt changing from corroding the matrix to depositing in the matrix. In the transition zone a low porosity cap forms over a high porosity region, with rapidly increasing overpressurization. The results have implications for degree of chemical equilibration of melt in different regions as well as for dominant modes for melt migration (i.e., whether porous channels or periodically forming cracks will appear).

4.1 Introduction

In this paper I present a newly developed $3D$ numerical model of flow and reaction through a porous media, and initial results from it. There are not many studies about

coupled flow and reaction, even less about deposition, and none of the existing ones handles both deposition and dissolution. This work aims, first of all, to study the evolving nature and statistics of reacting porous media and to establish the differences between dissolution and deposition as opposite processes. The secondary aim of this work is to perform some initial numerical experiments mimicking different environments for upwelling melt in the mantle, and compare the results to existing observations and predictions.

The method of study involves solving a set of partial differential equations, which describe mass conservation of fluid and rock, and Darcy's law. This mathematical description is applicable to scales above the pore size, where one can define an average porosity and permeability. The resulting set of coupled equations is solved on a computer (a SUN workstation) using a Multi-grid method [61] to obtain the pressure field. This efficient method enables inclusion of up to 64^3 nodes on a workstation, where memory availability limits simulations of larger boxes.

Before deciding upon a macroscopic partial-differential-equation solver I have attempted two additional numerical methods, which I will spend a brief paragraph to describe, in the dim chance that it will save somebody some work in the distant future. First I constructed a version of the lattice-gas method [66] in which particles flow and react on a lattice. This method proved to be well suited for microscopic simulations. The initial results were easy to obtain and provided qualitative indicators, but I was unable to continue into quantitative, large scale studies, due to size limitations. The description of the model and the initial results are presented in [36]. I then proceeded to implement a network model in which a reactive fluid flows through pipes of various sizes and may change the radius of the pipes by chemical reaction. At first glance this method seemed most promising, but it is limited by the need to solve for transport of solute. This is done either by particle tracking methods, which limit the size of the system to be investigated similar to the Lattice-Gas and other microscopic methods, or by differential equation solutions, which have the limitations of macroscopic models. Thus I concluded that for quantitative study of large scale organization a macroscopic model that solves a set of partial differential equations

would provide the most useful tool.

In the first section of this chapter I mathematically describe reactive flow through a porous medium, similar to the macroscopic description in Chapter III [3], but here in the rigid medium limit. In the second section the computer method is described and validated. In the final section I present two different sets of experiments of dissolution and deposition in a porous media.

The first set of experiments constitutes a basic study of $3D$ flow and reaction in a porous media. The statistical and general properties of the porous media are investigated, after a dissolving or depositing fluid have flown through it. Results from dissolution and deposition are compared to one another and to the initially randomly constructed media.

The second set of experiments is aimed at mimicking (very simplisticly) conditions of melt ascending beneath (1) mid-ocean ridges, similar to the situation described in Chapter III, and (2) subduction-related magmatic arcs or intraplate hot spots. Geochemical observations on lavas and mantle samples indicate that melt ascending beneath mid-ocean ridges is out of chemical equilibrium with surrounding mantle [28, 27], while observations of lavas and mantle samples from hot spots and arcs generally indicate extensive reactions (for review see [36]). Such geochemical observations are accompanied by geological observations of different structures for melt transport in the two cases: replacive dunites in the case of mid-ocean ridges and fractures for intraplate basalt. This set of experiments is a continuation of work initiated in [36] and Chapter III, in which the chemical and geological observations are explained by the different chemical interactions that occur between melt and the surrounding matrix: In midocean ridges, dissolution channels form when melt upwells in close to adiabatic conditions [36, 3, 32]. In hot spots and arcs, melt must pass through a conductively cooled tectosphere and so crystallize, possibly resulting in an overpressurized and finally cracked media [36]. In addition to checking the flow patterns in these two different cases, I also simulate the transition between dissolution and deposition, (a transition likely to happen as melt passes from a an adiabatic to a conductive geotherm) and discuss the likelihood and position of fracture initiation.

All simulations were performed with relatively high reaction rates and low diffusivities so as to maximize observed trends and minimize simulation times. The sets of experiments are by no means exhaustive. For discussion of the effect of varying the different control parameters see Chapter III, [80, 67] and [9].

4.2 Formulation of the problem

The description derived below is close to previously used forms [14, 57, 3], but here an analytical description of deposition is added. The mathematical formalism uses a conventional continuum approach suited for description of phenomena that occur at and above the Darcy scale.

4.2.1 General Equations

Mass conservation equations are:

$$\frac{\partial \rho_s(1-\phi)}{\partial t} = \sum_i \Gamma_i, \tag{4.1}$$

$$\frac{\partial \rho_f \phi}{\partial t} + \nabla \cdot (\rho_f \mathbf{v} \phi) = -\sum_i \Gamma_i, \tag{4.2}$$

$$\frac{\partial \rho_s(1-\phi)c_i^s}{\partial t} = \nabla \cdot [D_i^s \rho_s (1-\phi) \nabla c_i^s] + \Gamma_i, \tag{4.3}$$

$$\frac{\partial \rho_f \phi c_i}{\partial t} + \nabla \cdot (\rho_f \phi \mathbf{v} c_i) = \nabla \cdot [D_i \rho_f \phi \nabla c_i] - \Gamma_i, \tag{4.4}$$

where ϕ is the porosity, ρ_s and ρ_f are the solid and fluid density respectively in kg m^{-3}, and Γ_i is the mass transfer rate of mineral i from fluid to solid in kg m^{-3} $s^{-}1$. D_i and D_i^s are the diffusion coefficients of component i in the fluid and solid respectively and c_i, c_i^s are the mass fractions of component i in the fluid and solid respectively, with $\sum_i c_i = 1$ and $\sum_i c_i^s = 1$.

Equations 4.1 and 4.2 describe the conservation of total solid and fluid mass respectively. Equations 4.3 and 4.4 describe the conservation of each mineral component in the solid and fluid phase respectively.

Assuming first-order chemical reaction kinetics, the rate of mass transfer of com-

ponent i between fluid and solid is

$$\Gamma_i = R_i A_i(\mathbf{x}, t)(c_i - c_{eq_i}), \tag{4.5}$$

where R_i is the reaction rate constant of component i in kg m^{-2} s^{-1} and $A_i(\mathbf{x}, t)$ is the effective specific surface area (m^2/m^3) available for reaction of component i. c_{eq_i} is the equilibrium concentration of mineral i in the fluid, given in mass fraction. c_{eq_i} may be a function of position and time, as in the case for varying temperature or pH conditions. The specific surface area, $A_i(x, t)$ is also, in general, a complex function which has different values depending on whether a mineral is dissolving or depositing, and may depend on the presence of other minerals. Here I shall approximate $A_i(x, t)$ in a simple form. The effective specific surface area for dissolution, termed A_i^{diss}, is a function of the amount of mineral i available for dissolution at the pore-grain interface. Since $M^s{}_i = \rho_s c^s{}_i(1 - \phi)$ is the mass fraction of solid component i,

$$A_i^{diss}(c^s, \phi) \propto M^s{}_i^{2/3} \propto (c_{s_i}(1 - \phi))^{2/3}. \tag{4.6}$$

Equation 4.6 arguably applies to dissolution and not to deposition, since dissolution is limited by the mass of soluble material in the solid phase, while deposition is generally independent of the amount of mineral already existing in grains, but depends only on the total surface area exposed in the pores. Since the volume fraction occupied by pores is ϕ, the specific surface area associated with this volume fraction will be approximately

$$A_i^{dep}(\phi) \propto \phi^{2/3}. \tag{4.7}$$

The closing equation is Darcy's law, which relates the pressure p to the flux of the fluid:

$$\phi \mathbf{v} = -\frac{k}{\mu} \nabla p, \tag{4.8}$$

where μ is the viscosity of the fluid, p is the pressure in excess of hydrodynamic pressure, and k is the permeability.

The relation between the permeability and the geometry of the matrix is important for correct modeling of the non-linear process involved in this study, but a clear analytical description is not obvious. For example, it is possible that by selective

deposition (or dissolution) in strategically positioned necks the porosity will be hardly changed, while the permeability will be highly altered. Never the less, in the literature (e.g. [8, 88]) permeability is usually taken to be a power law function of the porosity

$$k(\phi) = d^2\phi^n/b, \tag{4.9}$$

with d a typical grain size, n usually between 2 and 3, and b a constant. This relation is not very good for low porosities, but is used in this study for lack of a better description, and as a first, even though not perfect, step. This approximation can be partially justified when one realizes that the discretized version of the set of equations presented above (4.1-4.9) is identical, when $n = 2$, to the set needed for solving for flow and reaction through a network of tubes. Thus, similarly to a network model, each node (in the network model representing a tube) by itself obeys 4.9, but the global arrangement in space may result in macroscopic porosity-permeability relations that are different than 4.9.

Boundary conditions. In general, equations 4.1-4.9 will require either pressure or flux boundary conditions on both the total fluid mass and on each individual fluid component. Initial conditions on ϕ and c_i are also needed in order to determine the spatial and temporal evolution of the six (in the case of a single soluble component in $3D$ flow) unknowns $\mathbf{v}$, p, ϕ and c.

4.2.2 Simplifications

For simplicity, I assume that the solid phase is composed of two components: a soluble component which can chemically react with the fluid by dissolution or precipitation, and a insoluble component. The soluble material has mass fraction c_s in solid and reaction rate R while the non-soluble component has mass fraction $1 - c_s$ in solid and its reaction rate is 0. Diffusion within the solid will be considered negligible. The fluid phase is composed of a carrier fluid with mass fraction $1 - c$ and a dissolved component with mass fraction c. The carrier fluid does not enter the solid phase. The density of the fluid and solid phases are presumed constant as the composition

of the melt changes due to chemical reaction. The subscript i will be dropped from this point on.

In this simplified case we can use 4.3 to write the mass conservation equation of the non-soluble phase,

$$(1 - c_s)(1 - \phi) = V_{ns} = const. \tag{4.10}$$

From 4.10, 4.6 and 4.7 we write the effective surface area as a function of the porosity only:

$$A(\phi) \propto \begin{cases} (\phi_f - \phi)^{2/3} & \text{if } c < c_{eq} \\ \phi^{2/3} & \text{if } c > c_{eq} \end{cases} \tag{4.11}$$

where $\phi_f = 1 - V_{ns}$ would be the final porosity if all soluble material is dissolved. Equations 4.1-4.4 can now be written as

$$\frac{\partial \phi}{\partial t} = -\Gamma/\rho_s, \tag{4.12}$$

$$\frac{\partial \phi}{\partial t} + \nabla \cdot (\mathbf{v}\phi) = -\Gamma/\rho_f, \tag{4.13}$$

$$\phi \frac{\partial c}{\partial t} + \phi \mathbf{v} \cdot \nabla c = D\nabla \cdot (\phi \nabla c) - (1 - c)\Gamma/\rho_f, \tag{4.14}$$

$$\Gamma = RA(\phi)(c - c_{\mathrm{eq}}), \tag{4.15}$$

where 4.14 is a result of subtracting 4.2 from 4.4 and equation 4.3 has been used to determine the reactive surface area for dissolution, and will not be followed individually anymore.

4.2.3 Nondimensionalization.

In nondimensionalizing equations 4.11-4.15 and 4.8, I define characteristic effective permeability as $k_0 = d^2\phi_0^n/b$, and characteristic flux as $\phi_0 w_0 = k_0 p_0/\mu L$, where L is a length scale of interest, and p_0 is the characteristic pressure difference across L. A characteristic concentration is defined as $c_0 = \bar{c}_{eq}$, which scales the concentration c to the spatial and temporal average of the equilibrium concentration c_{eq}. This definition reduces to $c_0 = c_{eq}$ when the equilibrium concentration is constant. Finally a characteristic surface area for reaction will be defined as $A_0 = \phi_0^{2/3}$.

I next define the nondimensional variables, denoted by primed letters:

$$\begin{aligned}
\mathbf{x} &= L\mathbf{x}' \\
\phi &= \phi_0\phi' \\
p &= p_0p' \\
v &= w_0v' \\
t &= \frac{L}{w_0}t' \\
c &= c_0c' \\
c_{eq} &= c_0f(\mathbf{x},t) \\
\phi_f &= \phi_0\phi_f'
\end{aligned}$$

Lastly, two controlling parameters emerge in the problem:

$$Da = \frac{RLA_0}{\phi_0 w_0 \rho_f} \tag{4.16}$$

$$Pe = \frac{w_0 L}{D}. \tag{4.17}$$

Equation 4.16 defines the Damkholer number, which measures the advection time scale versus the reaction time scale in the system. Equation 4.17 defines the Peclet number, which measures diffusion time scales versus the advection time scales in the problem.

Using the non-dimensional variables and parameters, 4.8, 4.9 and 4.11-4.15 can be rewritten, after some algebra, as:

$$\frac{\partial \phi'}{\partial t'} = -c_0\frac{\rho_f}{\rho_s}\mathrm{Da}\Gamma' \tag{4.18}$$

$$\nabla\cdot(\phi'^n\nabla p') = c_0\frac{\rho_s-\rho_f}{\rho_s}\mathrm{Da}\Gamma' \tag{4.19}$$

$$\phi'\frac{\partial c'}{\partial t} - \phi'^n\nabla p'\cdot\nabla c' = \frac{1}{Pe}\nabla\cdot(\phi'\nabla c') - (1-c_0c')\mathrm{Da}\Gamma' \tag{4.20}$$

$$\Gamma' = A(\phi')(c'-f(\mathbf{x},t)) \tag{4.21}$$

$$A(\phi) \propto \begin{cases} (\phi_f'-\phi')^{2/3} & \text{if } c' < f(x,t) \\ \phi'^{2/3} & \text{if } c' > f(x,t) \end{cases} \tag{4.22}$$

This constitutes the basic set of equations for this study. From this point on primes will dropped with reference to the non-dimensional variables. Equation 4.18 describes

the temporal evolution of porosity due to reaction. Equation 4.19 describes total fluid conservation which is simply the Laplace equation for the pressure. Equation 4.20 states that mineral concentration changes due to reaction, diffusion and advection. Finally Equation 4.21 and 4.22 are used to evaluate the mass transfer rate.

4.3 Description of numerical model

The numerical method for solution of 4.18-4.22 uses an explicit partial differential equation solver which is implemented on an evenly spaced grid with grid-spacing Δ in each of the respective dimensions, and time steps of size Δt. The model uses wrap-around boundary conditions in the x and y directions, and allows for flux or pressure specifications in the $z = 0, L$ boundaries. The model is implemented as follows:

1. Given $3D$ concentration and porosity fields, find the mass transfer rate Γ everywhere using 4.21 and 4.22.

2. Given pressure or flux boundary conditions and Γ, find the $3D$ pressure field from equation 4.19. The solution of such Laplace equations are most time and memory consuming, and constitute the step that limits the size of the problem to be solved. The model uses the recently developed Multi-Grid Method [61], which requires a number of operations of order n, where n is the number of grid points. This method is able to solve larger systems than direct solvers that need a number of operations of order n^3, but unlike the direct solvers it cannot resolve high frequency features.

3. Operator splitting [61] is then used to solve for the new solute concentration, from equation 4.20. The advective contribution is calculated using the "corrected up-wind scheme" [74], a stable advection scheme with courant condition: $\Delta t|\mathbf{Q}|/\Delta \leq 1/\sqrt{3}$ where $\mathbf{Q} = \phi^n \nabla p$. The corrected upwind scheme has small implicit diffusion parallel to the flow direction. The source (or sink) term due to chemical reaction is given by Γ, calculated in step 1. The diffusion step is implemented using a first-order explicit space-centered scheme [61] (stable for

$6\Delta t/\Delta < Pe$). The stability requirement is easily met for the small diffusivities (large Pe) which I use.

4. Finally the new porosity field is obtained from 4.18, and the loop returns to step 1.

In the validation tests and the experiments described below, fluid is driven by a pressure gradient from $z = 0$ to $z = L$, with constant pressure boundary conditions.

4.4 Testing of numerical model

In order to test the model I had to concentrate on simplified cases with many symmetries, due to the lack of theoretical work in more complex cases. First, each feature of the model was checked by itself. Advection and diffusion of an initial Gaussian were tested to give the analytically predictable profile. This test did not incorporate reaction. Reaction in a uniform porous media was tested against the analytically predicted decay to equilibrium of the concentration field. This test did not incorporate advection.

For a dissolving porous media there are a few cases which incorporate both reaction and transport, and for which there are analytical predictions. I have tested my model against a few of these cases. The test I present is a comparison of the numerical and predicted dispersion curves for the reactive infiltration instability. The analytical results are derived for reaction and flow in a two dimensional porous media, and therefore this test constitutes the most demanding of all available analytical ones.

For deposition in a porous media there are no available analytical calculations which incorporate both reaction and advection, and so I will only present a test of reaction in a uniform porous media, and rely on the fact that deposition and dissolution are nearly symmetrical process, and that the combined non-linear effects of the reaction and transport were shown to be consistent with theory in the previous test.

4.4.1 Test 1: The reactive infiltration instability in $2D$

When an undersaturated fluid is forced to flow through a partially soluble porous media, a propagating reaction front will form [14, 57]. Upstream of the reaction front, where all the soluble material has already been dissolved, the concentration will be that of the incoming undersaturated fluid. Downstream of the reaction front, the fluid will be in chemical equilibrium with the solid (i.e., saturated) and no dissolution will occur, provided that $Da \gg 1$. The position of the front is unstable to small perturbations: if the initial permeability is slightly higher in a certain region, this region will entrain more unsaturated fluid and dissolve more rapidly, thus increasing its porosity even further in a positive feedback mechanism. [57] present a detailed analysis of this instability in $2D$ [1]. They predict that for small perturbations, the front will develop scalloped fingers that grow in an unstable manner with time, such that any initial sinusoidal perturbation in position will grow as

$$\zeta(x,z,t) = \bar{z}(t) + \sum_m A_m \cos(mx) e^{\omega(m)t}, \tag{4.23}$$

where $\omega(m)$ is the growth rate of the wavelength $2\pi/m$ and $\zeta(x,z,t)$ is the position of the front, with average height $\bar{z}(t)$. The resulting dispersion relation is a function of the diffusion, advection, and reaction rates. [57] assume that $c_{eq} = c_0 = const$, $c_0/\rho_f << 1$ and $\rho_f = \rho_s$. Non-dimensionalization is performed with $t = L(w_0 c_0)^{-1} t'$. Their assumptions are analogous to having very fast reactions (i.e., $Da \rightarrow \infty$), or an infinitely thin reaction front. The analytical prediction for the linear growth rate $\omega(m)$ in this case is:

$$\omega(m) = \frac{\phi_f v_f}{(\phi_f - \phi_b)(1+\gamma)} \left[\alpha + (1-\gamma)m - (\alpha^2 + 4m^2)^{1/2}\right] \tag{4.24}$$

where v_f is the final fluid velocity after the front has passed, ϕ_b is the porosity before the passage of the front, $\alpha = Pe * v_f$ and $\gamma = \phi_b k_b / \phi_f k_f$ where k_b, k_f are the permeabilities before and after the passage of the front.

To measure $\omega(m)$, I performed a set of simulations, where flow enters a box (33 nodes per side) at $z = 0$ with initial concentration $c = 0$. An initial front between ϕ_b

[1] There is a slight mistake in their paper in the basic fluid conservation equation, but since this mistake is of order ϵ it does not effect the final result.

and ϕ_f was placed at $\zeta(x,z,0) = \bar{z} + A\sin(m_x x)$. The fluid was allowed to react with the porous media and the power spectrum of the porosity, $S(\mathbf{m},t)$, was obtained. The amplitude of the $3D$ power spectra in the seeded wavelength, $S(m_x,t)$, was checked as a function of time. To derive $\omega(m_x)$ from such measurements, I use 4.23 in the following formula: $\omega(m_x) = \ln(\sqrt{(S(m_x,t)/S(m_x,0))})/(tc_0)$, where c_0 is a parameter needed to convert between the two different time scales used in this paper and in [57]. The results are plotted in Figure 4-1.

4.4.2 Test 2: Deposition in uniform porous media

Since I do not know of any existing analytical prediction for combined flow and deposition in a heterogeneous porous media, I performed a primitive test for flow and deposition in a uniform porous media. Supersaturated fluid fills a uniform porosity box, where I allow for wrap-around boundary conditions in z as well as the usual wrap around conditions in x and y. In this case one expects no spatial concentration gradients. For $c_0\rho_f \ll \rho_s$, the change in porosity at short time scales is negligible (from equation 4.18). In this case equation 4.4 has a solution of

$$c(t) = 1 - \exp\left(\frac{-ADa\, t}{\phi}\right). \tag{4.25}$$

Figure 4-2 shows that simulation results follow theoretical predictions closely.

4.5 Simulations and results

In this section I present various types of computer experiments and their results. The experiments are exploratory, since there is very little previous quantitative knowledge about combined reaction and flow through porous media, and what exists is mainly aimed at dissolution. Many of the results will be quantified by measuring the correlation function, $c(\mathbf{r})$, of different variables in the system. The correlation function in all experiments is obtained using the Weiner-Khintchine theorem (e.g., [11]). Practically, this is done by taking the inverse fourier transform of the $3D$ power-spectra of the field of interest (e.g. porosity or flux). $c(\mathbf{r})$ is then normalized to 1, and ranges between -1

and 1. The correlation function gives a quantitative indication of the probability of finding identical values of the investigated scalar field at 2 different points separated by a distance vector r, as explained in more detail in the introduction of Chapter II.

4.5.1 General dissolution and deposition

This section presents a set of simple experiments. Reactive fluid flows through a $3D$ porous media, which is wrapped around in the z as well as the usual x, y directions. Porosity in the initial configuration is white Gaussian noise around a mean. The fluid in these experiments is kept artificially from reaching chemical equilibrium in order to observe the effect of long term reaction. The fluid is kept undersaturated (in the dissolution experiments) or supersaturated (in the deposition experiments), by readjusting the mean concentration at each time step to a given constant value.

Figure 4-3 shows average porosity within the box as a function of time for (a1) dissolving porous media and (b1) clogging porous media. Porosity asymptotically approaches ϕ_f in the dissolving case and 0 in the depositing case, following equation 4.22. Figure 4-3 also shows final $2D$ sections of the flow field, parallel to the flow direction, for a porous media subjected to (a2) flow and dissolution and (b2) flow and deposition.

Dissolution. When an undersaturated reactive fluid flows through a rock, one expects focusing of flow due to processes that preferentially dissolve regions of high initial permeability, similar to the reactive infiltration instability.

Figure 4-4 show the evolution of flux (a1) and porosity (a2) histograms and the porosity correlation function (a3) due to dissolution. The porosity histogram (Figure 4-4(a2)) after 700 time steps of dissolution shows only a slight increase in variability from its initial state. On the other hand, the flux histogram (Figure 4-4(a1)), shows a great amount of variability compared to its initial configuration. This can be explained by the rearrangement of the pore distribution in a correlated way, so as to form elongated high permeability pipes with high flux, alternating with regions of low permeability and low flux. The contrasting fast and slow regions of flow thus reflect

the variability in permeability due to spatial organization of porosity, rather than due to the actual change in porosity itself. This can be clearly observed in Figure 4-4(a3) as an increase in the correlation function of the porosity in the direction parallel to the flow (lag in z), which means that high porosity is likely to be found below or above other regions of high porosity while low porosity regions will be found adjacent to other low porosity regions (i.e., elongated pipes). This increased correlation function is most prominent along the flow direction, indicating that the medium has become anisotropic.

Deposition. An interesting and not well understood problem is how flow reorganizes as deposition clogs the porous media. Qualitatively, one expects that since fluid flows faster in regions of high permeability, it will tend to remain further from equilibrium in those regions. In the case of deposition this means that fluid retains a higher supersaturation in the high permeability regions, and thus will be able to deposit more in these regions. This process is expected to cause a negative feed-back: any highly permeable regions are choked by increased deposition, and the flow becomes more diffuse with time.

This phenomena is observed in our simulations. Most of the deposition occurs in the high permeability regions, where the fluid tends to clog the smaller necks, thus effectively blocking initially preferred paths for flow, and causing flow to become diffuse and uniform, as observed in the spiky flux histogram in Figure 4-4(b1). On the other hand, the porosity distribution is not much narrower than in its initial state (Figure 4-4(b2)). It is thus probable that reduction of correlations in the permeability path are responsible for flow dispersivity and uniformity, as opposed to homogenization of porosity. The correlation function of the porosity, shown in Figure 4-4(b3) demonstrates that correlations along the direction parallel to flow are somewhat reduced at small z lag.

The reduction of correlations, and the possible formation of negative correlations, can be explained in the following way: since deposition is a function of the flux of supersaturated material, it will occur most rapidly in the main paths for flow. These

paths are regions of connected, relatively high permeability, present in the initial random arrangement. Deposition in these paths will reduce the upstream permeability and preferentially cause regions of clogged low permeability to be connected to downstream regions of high permeability, which may result in negative correlations.

4.5.2 Dissolution and deposition in mantle flow

In this section I present results from simulations directly aimed at better understanding flow and chemical patterns of melt upwelling in the mantle, under various conditions.

The first experiment is for fluid increasingly able to dissolve the porous matrix through which it is flowing. This problem is set to mimic aspects of melt flow in upwelling mantle beneath mid-ocean ridges, where decompression of ascending mantle causes an increase in solubility of solid phases with height [72, 36]. A $2D$ linear compacting system was studied in Chapter III [3] and showed the formation of fast flowing melt channels. The $3D$ non-linear problem (in the rigid limit) is investigated here.

The second experiment is for melt ascending while crystallizing. [36] asserted that when melt ascends beneath magmatic arcs and hot spots volcanos it will first dissolve the surrounding mantle, similar to the situation in midocean ridges. But, in contrast to midocean ridges, it will encounter a wide region of conductively cooled, static mantle below the crust, and so the melt will cool to below the pyroxene saturation point and begin to crystallize. Numerical simulations are set to investigate flow patterns in such crystallizing regions.

The third experiment investigates the transition zone between dissolution and crystallization. Zones of transition between high and low permeability have been proposed for "magma pooling" and overpressurization, and as probable places for fracture initiation [86, 56, 36]. Kelemen et al. [36] emphasized that these are particularly likely where melt-rock reaction undergoes a transition form net dissolution, under adiabatic conditions, to net precipitation, under conductively cooled conditions.

Melt fraction increasing upstream (adiabatic conditions). The experimental conditions are such that fluid enters at $z = 0$ with concentration $c = 0$. The entering fluid is in equilibrium with the surrounding matrix. The equilibrium saturation increases linearly upstream, so that $c_0(z) = z/L$, where z is the height and L is the length of the box, (in Δ). The local concentration is thus a balance between reaction and advection of undersaturated material form downstream, as explained in Chapter III. For $Da \gg 1$ the fluid maintains a close to equilibrium concentration, but dissolution occurs rapidly leading to channel formation as predicted in Chapter III for $2D$. Figure 4-5a shows a vertical slice (parallel to the flow direction) of the $3D$ flux field after channels have been established by the dissolution process. Figure 4-6a and b show the correlation function in the direction parallel and perpendicular to the pressure gradient, respectively. Flow is focussed and thus exhibits strong correlations in the direction parallel to flow. Weak correlations are found in the perpendicular direction. These represent formation of channel-like features, with a characteristic size larger than the grid spacing. The medium is anisotropic, with vertical high permeability channels spanning the box.

Melt fraction decreases upstream (conductively cooled conditions). Fluid enters at $z = 0$ with solute concentration $c = 1$. At the entering height the fluid is in equilibrium with the matrix. The equilibrium saturation decreases linearly upstream so that $c_{eq}(z) = 1 - z/L$ where z is the height and L is the length of the box. This renders the fluid constantly, very slightly, supersaturated with respect to its height. A simple calculation, similar to that presented in the calculation of the steady-state of Chapter III, can be made to prove this. The initial porosity field for this experiment is not a random distribution, but instead the "channelized" porous media formed in a previous dissolution experiment. (The section shown in Figure 4-5a is a section from the initial flow field in this experiment.)

Figure 4-5b shows a slice parallel to the flow direction of the $3D$ flux field after 800 time steps. The initial channels of flow have been completely wiped out, except for remnants at $z = 0$, where the fluid enters at equilibrium and so no reaction

occurs. Figure 4-6a and b show the correlation function in the direction parallel and perpendicular to the flow, respectively. Deposition has completely destroyed the initial correlations (channels of flow) obtained by dissolution, so as to cause uniform and diffuse flow. In Figure 4-5b one can also observe the reduction in flux variability reminiscent of the results presented in Figure 4-4(b1).

The transition to Pyroxene saturation. To simulate the transition from dissolution to deposition, fluid enters at $z = 0$ with $c = 0$. The matrix is increasingly soluble until $z = L/2$ by having $c_{eq} = z/L$. At $z = L/2$, c_{eq} begins to decrease linearly and $c_{eq} = 1 - z/L$. The z profile of the equilibrium saturation and the resulting concentration profile (averaged over x and y, after 400 time steps) are drawn in solid line and stars respectively in Figure 4-7a. Melt is undersaturated ($c < c_{eq}$) for more than half of the box, i.e. concentration profile attains a maximum at a higher z than does the equilibrium concentration. The vertical distance between the maximum in concentration and the point of inversion in equilibrium concentration is determined by the Da: The deviation from equilibrium is a result of the competition between advection of downstream undersaturated material and equilibrating chemical reaction. As reaction rates increase ($Da \rightarrow \infty$), the concentration profile approaches that of c_{eq}, but $z(max(c))$ will remain greater than $z(max(c_{eq}))$ for any finite flow rates.

Vertical sections of the resulting $3D$ flow pattern are presented in Figure 4-8. Flux channels form in the dissolving region and extend somewhat into the precipitation region. Pressure sections, on the other hand, vary only along the z direction, and appear constant in x and y. Thus only z profiles of pressure are shown.

Figure 4-7b shows average (over x, y) porosity and deviation from hydrostatic pressure as a function of z. Melt fraction (porosity, plotted in circles) increases to half the box, after which a rapid decrease in porosity occurs so as to form a low permeability cap over the molten region. The peak in porosity corresponds to the largest deviation of c from c_{eq}, attained at the peak of c_{eq}.

The deviation of "measured" pressure from hydrostatic pressure is plotted as a solid line in Figure 4-7b. Overpressure attains a maximum at the same height as

does $c(z)$, i.e., the point of transition from net dissolution to net deposition. As discussed above, the vertical distance between the two points, the point where porosity is maximized and the point where overpressure is maximized, is determined by the Da, and decreases as $Da \rightarrow \infty$. In this rigid matrix, the difference in porosity between the molten and the crystallized regions, and the overpressure associated with the transition, continue to increase with time. The consequences of such a physical scenario will be discussed in the conclusions.

4.6 Summary and conclusions

In this study I have presented a new three-dimensional computer model which efficiently models Darcy-scale aspects of flow and chemical reaction, both deposition and dissolution, in a porous medium. Simulations of generic and specific process were performed, and the following conclusions for flow and reaction at high Da and Pe numbers, are reached:

4.6.1 General conclusions.

Reaction in porous media at high Da causes spatial rearrangement of the porosity in the matrix with relatively little effect on the shape of the porosity histogram. Dissolution results in formation of alternating high and low permeability regions parallel to the main flow direction, while deposition acts to decrease correlations in porosity and diffuses the flow (Figure 4-4). It is possible that reactive flow is accompanied by a change in the relationship between porosity and permeability (i.e., in dissolving systems global permeability will be higher than predicted by a measured average porosity, while in depositing systems global permeability will be lower than thus predicted). However, in my simulations this effect is not observed, and the total permeability of the system is well predicted (within 1%) by equation 4.9, using the average porosity within the whole box.

4.6.2 Relevance to melt migration in the earths mantle

The simulations in this section followed closely the proposed different scenarios in [36]. The results of simulations agree with predictions in that paper.

Melt ascending beneath midocean ridges, on an adiabatic geothermal gradient. It is currently believed that the earths mantle rapidly ascends below midocean ridges in near adiabat conditions and remains above the point of pyroxene saturation for most of its ascent path, continuously increasing in liquid mass [72, 36]. Under such conditions, simulations show that three dimensional, elongated channels of fast flowing, undersaturated melt form spontaneously. The vertical channels span the box size, similar to the two dimensional linear predictions obtained in Chapter III.

As detailed in Chapter III and in [36] and [32], the spontaneous formation of such channels may explain the observation of chemical disequilibrium between midocean ridge basalt and surrounding depleted peridotite [28, 27]. Some kind of channels have long been assumed in order to explain the geochemical observations [79, 22], but a formation mechanism for channels in the viscously deformable parts of the mantle was not known.

Melt ascending and cooling on a conductive geotherm (intra-plate volcanism and subduction arcs). Beneath hot spot volcanos, ascending melt follows an adiabatic path to the base of the tectosphere, but will cool at shallower levels. Thermal models of subduction zones indicate that melt initially heats and then cools as it ascends through the mantle wedge. In both cases, PT diagrams as shown in [36], reveal that melts rising through the upper mantle will first increase and then decrease in mass.

I find that when liquids increasingly crystallize, flow becomes diffuse and homogeneous, even if initially focused into channels. This result is in agreement with the chemical signature of basalts and mantle samples obtained from such regions ([36] and references therein), which show a closer approach to equilibrium and slower melt

extraction rates, in contrast with midocean ridges.

Simulations show that, at least in a rigid medium, a low porosity cap will form at the transition from dissolution to crystallization. The sharp transition from a region with high melt fraction to a region of low permeability causes rapidly increasing overpressurization. Such regions, whose depth in the mantle it may be possible to calculate from thermodynamic considerations, will be candidates for periodic hydrofracturing, due both to the high melt fraction and the overpressurization [36].

A relevant question concerning the initiation of hydrofractures in this region, is whether compaction forces can dissipate the excess pressure faster than the rate at which it increases due to a buildup of a low permeability cap. It has been argued that in steady-state, compaction will dissipate any stress differences larger than $\Delta\rho gh$, the buoyancy forces obtained over a compaction length h [81]. This calculation is not true in a medium constantly changing due to chemical reactions. Compaction, which acts to dissipate the overpressure, will be competing against crystallization, which acts to build up pressure. The faster of these two processes will determine the resulting overpressure.

The above findings are consistent with geological evidence for dunite dissolution features found in mantle structures in ophiolites preserved from adiabatic upwelling beneath an oceanic spreading ridge [32], and fractures filled with products of crystallized, cooled basalt found in mantle sections preserving structures formed within a conductive geotherm.

4.6.3 Open question and future investigations

The model presented above assumes a constitutive porosity-permeability relation given by equation 4.9. This is the first point for suggested improvement, since as stated previously, it is possible to deposit at strategic small necks, with a very small effect on porosity but a tremendous effect on permeability.

How to improve 4.9 is not immediately clear. One way is to use particle based models, such as the Lattice-Gas model, where porosity-permeability relations emerge physically, without a need for analytical predictions. But these microscopic models

are limited in size. Macroscopic modeling can be improved by imposing constitutive laws which take into account the changing situations in low porosity and assume a power n that increases as porosity is decreased in equation 4.9. Another possibility is to use only a fraction of the porosity (which can be termed the connected porosity) in the flow calculations.

Reactive infiltration instability in $3D$. Similar to the $2D$ reactive infiltration instability and as a consequence of laboratory experiments in $3D$ [17], one expects the reactive infiltration instability to form in $3D$, but it's form is yet to be fully understood. In experiments, the shape of the reaction front has been observed to have scale-invariant fingers under certain conditions [17].

Model simulations of the front propagating in $3D$ show that the front is unstable for small porosity perturbations, but forming fingers lock on the initial noisy distribution of the porosity. Increased diffusion is expected to change finger size, but I have not yet succeeded in determining the behavior of this instability in parameter space. It is necessary to simulate such a phenomena on larger boxes in order to observe possible scale invariant behavior.

Melt flow in the mantle. The channeling instability in a gradient of solubility may have interesting forms in $3D$, which need to be investigated as a function of the various parameters. This part of the study is complicated in a rigid medium, because of the lack of a steady state, and so future addition of compaction is proposed. Such tests using a numerical code that incorporates compaction, as well as reaction, will also investigate the transition from dissolution to precipitation and determine the maximum pressure obtained as a function of competing rates.

An additional point to study is temperature effects. In the earths mantle, the equilibrium concentration, and so the transition from dissolution to precipitation, are a function of temperature as well as pressure. For example, fast flowing melt in a high permeability channel may be still hot enough to be able to dissolve the solid matrix, while the neighboring regions may have already cooled enough to precipitate,

resulting in focusing of the upwelling melt in narrow chimneys with solidified walls, similar to results of the experiments reported in [36] and [82]. In the future, it would be interesting, though somewhat difficult due to the additional length and time scales involved, to incorporate temperature effects into the existing model.

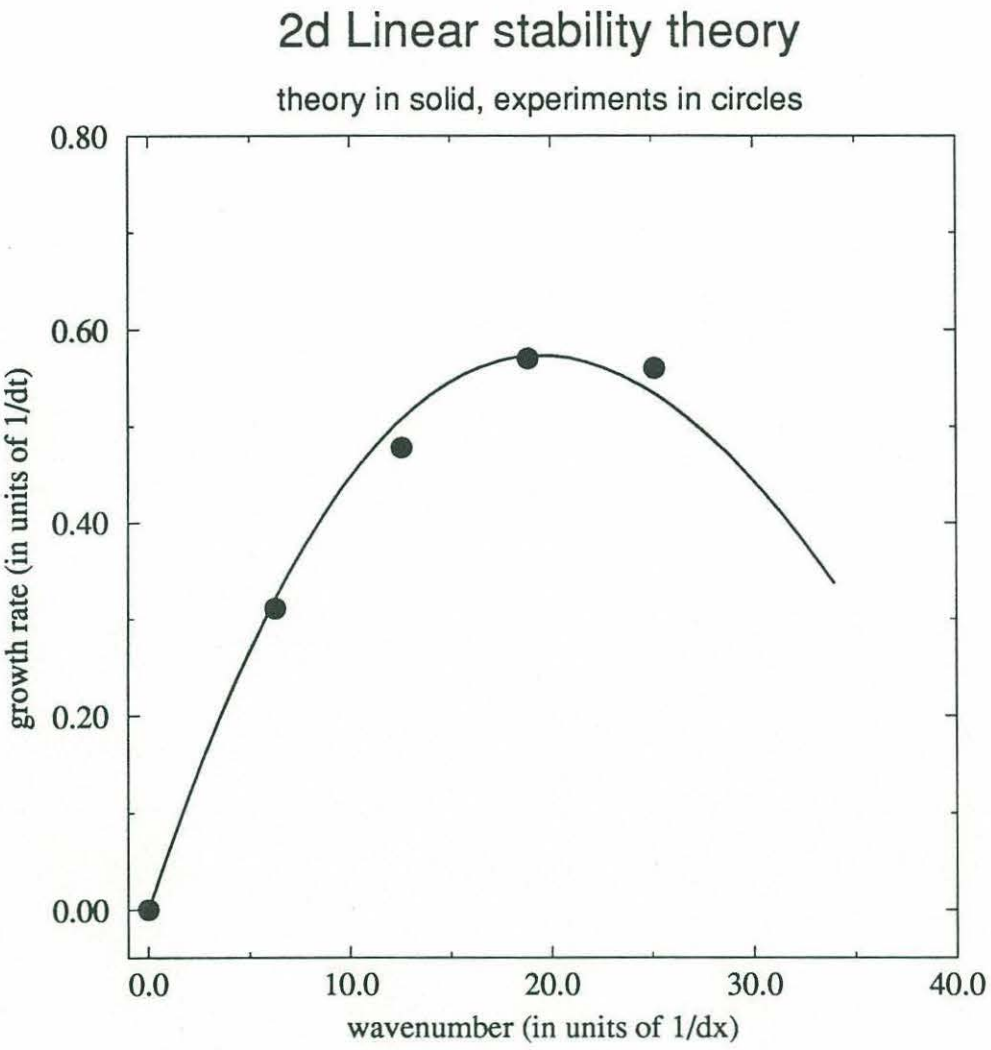

Figure 4-1: Growth rate as a function of wavenumber for the reactive infiltration instability. Results from model simulations in circles, analytical prediction from linear stability from [57] (equation 4.24) in solid line. Simulations were performed on a box with 33^3 grid points. Parameters used are: $\phi_f = 2, \phi_b = 1, \gamma = 0.125, v_f = 0.4, a = 80$ and $Da = 40$. The highest wavenumbers correspond to features close to the grid spacing. Such high frequency features are not well resolved by partial differential equation solvers such as this model.

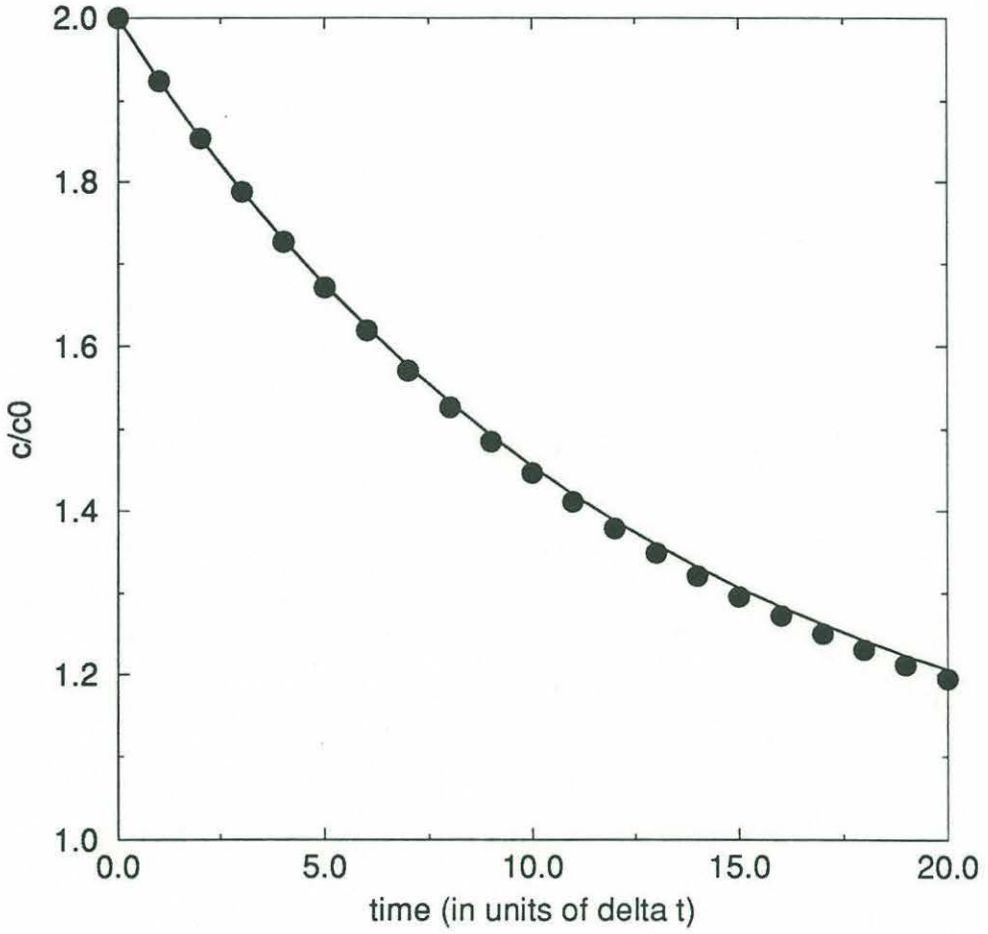

Figure 4-2: A supersaturated fluid reacting and flowing in a uniform media. Equation 4.25 describes the time evolution of the uniform concentration towards equilibrium. Parameter set used: $Da = 10, A = 0.63, \phi = 1, c_0 = 0.1, \Delta t = 0.0125$. Prediction from 4.25 in solid line. Simulation results in circles.

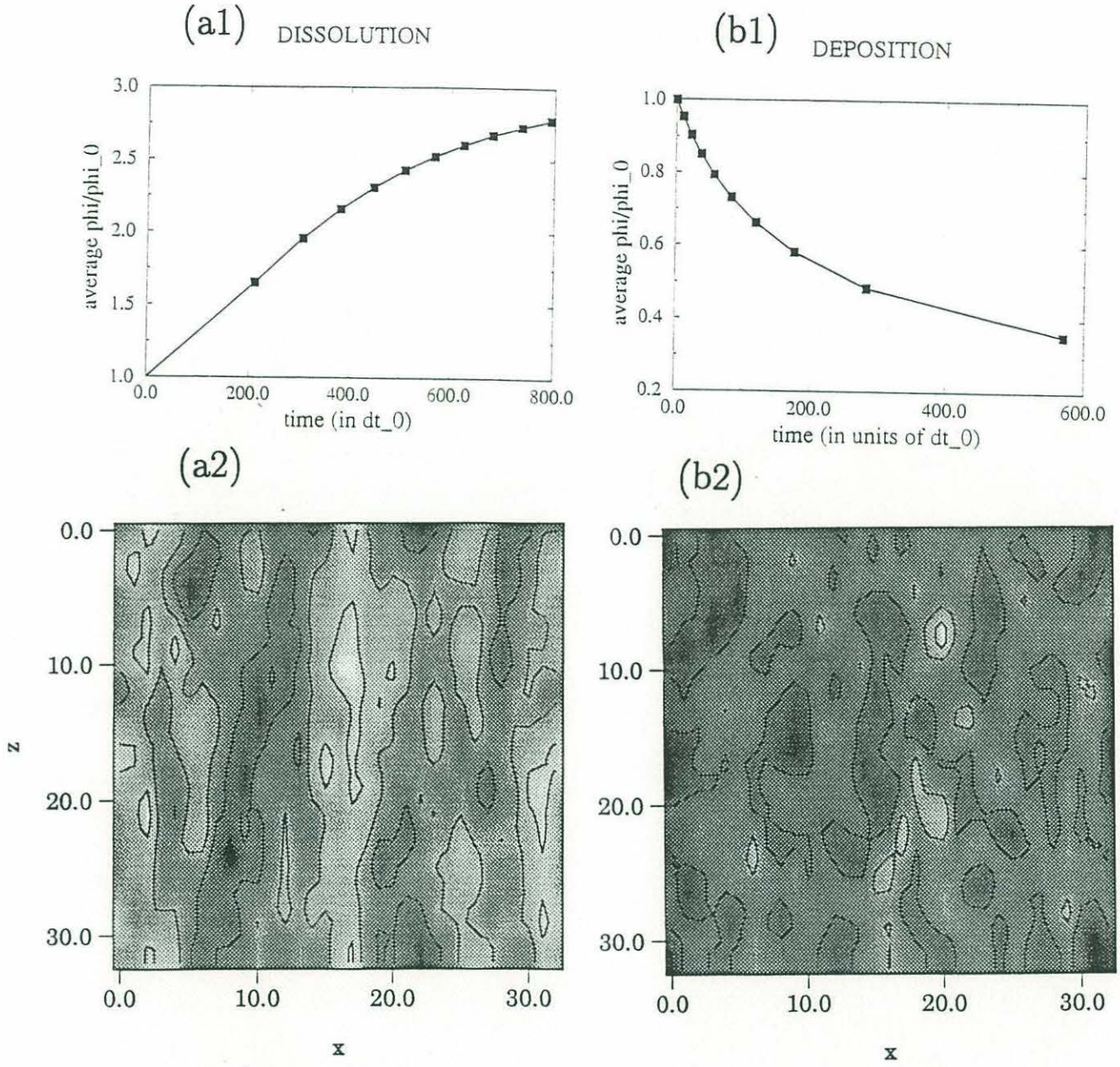

Figure 4-3: Average porosity as a function of time for (a1) dissolving porous media and (b1) porous media undergoing deposition. Porosity in both cases approaches a limiting value: in a dissolving matrix $\phi \rightarrow \phi_f$ (the porosity when no more soluble material is present), and in a depositing porous media $\phi \rightarrow 0$. Time is counted in units of initial time steps. (Time steps in model are changed according to stability requirements, where for larger fluxes one needs to take smaller steps.) The bottom half of the figure shows $2D$ sections (taken parallel to z, the main flow direction) of the final flow fields, obtained in (a2) dissolving and (b2) depositing porous media. lighter (darker) shadings correspond to higher (lower) than average fluxes. (a2) shows formation of elongated flow structures parallel to flow direction. (b2) shows more diffuse flow structures, although isotropy exists because of the driving pressure gradient along the z direction.

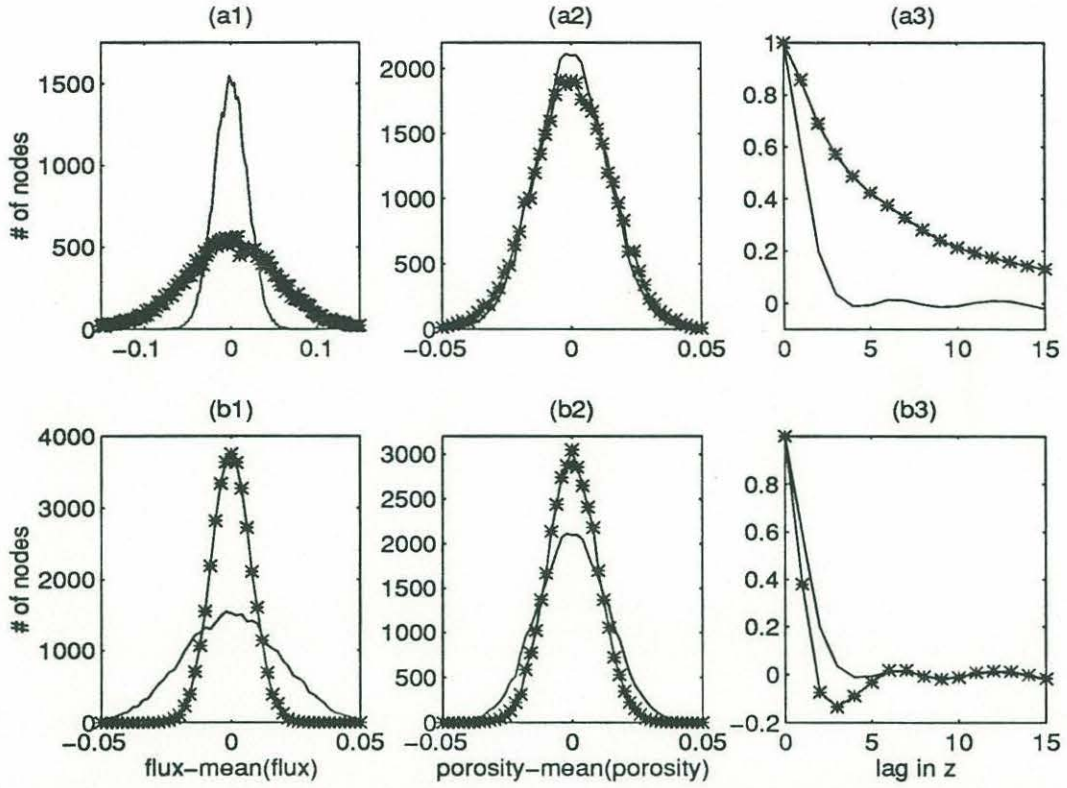

Figure 4-4: Histograms of flux and porosity, and correlation functions of porosity in a dissolving and "clogging" porous media. For the histograms the mean value of the variables was subtracted to enable comparison. Bin size is constant. The correlation functions of porosity shown are of lags along the z direction. Experiments performed on a 33^3 node box with $Da = 20, Pe = 10^3$ and $v_0 = 0.5$. Initial configuration in solid line. Final configuration in stars. a. Dissolving porous media: (a1) The variability in flux after 700 time steps is wide compared to the initial variability, as is expected for formation of focused, non-uniform flow with regions of fast and slow fluid velocity. (a2) The change in porosity variability between $t = 700$ and $t = 0$ is nearly unnoticeble. This is expected when permeability is changed due to organization of the porous medium and formation of long-range correlations, and not due to changes in porosity variability. (a3) Porosity correlation function in the direction parallel to flow is considerably enhanced, consistent with (a1) and (a2). b. Deposition in porous media: (b1) The variability of the flux after 600 time steps is much smaller than in the initial configuration, which means that the flow becomes more uniform with time. (b2) The decrease in porosity variability is less prominent, as expected when permeability is changed due to rearrangement of the porous media to form anti-correlations (i.e. preferential clogging in regions close to high permeability regions). (b3) Deposition results in reduced correlations in porosity which act to diffuse and homogenize the flow.

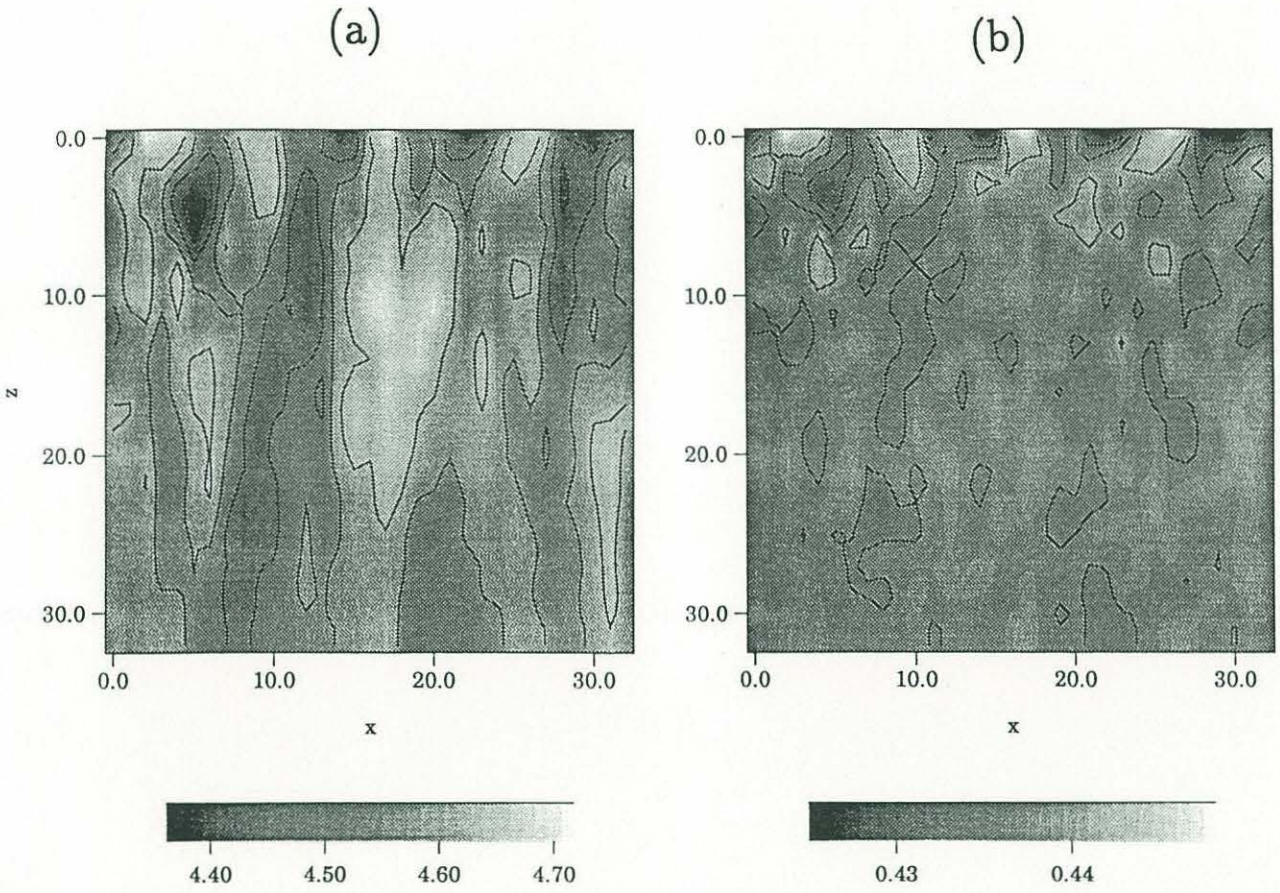

Figure 4-5: Vertical slices of the $3D$ flux field in a reacting porous medium with a gradient in solubility. Box is of 33^3 grid points. Parameters used: $Da = 20, Pe = 10^3, v_0 = 0.5$. (a) Dissolving porous medium with solubility increasing with z so that fluid is slightly undersaturated everywhere. Initial porosity distribution is random. The slice presented is taken after 700 time steps. Elongated channels are formed, with a large variation in flow velocities. (b) Using the configuration obtained by dissolution as the initial condition, the slice presented is taken from a porous media after 800 time steps of deposition. Flux channels have been obliterated. Flow is uniform with a small variability around the mean. (Some trace of channels can be observed at $z = 0$ where there is no reaction).

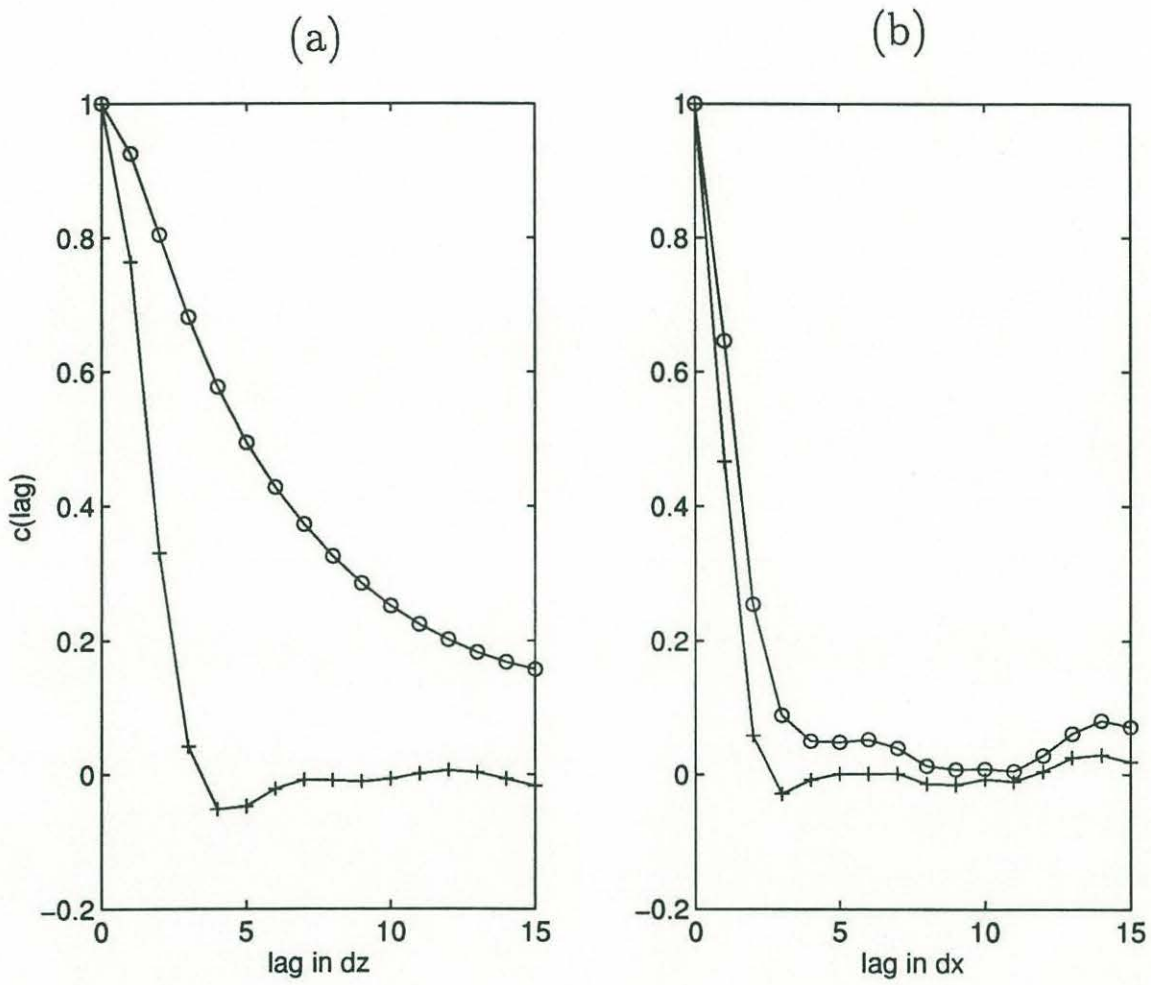

Figure 4-6: Correlation function of the flux field in a reacting porous medium with a gradient in solubility. Box is of 33^3 grid points. Parameters used: $Da = 20, Pe = 10^3, v_0 = 0.5$. The initial condition for dissolution is a random porous medium. The initial condition for deposition is the channelized porous media from the dissolution experiment. (a) Correlation functions parallel to flow direction (lag in z): Flux is highly correlated in the dissolved matrix, represented by circles, while it is completely uncorrelated in the deposited porous media (in plusses), i.e. the channels caused by dissolution have been preferentially clogged. (b) Correlation functions perpendicular to flow direction (lag in x): In a dissolved porous media (in circles) flow is somewhat correlated in the direction perpendicular to the forcing, i.e. pipes have a width larger than the grid spacing. These correlations are seen to be reduced by deposition (in plusses).

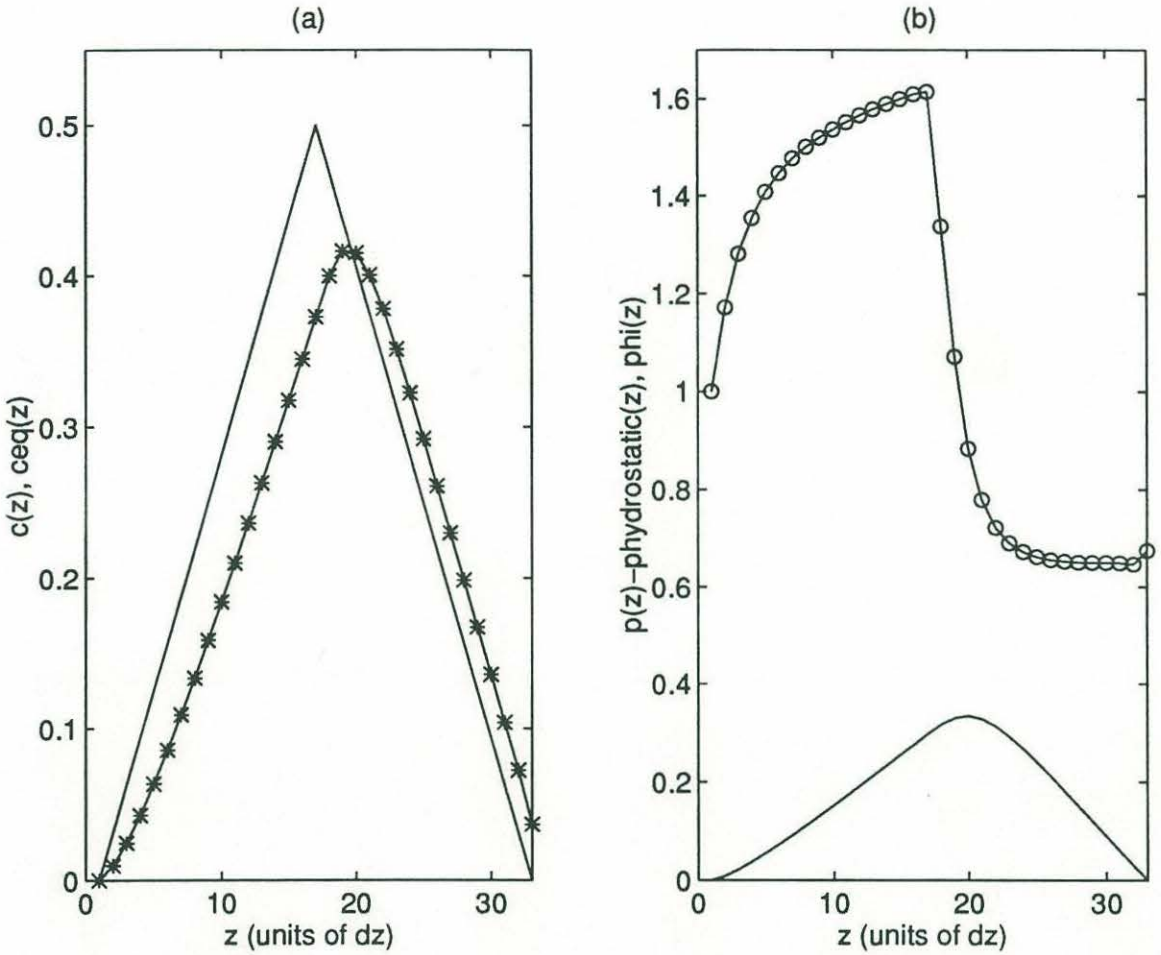

Figure 4-7: Results from simulations of the transition from dissolution to deposition, after 400 time steps. Porosity was initially homogeneous and random with average value of 1. Parameters are as in Figure 4-6. Plotted are various z profiles obtained by averaging over x and y. (a) Equilibrium concentration as a function of z, in solid line, and resulting concentration in stars. the fluid is increasingly undersaturated until a certain point, after which it is slightly supersaturated. The vertical distance between the maximas in concentration and in equilibrium concentration is determined by the Da number. (b) The porosity profile, in circles, has evolved to form a highly permeable region below a low porosity cap. Deviation of resulting pressure from hydrostatic pressure is plotted in solid line. While porosity attains a maximum at the same point as the equilibrium concentration, the overpressure attains a maximum at the transition between dissolution (undersaturation) and deposition (supersaturation). The deviation between these points is thus also dependent on Da.

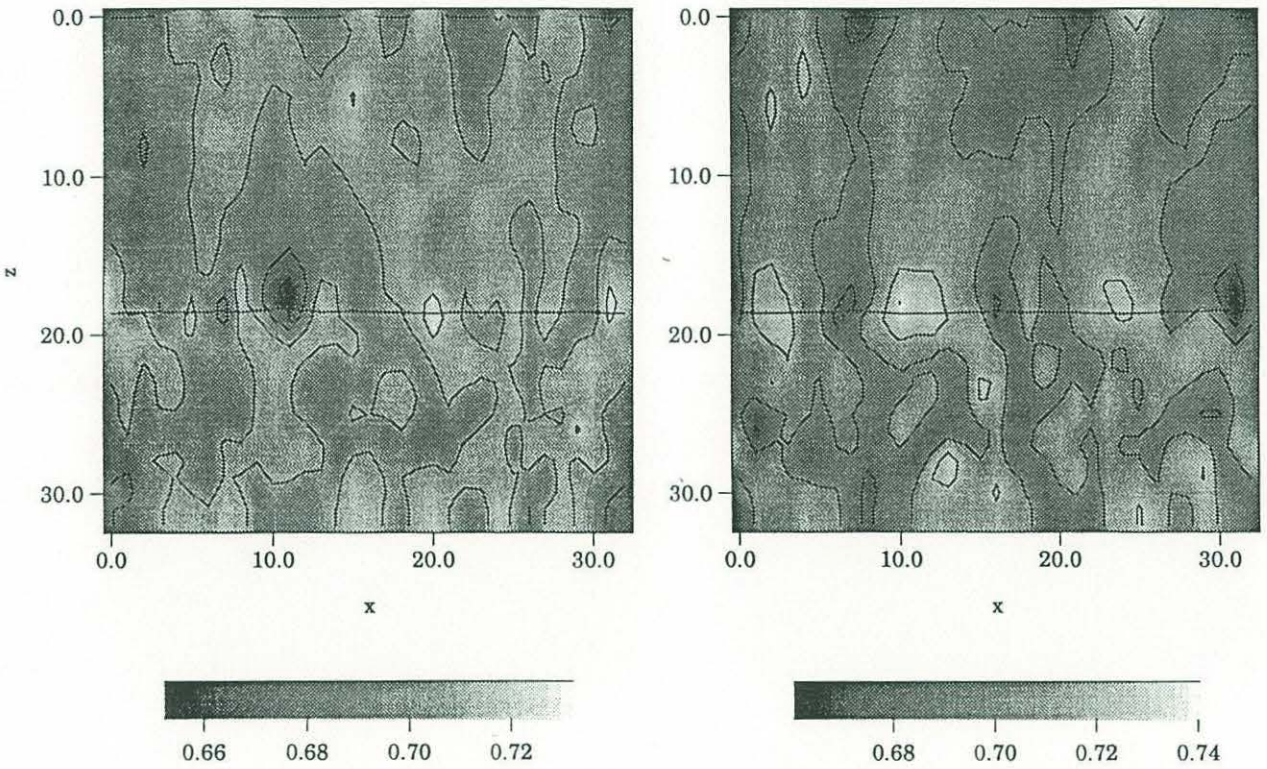

Figure 4-8: Two different vertical sections of a $3D$ flux field in a transition simulation. Flux channels span the dissolution region and may affect the crystallizing region as well. The $\phi = 1$ contour, which represents the transition point, is drawn as a horizontal solid line.

Chapter 5

Conclusions

Motivated by various observations in sedimentary and igneous rocks, this thesis presents a study of changes that occur in a porous medium subjected to flow and chemical reaction. Coupled flow and reaction operate during sedimentary rock formation, during upwelling of melt in the mantle, at the core-mantle boundary, and in various other technological and geological settings.

The coupled physical process influences the geometry of a porous matrix at both the microscopic and the macroscopic levels. At the smallest scale flow may have a role of keeping the system out of equilibrium so as to allow for growth and existence of non-equilibrium features. At larger scales flow may act as a "long-range messenger", causing large-scale organization during cementation or dissolution.

This thesis reaches two levels of conclusions: The first level is that generic aspects of flow and reaction change the statistical characteristics of a porous medium, with dissolution and deposition having qualitatively opposite effects (Chapter IV). It may be possible in the future to use the statistics to obtain quantitative constraints on the processes that different porous media have undergone. It is also clear that flow and reaction effect permeability, in a way which needs to be further studied. Future studies require deeper understanding and quantification of the interaction between the scales.

On the second level this thesis suggests that coupled flow and reaction are significant forces in geology: This generic physical process may be responsible for the

observed fractal structures on the pore scale of sedimentary rocks (Chapter II, also in [1]), for formation of channels in the mantle (Chapter III, also in [3], and [36, 32]), and for controlling modes of melt extraction (Chapter IV and [36]). The coupled process may influence rates of lava flow and sea floor accretion as well as volcanic eruptions. Future extension of these studies to more realistic conditions, both via experiments and through theory, is necessary before these new results can be used in a quantitative fashion.

Appendix A

Theoretical prediction of the roughness amplitude (Chapter II)

In this appendix we calculate a theoretical value for $A(D)$, the prefactor in equation 2.17, for interfaces formed by Model I. Our calculations will use the characteristics of the 'single-step' model and the fact that power spectra of self-affine interfaces follow a power-law [87].

In the calculation of $A(D)$ the first step is to define a two-dimensional discrete Fourier transform $H(p,q)$ of the height $h(m,n)$, where m and n are the discrete x and y positions respectively:

$$H(p,q) = \frac{1}{L^2} \sum_{m=1}^{L} \sum_{n=1}^{L} h(m,n) e^{-i2\pi(pm+qn)/L}. \tag{A.1}$$

The inverse transform is

$$h(m,n) = \sum_{p=1}^{L} \sum_{q=1}^{L} H(p,q) e^{i2\pi(pm+qn)/L}. \tag{A.2}$$

Since in Model I the height difference between adjacent sites is always constrained to be of amplitude one, the sum of the squares of the slopes in the x direction is

$$\sum_{m=1}^{L} \sum_{n=1}^{L} |h(m,n) - h(m-1,n)|^2 = L^2. \tag{A.3}$$

By substituting the inverse Fourier transform for h in the above 'sum-rule' one obtains

$$2 \sum_{p=1}^{L} \sum_{q=1}^{L} |H(p,q)|^2 (1 - \cos(2\pi p/L)) = 1 \tag{A.4}$$

The same calculation in the y direction gives

$$2\sum_{p=1}^{L}\sum_{q=1}^{L}|H(p,q)|^2(1-\cos(2\pi q/L))=1, \tag{A.5}$$

and by adding A.4 and A.5, we obtain

$$\sum_{p=1}^{L}\sum_{q=1}^{L}|H(p,q)|^2(2-\cos(2\pi q/L)-\cos(2\pi p/L))=1. \tag{A.6}$$

On the other hand, the width, as defined by equation 2.4, is also related to the power spectrum by the Parseval-Rayleigh relation:

$$W^2=\frac{1}{L^2}\sum_{m=1}^{L}\sum_{n=1}^{L}|h(m,n)-\bar{h}|^2=\sum_{p=1}^{L-1}\sum_{q=1}^{L-1}|H(p,q)|^2 \tag{A.7}$$

Thus $A(D)$ can be extracted from equations A.7 and 2.17:

$$A^2(D)=L^{2(D-3)}\sum_{p=1}^{L-1}\sum_{q=1}^{L-1}|H(p,q)|^2. \tag{A.8}$$

For self-affine interfaces the power spectrum scales like a power-law,

$$|H(p,q)|^2=A'(D)\left(\left(\frac{2\pi q}{L}\right)^2+\left(\frac{2\pi p}{L}\right)^2\right)^{D-4}, \tag{A.9}$$

where $A'(D)$ is the amplitude of the power spectrum [87].

Equation A.8 can be rewritten using $|H(p,q)|^2$ from equation A.9:

$$A(D)^2=A'(D)L^{2(D-3)}\sum_{p=1}^{L-1}\sum_{q=1}^{L-1}\left(\left(\frac{2\pi q}{L}\right)^2+\left(\frac{2\pi p}{L}\right)^2\right)^{D-4}. \tag{A.10}$$

$A'(D)$ can be derived by substituting the power spectrum given in A.9 in A.6 to give a final form for the square of the roughness amplitude

$$A^2(D)=L^{2(D-3)}\frac{\sum_{p=1}^{L-1}\sum_{q=1}^{L-1}(q^2+p^2)^{D-4}}{\sum_{p=1}^{L}\sum_{q=1}^{L}(2-\cos(2\pi q/L)-\cos(2\pi p/L))(q^2+p^2)^{D-4}}. \tag{A.11}$$

The sum can be evaluated numerically, to yield a theoretical value of $A(D)$, which is shown in Figure 2-15. Our calculations of A have not fully converged and show a very weak dependence on L, with L values taken up to 10^4. The integral approximation of the sum in equation A.11 shows however no dependence on L, and therefore full convergence is expected as $L\to\infty$.

Appendix B

Discussion of Parameter Values for the Mantle (Chapter III)

Table 3.1 illustrates the derivation of a range of Damköhler numbers which may be applicable to porous flow of melt in the mantle. The results are tabulated in two ways, in terms of an "equilibration length," and in terms of Damköhler number for a fixed system length scale of 100 m. In our study, the equilibration length, $L_{\rm eq} = \phi\rho_f w_0/R_{\rm eff}$, is the length over which fluid will advect before equilibrating with its surroundings.

Critical input parameters in determining equilibration lengths for the mantle are the crystal dissolution rate and the melt flow velocity. We present a broad range of possible values, because the estimation of effective dissolution rates, porosity and fluid velocity are so uncertain. Several studies have measured dissolution of mantle minerals in basaltic melts at upper mantle pressures and temperatures [41, 12, 96]. All of these indicate that measured dissolution rates are diffusion controlled, and thus depend on the diffusivity of the dissolving species and the width of a chemical boundary layer around the dissolving crystal. The first two studies emphasized results for relatively "well-stirred" melts, with narrow chemical boundary layers, while [96] attempted to minimize convection and mixing in liquids surrounding dissolving crystals, maximizing the width of the chemical boundary layer. It is difficult to know which of these apply to the microscopic geometry of melt flow in the mantle, below

the continuum or Darcy scale, in which some intergranular pores could be effectively stagnant, while others may carry rapidly moving liquids. For this reason, we use linear dissolution rates derived from these studies ranging from 10^{-8} to 10^{-12} m/s. We convert volume to weight units using an approximate density of 3000 kg m^{-3} to obtain the reaction rate constant, R.

To obtain effective dissolution rates (kg s^{-1} m^{-3}), we calculated effective surface areas over which dissolution could occur in mantle peridotites, per unit volume. This calculation requires estimation of the grain size, grain shape, proportion of solid/liquid surface area to total surface area, and proportion of soluble phases in the peridotite. Pyroxene is much more soluble than olivine in ascending liquids (e.g.,[33, 36]), so for the purposes of this calculation we assumed that the proportion of soluble phases was the proportion of pyroxene in mantle peridotite. We have used the work of [90] to estimate solid-liquid surface areas for basalt-mantle systems as a function of porosity. In calculating the solid surface area per unit volume, we have assumed cube-shaped grains with linear dimensions from 0.01 to 0.5 cm.

[36] calculated peridotite solubilities in typical melts along likely adiabatic P-T gradients beneath mido-ocean ridges, using a thermodynamic model for partially molten silicate systems. Thus this calculation incorporates the effect of the heat of fusion in limiting solid solubility. Results of these calculations were used to estimate an approximate value for the solubility gradient, given in Table 3.1. This calculation did not include the possible effects of advective heat transport by rising melt in high permeability channels. Potentially, if melt flux becomes large enough, this could result in local heating of channels to temperatures higher than the adiabat for partially melting mantle peridotite. If this occurred, it would increase the local solubility of solid phases to values higher than those in Table 3.1, and act to further enhance growth of channels.

Steady state melt flow velocities were calculated using the reasoning of [78], in which the Darcy flux, $\phi w_0 = FV_0$ (where F is integrated mass fraction of melting and V_0 is solid upwelling rate) for ascending mantle beneath a spreading ridge. Another simplification can be made if ϕ is constant (e.g.,[27, 75]). In this formulation, if ϕ is

much smaller than F, flow velocities are much greater than if the porosity is of the same order as the melt fraction. A range of values is used in Table 3.1 to investigate the maximum and minimum equilibration lengths likely in the mantle. Equilibration lengths calculated in this way range from Angstroms to meters.

The attempt to quantify effective reactive surface area brings about an interesting hypothesis about the finite size behavior of these channels: When high porosity channels form, the solid-liquid surface area per unit volume is reduced and the characteristic equilibration length of the system will increase. Hence the horizontal wavelength of the channels will grow (from equation 3.55). Increasing melt velocity with height results in an additional increase in L_{eq}. A tentative sketch of finite size behavior is given in Figure 3-9.

Bibliography

[1] E. Aharonov and D. H. Rothman. Growth of correlated pore-scale structures in sedimentary rocks: a dynamical model. *J. Geophy. Res.*, in press, 1995.

[2] E. Aharonov, A. Thompson, and D. H. Rothman. Roughness in rocks. *submitted to Science*, 1995.

[3] E. Aharonov, J. Whitehead, P. B. Kelemen, and M. Spiegelman. Channeling instability of upwelling melt in the mantle. *J. Geophy. Res.*, 100:20,433–20,450, 1995.

[4] J. G. Amar and F. Family. Phase transition in a restricted solid-on-solid surface-growth model in 2+1 dimensions. *Phys. Rev. Lett.*, 64:543–547, 1990.

[5] D. Avnir, D. Farin, and P. Pfeifer. Molecular fractal surfaces. *Nature*, 308:261–263, 1984.

[6] A. L. Barabasi and H. E. Stanley. *Fractal Concepts in Surface Growth.* Cambridge Univ. Press, New York, 1995.

[7] V. Barcilon and F. Richter. Nonlinear waves in compacting media. *J. Fluid Mech.*, 164:429–448, 1986.

[8] J. Bear. *Dynamics of Fluids in Porous Media.* Dover Publications, New York, 1972.

[9] S. Bekri, F. Thovert, and P. Adler. Dissolution in porous media. *Chem. Eng. Sci.*, 49:1–27, 1995.

[10] F. Boudier and A. Nicolas. Structural controls on partial melting in the Lanzo peridotites. In H. B. Dick, editor, *Magma Genesis*, pages 63–78, Portland, 1977. Oreg. Dep. of Geol. and Miner. Ind.

[11] R. Bracewell. *The Fourier transform and its applications.* McGraw-Hill, New York, 1978.

[12] M. Brearley, C.M. Scarfe, and H. Brenner. Dissolution rates of upper mantle minerals in an alkali basalt melt at high presssure: An experimental study and implications for ultramafic xenolith survival. *J. Petrol.*, 27:1157–1182, 1986.

[13] G. F. Carrier and C. E. Pearson. *Partial Differential Equations: Theory and Technique.* Academic, San Diego, Calif., 1988.

[14] J. Chadam, D. Hoff, E. Merino, P. Ortoleva, and A. Sen. Reactive infiltration instability. *IMA J. Appl. Math.*, 36:207–221, 1986.

[15] M. Cohen and M. Anderson. Geometry and topology of porous materials. In M. Tomkiewicz and P. Sen, editors, *The Chemistry and Physics of Porous Media*, pages 1–3. Electrochem. Soc., Pennigton, New Jersey, 1985.

[16] G. Daccord. Dissolutions, evaporations, etchings. In D. Avnir, editor, *The fractal approach to heterogeneous chemistry*, pages 183–197. Wiley and Sons, 1989.

[17] G. Daccord and R. Lenormand. Fractal pattrens from chemical dissolution. *Nature*, 325:431–432, 1987.

[18] P.G. de Gennes. *Physics of Disordered Materials.* Plenum, New York, 1985.

[19] H. Dick. Evidence of partial melting in the Josephine peridotite. In H. B. Dick, editor, *Magma Genesis*, pages 63–78, Portland, 1977. Oreg. Dep. of Geol. and Miner. Ind.

[20] S. Edwards and D. Wilkinson. The surface statistics of a granular aggregate. *Proc. R. Soc. London A*, 381:17–31, 1982.

[21] J. Hansen and A. Skjeltorp. Fractal pore space and rock permeability implications. *Phys. Rev. B*, 38:2635–2638, 1988.

[22] S. R. Hart. Equilibration during mantle melting: A fractal tree model. *Proc. Natl. Acad. Sci. U.S.A.*, 90:11,914–11,918, 1993.

[23] G. Hinch and B. S. Bhatt. Stability of an acid front moving through porous rock. *J. Fluid Mech.*, 212:279–288, 1990.

[24] M. Hoefner and H. Fogler. Pore evolution and channel formation during flow and reaction in porous media. *AIChE J.*, 34:45–54, 1988.

[25] A. W. Hofmann. Diffusion in natural silicate melt: A critical review. In R. B. Hargraves, editor, *Physics of melt migration*, pages 385–417. Princton Univ. Press, Princton, N.J., 1980.

[26] H. Iwamori. A model for disequilibrium mantle melting incorporating melt transport by porous and channel flows. *Nature*, 366:734–737, 1993.

[27] K.T.M. Johnson and H.J.B. Dick. Open system melting and the temporal and spatial variation of peridotite and basalt compositions at the Atlantis II fracture zone. *J. Geophys. Res.*, 97:9219–9241, 1992.

[28] K.T.M. Johnson, H.J.B. Dick, and N. Shimizu. Melting in the oceanic upper mantle: An ion microprobe study. *J. Geophys. Res.*, 95:2661–2678, 1990.

[29] M. Kardar, G. Parisi, and Y. Zhang. Dynamic scaling of growing interfaces. *Phys. Rev. Lett.*, 56:889–893, 1986.

[30] A.J. Katz and A.H. Thompson. Fractal sandstone pores: Implications for conductivity and pore formation. *Phys. Rev. Lett.*, 54:1325, 1985.

[31] P. Kelemen, N. Shimizu, and V. Salters. Focused flow of melt in the upper mantle: Extraction of MORB beneath oceanic spreading ridges. *Mineral Mag.*, 58A:466–467, 1994.

[32] P. B. Kelemen, N. Shimizu, and V. J. Salters. Extraction of MORB from the upwelling mantle by focused flow of melt in dunite channels. *Nature*, 375:747–753, 1995.

[33] P.B. Kelemen. Reaction between ultramafic wall rock and fractionating basaltic magma. *J. Petrol.*, 31:51–98, 1990.

[34] P.B. Kelemen, H. Dick, and J. Quick. Production of harzburgite by pervasive melt rock-reaction in the upper mantle. *Nature*, 358:635–641, 1992.

[35] P.B. Kelemen and H.J.B. Dick. Focused melt flow and localized deformation in the upper mantle: Juxtaposition of replacive dunite and ductile shear zones in the Josephine peridotite, SW Oregon. *J. Geophys. Res.*, 100:423–438, 1995.

[36] P.B. Kelemen, J. Whitehead, E. Aharonov, and K. Jordahl. Experiments on flow focusing in soluble porous media with applications to melt extraction from the mantle. *J. Geophys. Res.*, 100:475–496, 1995.

[37] E. M. Klein and C. H. Langmuir. Global correlations of oceanic ridge basalt chemistry with axial depth and crustal thickness. *J. Geophys. Res.*, 92:8089–8115, 1987.

[38] C.E. Krohn. Fractal measurments of sandstones, shales and carbonates. *J. Geophys. Res.*, 93:3297–3305, 1988.

[39] C.E. Krohn. Sandstone fractals and euclidean pore volume distributions. *J. Geophys. Res.*, 93:3286–3296, 1988.

[40] J. Krug and H. Spohn. Kinetic roughening of growing interfaces. In C. Godreche, editor, *Solids Far from Equilibrium*, pages 479–582. Cambridge Univ. Press, New York, 1991.

[41] L. C. Kuo and R. J. Kirkpatrick. Kinetics of crystal dissolution in the system diopside-forsterite-silica. *Am. J. Sci.*, 285:51–90, 1985.

[42] J. S. Langer. Instabilities and pattern formation in crystal growth. *Rev. Mod. Phys.*, 52:1–28, 1980.

[43] A. Lasaga and R. Kirkpatrik, editors. *Kinetics of Geochemical processes.* Reviews in Minerology, Washington, D.C., 1981.

[44] D. McKenzie. The generation and compaction of partially molten rock. *J. Petrol.*, 25:713–765, 1984.

[45] P. Meakin. The growth of rough surfaces and interfaces. *Phys. Rep.*, 235:189–289, 1993.

[46] P. Meakin and R. Jullien. Spatially correlated ballistic deposition. *Europhys. Lett.*, 9:71–76, 1989.

[47] P. Meakin and R. Jullien. Spatially correlated ballistic deposition on one and two dimensional surfaces. *Phys. Rev. A*, 41:983–993, 1990.

[48] P. Meakin, P. Ramanlan, L. Sander, and R. Ball. Ballistic depostion on surfaces. *Phys. Rev. A*, 34:152, 1986.

[49] E. Medina, T. Hwa, M. Kardar, and Y. C. Zhang. Burgers equation with correlated noise: renormalization-group analysis and applications to directed polymers and interface growth. *Phys. Rev. A*, 39:3053–3075, 1989.

[50] M. M. Morel and J. Hering. *Principles and applications of aquatic chemistry.* Wiley and sons, New York, 1993.

[51] J. Morse. The kinetics of calcium carbonate dissolution and precipitation. In R. Reeder, editor, *Carbonates: minerology and chemistry.* Mineralogical Sociaty of America, Washington, D.C., 1983.

[52] J. Morse and F. Mackenzie. *Geochemistry of sedimentary carbonates.* Elsevier, New York, 1990.

[53] K. L. Nagy and A. C. Lasaga. Dissolution and precipitatiion kinetics of Gibbsite at 80c and pH3. *Geochim. Cosmochim. Acta*, 56:3093, 1991.

[54] K. L. Nagy and A. C. Lasaga. Simultanieous precipitation kinetics of Keolonite and Gibbsite. *Geochim. Cosmochim. Acta*, 57:4329, 1993.

[55] A. Nicolas. *Structures of Ophiolites and Dynamics of Oceanic Lithosphere.* Kluwer Academic, Norwell, Mass., 1989.

[56] A. Nicolas. Melt extraction from mantle peridotites: Hydrofracturing and porous flow, with consequences for oceanic ridge activity. In M.P. Ryan, editor, *Magma Transport and Storage*, pages 159–174. John Wiley, New York, 1990.

[57] P. Ortoleva, J. Chadam, E. Merino, and A. Sen. Geochemical self-orgeganization ii: the reactive-infiltration instability. *Amer. J. of Sci.*, 287:1008–1040, 1987.

[58] P. Ortoleva, E. Merino, C. Moore, and J. Chadam. Geochemical self-organization, I, reaction-transport feedbacks. *Am. J. Sci.*, 287:979–1007, 1987.

[59] Y. Pellegrini and R. Jullien. Roughening transition and percolation in random ballistic deposition. *Phys. Rev. Lett.*, 64:1745, 1990.

[60] M Plischke, Z. Racz, and D. Liu. Time-reversal invariance and universality of two-dimensional growth models. *Phys. Rev. B.*, 35:3485–3495, 1987.

[61] W. Press, S. Teukolsky, W. Vetterling, and B. Flannery. *Numerical recipes in FORTRAN, 2nd edition.* Cambridge Univ. Press, 1993.

[62] J. Quick. The origin and significance of large, tabular dunite bodies in the Trinity peridotite, northern California. *Contrib. Mineral. Petrol.*, 78:413–422, 1981.

[63] S. Richardson and H. McSween. *Geochemistry, pathways and processes.* Prantice-Hall, New Jersey, 1989.

[64] G.N. Riley and D.L. Kohlstedt. Kinetics of melt migration in upper mantle tupe rocks. *Earth Planet. Sci. Lett.*, 105:500–521, 1991.

[65] J. D. Rimstidt and H. L. Barnes. The kinetics of silica-water reactions. *Geochim. Cosmochim. Acta*, 44:1683–1699, 1980.

[66] D. H. Rothman. Cellular-automaton fluids: A model for flow in porous media. *Geophysics*, 53:509–518, 1988.

[67] J. Salles, J. Thovert, and P. Adler. Deposition in porous media and clogging. *Chem Eng. Sci.*, 48:2839–2858, 1993.

[68] V. J. M. Salters and S. Hart. The Hf-paradox and the role of garnet in the MORB source. *Nature*, 342:420–422, 1989.

[69] C. H. Scholz, A. Leger, and S. L. Karner. Experimental diagenesis: exploratory results. *Geophys. Res. Lett.*, 22:719–722, 1995.

[70] D. Scott. The competition between percolation and circulation in a deformable porous medium. *J. Geophys. Res.*, 93:6451–6462, 1988.

[71] D. Scott and D. Stevenson. Magma ascent by porous flow. *J. Geophys. Res.*, 91:9283–9293, 1986.

[72] N.H. Sleep. Formation of oceanic crust: Some thermal constraints. *J. Geophys. Res.*, 80:4037–4042, 1975.

[73] N.H. Sleep. Tapping of melt by veins and dykes. *J. Geophys. Res.*, 93:10255–10272, 1988.

[74] P. Smolarkiewicz. A simple positive definite advection scheme with small implicit diffusion. *Monthly Weather Rev.*, 111:479–486, 1983.

[75] A. V. Sobolev and N. Shimizu. Ultra-depleted primary melt included in an olivine from the Mid-Atlantic Ridge. *Nature*, 363:151–154, 1993.

[76] M. Spiegelman. Flow in deformable porous media, 1, Simple analysis. *J. Fluid Mech.*, 247:39–63, 1993.

[77] M. Spiegelman. Flow in deformable porous media, 2, Numerical analysis — the relationship between shock waves and solitary waves. *J. Fluid Mech.*, 247:17–38, 1993.

[78] M. Spiegelman. Physics of melt extraction: Theory, implications and applications. *Philos. Trans. R. Soc. London A*, 342:23–41, 1993.

[79] M. Spiegelman and P. Kenyon. The requirements for chemical disequilibrium during magma migration. *Earth. Planet. Sci. Lett.*, 109:611–620, 1992.

[80] C. Steefel and A. Lasaga. Evolution of dissolution patterns. In D.C. Melchior and R.L. Bassett, editors, *Chemical Modeling in Aqueous Systems II*, pages 212–225. Am. Chem. Soc., Washington, D.C., 1990.

[81] D. Stevenson. Spontaneous small-scale melt segregation in partial melts undergoing deformation. *Geophys. Res. Lett.*, 9:1076–1070, 1989.

[82] S. Tait, K. Jahrling, and C. Jaupart. The planform of compositional convection and chimney formation in a mushy layer. *Nature*, 359:406–408, 1992.

[83] A.H. Thompson. Fractals in rock physics. *Annu. Rev. Earth Planet. Sci.*, 19:237, 1991.

[84] A.H. Thompson, A. Katz, and C. Krohn. the microgeometry and transport properties of sedimentary rocks. *Advan. in Phys.*, 36:625–694, 1987.

[85] A.H. Thompson, J. B. Knight, and R. A. Raschke. Trends in fractal rock pores: Implications for universal pore formation processes. *submitted to J. Geophy. Res.*, 1995.

[86] D. Turcotte. Physics of magma segregation. In B. O. Mysen, editor, *Magmatic processes: Physiochemical principles*, page 69. Geochemical Society, 1987.

[87] D. Turcotte. *Fractals and chaos in geology and geophysics.* Cambridge university press, Cambridge, 1992.

[88] D. Turcotte and G. Schubert. *Geodynamics, Application of Continuum Physics to Geological Problems.* John Wiley, New York, 1982.

[89] T. Vicsek. *Fractal growth phenomena.* World Scientific, Singapore, 1992.

[90] N. VonBargen and H. Waff. Permeabilities, interfacial areas and curvatures of partially molten systems: Results of numerical computations of equilibrium microstructures. *J. Geophys. Res.*, 91:9261–9276, 1986.

[91] R. F. Voss. Random fractals. In R. Pynn and A. Skjeltrop, editors, *Scaling phenomena in disordered systems*, pages 1–11. Plenum, London, 1985.

[92] J. Walls, D. Janecky, and B. Travis. A lattice gas automata model for hetrogeneous chemical reactions at mineral surfaces and in pore networks. *Phys. D*, 47:115–123, 1991.

[93] J. D. Weeks. The roughening transition. In T. Riste, editor, *Ordering in strongly fluctuating condensed matter systems*, pages 293–317. Plenum, 1980.

[94] P. Wong, J. Howard, and J. Lin. Surface roughening and the fractal nature of rocks. *Phys. Rev. Lett.*, 57:637–641, 1986.

[95] H. Yan, D. Kessler, and L.M. Sander. Roughening phase transition in surface growth. *Phys. Rev. Lett.*, 64:926, 1989.

[96] Y. Zhang, D. Walker, and C.E. Lesher. Diffusive crystal dissolution. *Contrib. Mineral. Petrol.*, 102:492–513, 1989.